

# **XAS investigation of catalytically relevant metal and metal oxides dispersed in inorganic matrices**

Von der Fakultät Chemie der Universität Stuttgart  
zur Erlangung der Würde eines Doktors der  
Naturwissenschaften (Dr. rer. nat.) genehmigte Abhandlung

Vorgelegt von  
**Sankaran Anantharaman**  
aus Tirunelveli, Indien

Hauptberichter: Prof. Dr. H. Bertagnolli  
Mitberichter: Prof. Dr. F. Gießelmann

Tag der mündlichen Prüfung: 28.07.2010

Institut für Physikalische Chemie der Universität Stuttgart  
2010

Eidesstattliche Erklärung Ich versichere, daß ich diese Dissertation selbstständig verfaßt und nur die angegebenen Quellen und Hilfsmittel verwendet habe.

Stuttgart, 28.07.2010

Sankaran Anantharaman

Prüfungsvorsitzender: Prof. Dr. T. Schleid  
Hauptberichter: Prof. Dr. H. Bertagnolli  
Mitberichter: Prof. Dr. F. Gießelmann

# Contents

<b>List of Figures</b>	<b>v</b>
<b>List of Tables</b>	<b>xi</b>
<b>1. Introduction</b>	<b>1</b>
<b>2. XAS investigation of platinum clusters in zeolite Y</b>	<b>3</b>
2.1. Introduction . . . . .	3
2.1.1. Supported metal catalysts . . . . .	3
2.1.2. Formation of metal clusters in zeolite cages by reduction of ion exchanged cations . . . . .	4
2.2. Experimental method . . . . .	5
2.2.1. Data evaluation . . . . .	6
2.3. Results and discussion . . . . .	7
2.3.1. XANES investigation . . . . .	7
2.3.2. EXAFS investigation . . . . .	11
<b>3. Parameterization of resonance absorption at the L edges of Pt</b>	<b>17</b>
3.1. Introduction . . . . .	17
3.1.1. White lines . . . . .	18
3.1.2. L <sub>2</sub> and L <sub>3</sub> edges in Pt . . . . .	20
3.1.3. Method used to extract d-band information . . . . .	22
3.1.4. Absorption contribution of the white line . . . . .	24
3.1.5. Deconvolution of XANES region . . . . .	27
3.2. Results and Discussion . . . . .	30
3.2.1. Quantitative determination of the number of d-electron states in Pt/NaY . . . . .	30

3.2.2. QXAS during CO interaction with 6 wt%Pt/NaY . . . . .	37
<b>4. Multi-resolution wavelet analysis of EXAFS spectra</b>	<b>45</b>
4.1. Introduction . . . . .	45
4.2. Formulation . . . . .	46
4.3. Results and discussion . . . . .	49
4.3.1. Wavelet analysis of model EXAFS spectra . . . . .	49
4.3.2. Limitations in resolution achievable using Morlet wavelets . . . . .	56
4.3.3. Effect of superposition of two constituent signals on the wavelet transform . . . . .	57
<b>5. Ruthenium based catalysts in zeolite</b>	<b>65</b>
5.1. Introduction . . . . .	65
5.1.1. Zeolites . . . . .	67
5.1.2. Local structure of ruthenium oxide and hydroxide . . . . .	69
5.1.3. In situ XAS set up . . . . .	72
5.2. Results and discussion . . . . .	78
5.2.1. XANES investigation . . . . .	78
5.2.2. EXAFS investigation . . . . .	84
5.2.3. Theoretical standards in EXAFS analysis . . . . .	84
<b>6. Summary</b>	<b>107</b>
<b>7. Zusammenfassung</b>	<b>113</b>
<b>A. Appendix</b>	<b>119</b>
A.1. XAS experiment . . . . .	119
A.1.1. Monochromator . . . . .	120
A.1.2. Ion chambers . . . . .	126
A.2. Analysis of XAS data . . . . .	126
A.2.1. EXAFS Fourier transform . . . . .	127
A.2.2. The isolation of $\chi(k)$ . . . . .	128
A.3. Curve fitting of QXAS during CO interaction with 6wt% Pt/NaY . . . . .	131
<b>References</b>	<b>139</b>

# List of Figures

2.1. XANES measured at the Pt L <sub>3</sub> edge (11564 eV) for the samples investigated	7
2.2. Q-XAS Pt L <sub>3</sub> edge (11564 eV) spectra collected during the temperature treatment under hydrogen gas flow of the as prepared (oxygen pre-calcined) sample . . . . .	8
2.3. Q-XAS Pt L <sub>3</sub> edge (11564 eV) spectra collected after reaching 475.35 K during the temperature treatment under hydrogen gas flow of the as prepared (oxygen pre-calcined) sample . . . . .	9
2.4. Q-XAS Pt L <sub>3</sub> edge (11564 eV) spectra during CO interaction with platinum cluster at room temperature . . . . .	10
2.5. Experimental EXAFS function (left), its Fourier transform (right) and fit to the experimental data of Pt <sub>13</sub> H <sub>m</sub> /NaY . . . . .	12
2.6. Experimental EXAFS function (left), its Fourier transform (right) and fit to the experimental data of Pt <sub>x</sub> (CO) <sub>m</sub> /NaY . . . . .	13
2.7. Experimental EXAFS function (left), its Fourier transform (right) of Pt <sub>13</sub> H <sub>m</sub> /NaY and Pt <sub>x</sub> (CO) <sub>m</sub> /NaY . . . . .	14
2.8. The schematic structure of Pt <sub>2</sub> (CO) <sub>m</sub> in NaY with possible CO bonding scenario . . . . .	14
3.1. Absorption edges of elements with the electronic shells . . . . .	18
3.2. Schematic diagram illustrating the photoabsorption process for noble metals and the resulting XANES spectrum. N(E) is the density of states which shows a characteristic narrow d-band and free-electron-like sp-band. White line feature in the XANES shown in the upper left hand side of the figure arise from dipole transitions from core levels to unoccupied states above the Fermi level . . . . .	19

3.3. A rough sketch of the density of states in platinum plotted versus energy for the L <sub>2</sub> edge, L <sub>3</sub> edge and conduction band including spin-orbit coupling. The shaded region indicate the unoccupied states above the Fermi level and the double feature in the d-band indicates splitting due to spin-orbit coupling (Reproduced from reference [1]) . . . . .	21
3.4. Normalized L <sub>3</sub> and L <sub>2</sub> edge XAS spectra of Pt metal foil . . . . .	23
3.5. Comparison of the L <sub>2</sub> , L <sub>3</sub> edges of Pt metal foil and 12 wt% Pt-H <sub>2</sub> /NaY at 473 K . . . . .	31
3.6. Comparison of the L <sub>2</sub> and L <sub>3</sub> edge spectra of Pt metal foil with 12 wt% Pt-H <sub>2</sub> /NaY at 473 K . . . . .	32
3.7. Comparison of the L <sub>2</sub> and L <sub>3</sub> edge spectra of Pt metal foil with 12 wt% Pt/-NaY at 473 K after purging with Ar gas flow . . . . .	33
3.8. Comparison of the L <sub>2</sub> and L <sub>3</sub> edge spectra of Pt metal foil with 12wt% Pt-H <sub>2</sub> /NaY at room temperature (rt) . . . . .	34
3.9. Comparison of the L <sub>2</sub> and L <sub>3</sub> edge spectra of Pt metal foil with 6wt% Pt/-NaY at (Bottom) rt after purging with Ar gas flow . . . . .	35
3.10. Comparison of the L <sub>2</sub> and L <sub>3</sub> edge spectra of Pt metal foil with 6wt% Pt-H <sub>2</sub> /NaY at 473 K . . . . .	36
3.11. Comparison of the L <sub>2</sub> and L <sub>3</sub> edge spectra of Pt metal foil with 6wt% Pt/-NaY at 473 K (Bottom) after purging with Ar gas flow . . . . .	37
3.12. Comparison of the L <sub>2</sub> and L <sub>3</sub> edge spectra of Pt metal foil with 6wt% Pt-CO/NaY at room temperature following reduction under hydrogen flow, argon flow to remove adsorbed hydrogen and subsequent CO flow . . . . .	38
3.13. Q-XAS Pt L <sub>3</sub> edge (11564 eV) spectra during CO interaction with platinum cluster at room temperature . . . . .	39
3.14. Area under the curve determined in the range [11568 to 11580 eV] . . . . .	41
3.15. Area under the curve determined in the range [11540 to 11580 eV] . . . . .	41
3.16. Area under the curve (pseudo-Voigt function) estimated in the range [11560 to 11580 eV] as a function of time and the linear fit to the data in two regions indicating the kinetic behavior . . . . .	43
4.1. Time-frequency boxes of two wavelets $\psi_{u,s}$ and $\psi_{u_0,s_0}$ . When the scale $s$ decreases, the time spread is reduced but the frequency spread increases and covers an interval that is shifted towards higher frequencies . . . . .	47

4.2. Morlet wavelet as a function of variable $t$ with $\kappa = 14$ ; $\sigma = 2$ (Left) and $\kappa = 2$ ; $\sigma = 1$ (Right) . . . . .	49
4.3. Magnitude of backscattering amplitude of Ag and Au with different $k$ weightings generated using EXCURV98 [2] package . . . . .	51
4.4. Fourier transform (Solid line) of model EXAFS signals 1 (left) and 2 (right) along with the sine transform (dashed line) with $k$ -weighting of 1, 2 and 3 (top–bottom) . . . . .	52
4.5. Contour plots of the overview wavelet transform of EXAFS signal 1 with $k$ -weighting of 0, 1, 2 and 3 . . . . .	53
4.6. Contour plots of the resolved wavelet transform of EXAFS signal 1 with $k$ -weighting of 0, 1, 2 and 3 . . . . .	54
4.7. Wavelet of type 2 as a function of variable $t$ with $\kappa = 2$ ; $\sigma = \{1, 0.8, 0.7, 0.6\}$ (top left–bottom right) . . . . .	56
4.8. Model input signals with different $\Delta C$ values (given on the figures in the right side) and their FT modulus . . . . .	58
4.9. Wavelet transform of the input signal with $\Delta C=1$ using different wavelet parameters given with each plot . . . . .	59
4.10. Wavelet transform of the input signal with $\Delta C=2$ using different wavelet parameters given with each plot . . . . .	60
4.11. Wavelet transform of the input signal with $\Delta C=3$ using different wavelet parameters given with each plot . . . . .	61
4.12. Wavelet transform of the input signal with $\Delta C=4$ using different wavelet parameters given with each plot . . . . .	62
4.13. Wavelet transform of the input signal with $\Delta C=5$ using different wavelet parameters given with each plot . . . . .	63
5.1. Idealized picture of channel system in silicate shown along with the dimensions of the channels . . . . .	67
5.2. Secondary building unit (bold) along with the chain-type building block	69
5.3. Skeletal diagram of ZSM-5 layer with the chains of figure 5.2 around the channel opening . . . . .	69
5.4. Depiction of sodalite cages connected to form Zeolite-A . . . . .	70

5.5. Structure models of RuO <sub>2</sub> ·0.29H <sub>2</sub> O featuring RuO <sub>6</sub> octahedral dimers (left) and RuO <sub>2</sub> ·2.32H <sub>2</sub> O (right) with disordered RuO <sub>6</sub> linked in twisted unconnected chains [79] . . . . .	71
5.6. Structure model of anhydrous RuO <sub>2</sub> featuring c-axis projection (left) and b-axis projection (right) [79] . . . . .	71
5.7. Schematic of the quartz catalytic reactor used as high-temperature flow reactor and simultaneously as a good x-ray transmission cell for XAS measurements along with the gas mixing and supply unit . . . . .	73
5.8. Picture of the quartz cell with an operating temperature range starting from RT to 623 K . . . . .	74
5.9. Technical drawing of the adjustable mounting platform of the inconel alloy heating block and the modified ultra-tight gas connectors used to connect the metal tubes to the quartz reactor (dimensions given in mm)	75
5.10. Technical drawing of the inconel alloy heating block of the quartz cell indicating the dimensions in mm . . . . .	76
5.11. Stainless steel cell with temperature range from RT to 553 K . . . . .	77
5.12. Ruthenium K edge XANES spectra of reference samples of Ru-metal, anhydrous RuO <sub>2</sub> , hydrous RuO <sub>2</sub> and ruthenium catalysts without the calcination step. For the notation see table 5.2 . . . . .	79
5.13. Ruthenium K edge XANES spectra of reference samples of Ru-metal, anhydrous RuO <sub>2</sub> , hydrous RuO <sub>2</sub> and ruthenium catalysts after calcination post-treatment. For the notation see table 5.2 . . . . .	80
5.14. XANES region of sample 7 at 393.15 K under hydrogen flow and minutes after reduction measured in situ under 25 ml min <sup>-1</sup> hydrogen gas flow. For comparison the XANES spectrum of the sample before reduction is also given . . . . .	81
5.15. XANES spectra of Ru/NaA2 at measurement conditions of a–d along with the fit obtained as a linear combination of XANES spectra of hydrous RuO <sub>2</sub> and Ru-metal . . . . .	82
5.16. Experimental Fourier transformed EXAFS spectrum RuO <sub>2</sub> along with the fit to the data obtained from FEFF simulation. The type of atoms in a particular coordination shell, the interatomic distances and average coordination numbers according to the crystallographic data are indicated	88



5.17. EXAFS model representing the single scattering paths originating from the central Ru atom of rutile type RuO <sub>2</sub> . . . . .	90
5.18. Experimental EXAFS data of anhydrous RuO <sub>2</sub> and the fitted EXAFS function using scenario 1 . . . . .	92
5.19. Experimental EXAFS data of Sample 3 and the fitted EXAFS function using scenario 1 . . . . .	94
5.20. Experimental EXAFS data of Sample 4 and the fitted EXAFS function using scenario 1 . . . . .	94
5.21. Experimental EXAFS data of Sample 3 and the fitted EXAFS function using scenario 2 . . . . .	95
5.22. Experimental EXAFS data of Sample 4 and the fitted EXAFS function using scenario 2 . . . . .	96
5.23. Experimental EXAFS data of Sample 3 and the fitted EXAFS function using scenario 3 . . . . .	97
5.24. Experimental EXAFS data of Sample 4 and the fitted EXAFS function using scenario 3 . . . . .	97
5.25. Experimental EXAFS data of Sample 9 and the fitted EXAFS function using a two shell model of crystalline RuO <sub>2</sub> . . . . .	100
5.26. Comparison of experimental EXAFS spectra of Ru/NaA1 and Ru/NaA2 (samples 6 and 7) along with hydrous RuO <sub>2</sub> reference . . . . .	101
5.27. Model of two-dimensional RuO <sub>2</sub> ·2.32H <sub>2</sub> O with disordered RuO <sub>6</sub> edge connected in twisted unconnected chains . . . . .	102
5.28. Experimental EXAFS data of Sample 6 and the fitted EXAFS function using a two-shell model of crystalline RuO <sub>2</sub> . . . . .	102
5.29. Experimental EXAFS data of Sample 7 and the fitted EXAFS function using a two-shell model of crystalline RuO <sub>2</sub> . . . . .	104
5.30. Experimental EXAFS data of reference 3, hydrous RuO <sub>2</sub> and the fitted EXAFS function using a two-shell model of RuO <sub>2</sub> . . . . .	104
A.1. Layout of a typical XAS beamline experiment in transmission mode . . .	119
A.2. Double crystal monochromator mounted on a goniometer. In addition, the second crystal can be rotated separately and used to detune the monochromator. . . . .	122

A.3. Variation of reflected intensity with various degrees of overlapping of the diffraction patterns of crystals 1 and 2 as the crystals are rocked through the parallel position. The values of the product integrals plotted as ordinates in the lower curve correspond to total superposed area available with different degrees of overlap . . . . .	123
A.4. X-rays from a white source are incident on two crystals aligned in the same orientation. The central ray (full line) will be Bragg reflected by both the crystals and will emerge parallel to the original ray. The angle of incidence this ray makes with the second crystal is the same as that it made with the first, and will be Bragg reflected. The DuMond diagram in the right shows that a scan of the second crystal has a width equal to the convolution of the Darwin widths of the two crystals . . . . .	124
A.5. The experimental Q-XAS spectra measured after a given time of CO interaction, fit to the experimental spectrum using an arctan function to the rising absorption edge and a pseudo-Voigt function to the white line and the residual from the fit to the experiment are given for spectra 1–4 . . .	133
A.6. The experimental Q-XAS spectra measured after a given time of CO interaction, fit to the experimental spectrum using an arctan function to the rising absorption edge and a pseudo-Voigt function to the white line and the residual from the fit to the experiment are given for spectra 5–8 . . .	134
A.7. The experimental Q-XAS spectra measured after a given time of CO interaction, fit to the experimental spectrum using an arctan function to the rising absorption edge and a pseudo-Voigt function to the white line and the residual from the fit to the experiment are given for spectra 9–12 . .	135
A.8. The experimental Q-XAS spectra measured after a given time of CO interaction, fit to the experimental spectrum using an arctan function to the rising absorption edge and a pseudo-Voigt function to the white line and the residual from the fit to the experiment are given for spectra 13–16 .	136
A.9. The experimental Q-XAS spectra measured after a given time of CO interaction, fit to the experimental spectrum using an arctan function to the rising absorption edge and a pseudo-Voigt function to the white line and the residual from the fit to the experiment are given for spectra 17–19 along with the fit to the XANES spectra of 6wt% Pt-CO/NaY (bottom right)	137

# List of Tables

2.1. List of all the platinum samples and the their treatment conditions before XAS measurements . . . . .	6
2.2. Fit results of the EXAFS data of samples Pt <sub>13</sub> -H <sub>m</sub> /NaY and Pt <sub>x</sub> (CO) <sub>m</sub> /NaY. <sup>a</sup> Absorber(Abs)-back scatterer(Bs). <sup>b</sup> Average coordination number(CN). <sup>c</sup> Inter atomic distance. <sup>d</sup> EXAFS Debye-Waller factor( $\sigma$ ) with its estimated deviation. <sup>e</sup> see text in section 2.2.1 . . . . .	15
3.1. List of platinum in zeolite samples subjected to quantitative determination of d-electron states. Pt L <sub>2</sub> and L <sub>3</sub> edge XAS spectra were measured after in situ treatment at the above mentioned measurement conditions .	31
3.2. Area under the curve determined using Simpson's rule. . . . .	35
3.3. Fractional change in d-band vacancies, $f_d$ and the total density of unoccupied states with d-character $\Delta h_{total}$ calculated for different samples. <sup>a</sup> -uncertainty of 5% reported by Sham, Naftel and Coulthard [3] . . . . .	36
3.4. The numerically integrated area under the curve during CO interaction measured in Q-XAS mode using two different integration (energy) ranges	40
3.5. The centers of the fitted arctan function and the area estimated by numerical integration under the fitted pseudo-Voigt function during CO interaction with Pt/NaY material. . . . .	42
4.1. Parameters used in the generation of the model EXAFS signal. <sup>a</sup> Absorber(Abs)-backscatterer(Bs). <sup>b</sup> Average coordination number(CN). <sup>c</sup> Interatomic distance. <sup>d</sup> EXAFS Debye-Waller factor( $\sigma$ ) . . . . .	50
4.2. Wavelet parameters used in the present study to vary the resolution of the wavelet transform . . . . .	53

4.3. The centers in the wavelet transformed EXAFS signal along the $k$ and $r$ coordinates corresponding to maximum magnitude of wavelet transformed signal . . . . .	55
5.1. Zeolites used in this study and their pore dimensions . . . . .	70
5.2. Ruthenium containing zeolite samples and the references used in the XAS investigation . . . . .	78
5.3. Weighting fraction of the reference spectra determined by LC-XANES fit for sample NaA2 measured under different conditions . . . . .	83
5.4. EXAFS fit results of anhydrous RuO <sub>2</sub> reference sample. <sup>a</sup> Path of absorber–backscatterer. <sup>b</sup> Path degeneracy or coordination number. <sup>c</sup> Distance between the absorber and the neighboring atom ( $R_i = R_{\text{eff}i} + \Delta R_i$ ). <sup>d</sup> Mean squared displacement of bond length. <sup>e</sup> Shift in energy scale reference .	90
5.5. EXAFS fit results of samples subjected to calcination post-treatment using the model of anhydrous RuO <sub>2</sub> . The parameters not iterated in course of the fit are given in bold and those parameters resulting from iteration are given in normal text. <sup>a</sup> Path of absorber–backscatterer. <sup>b</sup> Path degeneracy or coordination number. Value of ( $S_0^2$ ) was fixed at ( $S_0^2$ )=1. <sup>c</sup> Distance between the absorber and the neighboring atom ( $R_i = R_{\text{eff}i} + \Delta R_i$ ). <sup>d</sup> Mean squared displacement of bond length. <sup>e</sup> Shift in energy scale reference .	93
5.6. EXAFS fit results of samples subjected to calcination post-treatment using the model of rutile RuO <sub>2</sub> . <sup>a</sup> Path of absorber–backscatterer. <sup>b</sup> Path degeneracy or coordination number. Value of ( $S_0^2$ ) was fixed at ( $S_0^2$ )=1. <sup>c</sup> Distance between the absorber and the neighboring atom ( $R_i = R_{\text{eff}i} + \Delta R_i$ ). <sup>d</sup> Mean squared displacement of bond length. <sup>e</sup> Shift in energy scale reference. The parameters not iterated in course of the fit are given in bold and those parameters resulting from iteration are given in normal text .	95
5.7. EXAFS fit results of samples subjected to calcination post-treatment using the model of rutile RuO <sub>2</sub> . <sup>a</sup> Path of absorber–backscatterer. <sup>b</sup> Path degeneracy or coordination number. <sup>c</sup> Distance between the absorber and the neighboring atom ( $R_i = R_{\text{eff}i} + \Delta R_i$ ). <sup>d</sup> Mean squared displacement of bond length. <sup>e</sup> Shift in energy scale reference. The parameters not iterated in course of the fit are given in bold and those parameters resulting from iteration are given in normal text . . . . .	98

5.8. EXAFS fit results of sample 9 using the first Ru–O and Ru–Ru paths of rutile RuO <sub>2</sub> . <sup>a</sup> Path of absorber–backscatterer. <sup>b</sup> Path degeneracy or coordination number. <sup>c</sup> Distance between the absorber and the neighboring atom ( $R_i = R_{effi} + \Delta R_i$ ). <sup>d</sup> Mean squared displacement of bond length. <sup>e</sup> Shift in energy scale reference . . . . .	99
5.9. EXAFS fit results of samples without calcination post-treatment, using the two shell model of crystalline RuO <sub>2</sub> . <sup>a</sup> Path of absorber–backscatterer. <sup>b</sup> Path degeneracy or coordination number. <sup>c</sup> Distance between the absorber and the neighboring atom ( $R_i = R_{effi} + \Delta R_i$ ). <sup>d</sup> Mean squared displacement of bond length. <sup>e</sup> Shift in energy scale reference. The parameters not iterated in course of the fit are given in bold and those parameters resulting from iteration are given in normal text . . . . .	103
A.1. The double crystal monochromator chosen according to the edge energies of the elements studied and the beamlines where the XAS spectra were recorded [90] . . . . .	125



# 1. Introduction

Modern world depends on energy and this enormous demand for energy is in the present day satisfied by fossil fuels which power our transport systems, electricity grids, industry and agriculture. It is well known that this supply of fossil energy is limited. Further, continuously increasing carbon dioxide emissions causes concerns for the balance of the world climate. There is an immediate and enormous emphasis on the scientific community to develop alternative sources of energy and to ensure sustainable methods of energy usage, storage and delivery.

Materials research is at the heart of development for modern energy systems. Photo voltaic systems, fuel cells which could work on hydrogen, alcohols or hydrocarbons that are oxidized electrochemically to produce electricity, new materials for rechargeable batteries, especially those based on lithium, hydrogen storage materials, based on light elements that bind and release hydrogen under mild conditions are all actively sought. Similarly, materials that can adsorb carbon dioxide or other pollutants can be used to help clean up the products of combustion from a fossil-fuel power plant. Experiments to fully understand the structure and properties of materials for these varied applications and to develop low-cost materials with enhanced properties is the key to take these modern innovations to the common man.

Material research is substantially carried out in laboratories around the world however, synchrotron radiation based techniques play a very important and significant role in this area too. Certain materials could only be completely characterized using the powerful yet expensive synchrotron radiation techniques and XAS is one such technique which has been at the forefront of catalysis research to study catalysts under operating conditions. Bulk metals and metal oxides have been used extensively in catalysis and continue to find immense use in the form of dispersed active materials in carrier matrices. In certain selected aluminosilicate matrices like zeolites, it is possible to prepare, in addition to well dispersed materials, small clusters of metal and metal oxides confined

in cavities. In most cases the knowledge about structure of the active material is very useful to correlate the activity of the catalyst for a given chemical transformation.

Experimental development of in situ XAS methods combined with mass spectrometry or Raman/IR and UV/Vis spectroscopy provide vital clues about the catalyst during the reaction. Ruthenium based catalysts are widely investigated for their electro catalytic activity and platinum group metals have been known to catalyze several reactions of industrial significance and also find application in energy systems like fuels cells as catalyst coating.

Despite experimental developments, certain limitations exist in the interpretation of the results presented by these advance techniques. Therefore parallel to technical developments, maximum utilization of the experimental data to derive useful information is also very important. In this direction, the development of wavelet based time-frequency analysis for x-ray and neutron scattering data on silicon glasses has been developed and this method has been extended to the evaluation of XAS data to extract better information from an experiment.

In this thesis, XAS technique is prominently used to investigate metals and metal oxide catalysts dispersed in inorganic matrices. Structure of the catalysts, effect of gas adsorption on zeolite based catalysts, kinetic studies of CO interaction with platinum clusters, highly dispersed ruthenium oxide clusters in zeolites have been studied in detail. Theoretical wavelet based methods for EXAFS analysis has been proposed as an additional evaluation step to interpret XAS data.

Bridging the gap between the fundamental understanding of how materials work and how the structure of the material, both physical and electronic affect different properties of the materials is an enormous task considering the vast array of materials available today. But, a small but sure step in this direction to augment the knowledge about catalysts with possible technical applications in sustainable energy systems has been attempted in this thesis work.



## 2. XAS investigation of platinum clusters in zeolite Y

### 2.1. Introduction

Metal catalysts are widely used in the industry for refining of petrochemicals, conversion of automobile exhaust gases, hydrogenation of carbon monoxide, hydrogenation of fats and many other processes. The metal used is often expensive and may constitute only about 1 wt% of the catalytic material and is applied in a finely dispersed form as particles on a high surface area porous metal oxide support. The smaller the metal particles, the larger the fraction of the metal atoms that are exposed at surfaces, where they are accessible to reactant molecules and available for catalysis. These supported metal catalysts can be prepared by impregnation of a porous support (e.g., faujasite zeolite) with an aqueous solution of a metal salt (e.g., tetraamineplatinum chloride), followed by heating in air (calcination) and reduction in hydrogen. The resulting product typically consist of metal particles distributed over the surface of the support and in the pores. Most support surfaces are structurally nonuniform and supported metal particles are also often nonuniform in size and shape, and too small to be structurally characterized precisely. As a result the structures of supported metal catalysts are not well understood.

#### 2.1.1. Supported metal catalysts

Supported platinum catalysts are an important class of monometallic catalysts with wide range of commercial applications [4–6]. Due to its importance as a catalyst, several investigations on the structure platinum particles in various supports has been carried

out [7–11]. Supported platinum clusters are structurally sensitive to reactive gases and studies of the geometric changes of the metal particles and the electronic effects of the reactive gases on platinum have been carried out [8, 12–17].

### 2.1.2. Formation of metal clusters in zeolite cages by reduction of ion exchanged cations

Zeolite-supported metal clusters have most commonly been prepared by ion exchange followed by reduction [18]. Usually the metals are introduced as cationic complexes, (e.g.,  $[\text{Pt}(\text{NH}_3)_4]^{2+}$ ) that replace cations such as  $\text{Na}^+$  in the zeolite and are then decomposed by heating in  $\text{O}_2$  or air and reduced in  $\text{H}_2$ . Reduction of metals in zeolites often leads to metal clusters or particles that are too large to fit in the cages, and it may then be accompanied by the breakup of the zeolite framework and/or migration of the metal outside the cages. Cations of noble metals in zeolites are easily reduced by  $\text{H}_2$ , but proper activation and reduction treatments that give the highest metal dispersions are difficult to achieve.

Appropriate treatments of ion-exchanged zeolites are needed to minimize migration and sintering of the metal and to produce uniform size distribution. For example, prior to reduction in  $\text{H}_2$ , it is usually necessary to eliminate  $\text{NH}_3$  produced by thermal decomposition of  $\text{NH}_4^+$  ions or amine complexes, because reduction of metal ions in the presence of evolving  $\text{NH}_3$  leads to agglomeration of the metal. Direct reduction of noble metal cations by  $\text{H}_2$  at high temperatures may lead to formation of neutral metal hydrides, which are mobile, again causing metal agglomeration and low metal dispersion. Water is also considered to be detrimental to high metal dispersion.

Despite all these difficulties, proper selection of the temperature and duration of calcination and reduction can lead to the formation of well dispersed metal particles in the zeolite material. Activation in flowing  $\text{O}_2$  prior to reduction in  $\text{H}_2$  also gives highly dispersed platinum clusters in zeolites. Ciccariello et al. [5] showed that for a 2.98 wt% Pt/NaY catalyst sample, calcination performed for 4 h at 250 °C yields very dispersed metal particles.

In this chapter the experiments and results of the XAS investigation on platinum dispersed in NaY zeolite material carried out to determine the local structure of platinum

and in turn to derive information about their size and location in the zeolite matrix are presented. Since very small clusters of platinum are known to be very sensitive to air [19], the formation of platinum clusters from an oxidized precursor has been completely carried out in a in situ XAS reactor with high flux of hydrogen gas. The hydrogen rich platinum material was subsequently subjected to argon gas flow and CO addition. In order to register the changes that take place to the local environment of platinum during these treatments, in situ XAS measurements were carried out. The experimental conditions used in this process are discussed in the following section and the XAS results of the investigation are presented and discussed with respect to the changes that take place to the local environment of platinum in NaY zeolite.

## 2.2. Experimental method

The XAS experiments were carried out at beamline X1 of Hasylab at DESY Hamburg, Germany. A Si (111) double crystal monochromator detuned to 65% of the intensity to remove higher harmonics was used for the energy scans. All spectra were recorded in transmission mode using ionization chambers filled with argon gas to achieve optimal absorption and signal to noise ratios. Energy calibration was performed using a platinum metal foil, which was measured simultaneously with every sample. The oxygen calcined Pt/NaY samples were pressed into pellets (13 mm diameter) and placed in a stainlesssteel in situ cell connected to a gas flow regulator system. Heating rate regulation and temperature registration of the reaction cell was achieved using an Eurotherm controller.

Detailed description of the XAS in situ setup used for the investigation is presented in section 5.1.3 of chapter 5. XAS scans at the Pt  $L_3$  edge (11564 eV) were performed at room temperature after in situ reduction in a  $25 \text{ mL min}^{-1}$  flow of  $\text{H}_2$  at 473 K for 1 hour, after argon gas flow at  $50 \text{ ml min}^{-1}$  for 10 min, and after CO gas flow at  $25 \text{ ml min}^{-1}$  for 20 min. Quick-XAS (Q-XAS) scans were performed during CO flow and hydrogen pre-treatment, with an approximate time resolution of 40 s. The gas flow through in the XAS cell was maintained at 1 bar over pressure with regulative one-way valves. The investigated samples and the physical conditions in which the XAS measurements were carried out for each sample are presented in table 2.1 for a quick overview.

## 2. XAS investigation of platinum clusters in zeolite Y

---

Sample	Prepared at	Measurement at
6 wt% Pt-O <sub>x</sub> /NaY (as prepared)	573.15 K	rt
6 wt% Pt-H <sub>2</sub> /NaY (Pt <sub>13</sub> H <sub>m</sub> /NaY)	475.15 K	rt
6 wt% Pt-Ar/NaY (Pt <sub>13</sub> /NaY)	rt	rt
6 wt% Pt-CO/NaY (Pt <sub>x</sub> (CO) <sub>y</sub> /NaY)	rt	rt
Pt metal foil	–	rt

Table 2.1.: List of all the platinum samples and the their treatment conditions before XAS measurements

### 2.2.1. Data evaluation

The XAS spectra measured in the energy scale is subjected to data evaluation, which involves background absorption correction, normalization and background subtraction<sup>1</sup>. The extracted EXAFS function was transformed to  $k$ -space by choosing suitable threshold energy from half the absorption edge step. EXAFS data analysis was performed in  $k$ -space.

The fit of the calculated EXAFS function to experimental data was obtained by the adjustment of the common theoretical EXAFS expression according to the curved wave formalism of EXCURV98 [2]. The potential and phase shifts in this program were calculated by employing Hedin-Lundquist for the exchange potential and van Barth for the ground state potential. The amplitude reduction factor was determined to be 0.8 and was fixed during the iteration procedure [20]. When fitting experimental data with theoretical models, a correction term  $E_f$  was introduced that accounts for an overall phase shift between the experimental and calculated EXAFS spectrum. The quality of the fit is given in terms of the R-factor.

---

<sup>1</sup>For details about the data reduction and evaluation steps refer to Appendix

## 2.3. Results and discussion

### 2.3.1. XANES investigation

Pt L<sub>3</sub> edge XANES spectra of Pt metal foil and other Pt samples mentioned in table 2.1 are given in figure 2.1. From the figure, it can be seen that both the shape and the intensity of the white line of the XANES are found to be completely different for the investigated samples, although the absorption edge positions are similar to those of the reference metal foil. Compared to the metal foil, the calcined sample exhibits a relatively intense white line which is found to decrease in intensity upon reduction and further upon argon purging, but it is still larger than that for the metal foil. Upon CO adsorption, there is again a strong increase in the white line intensity.

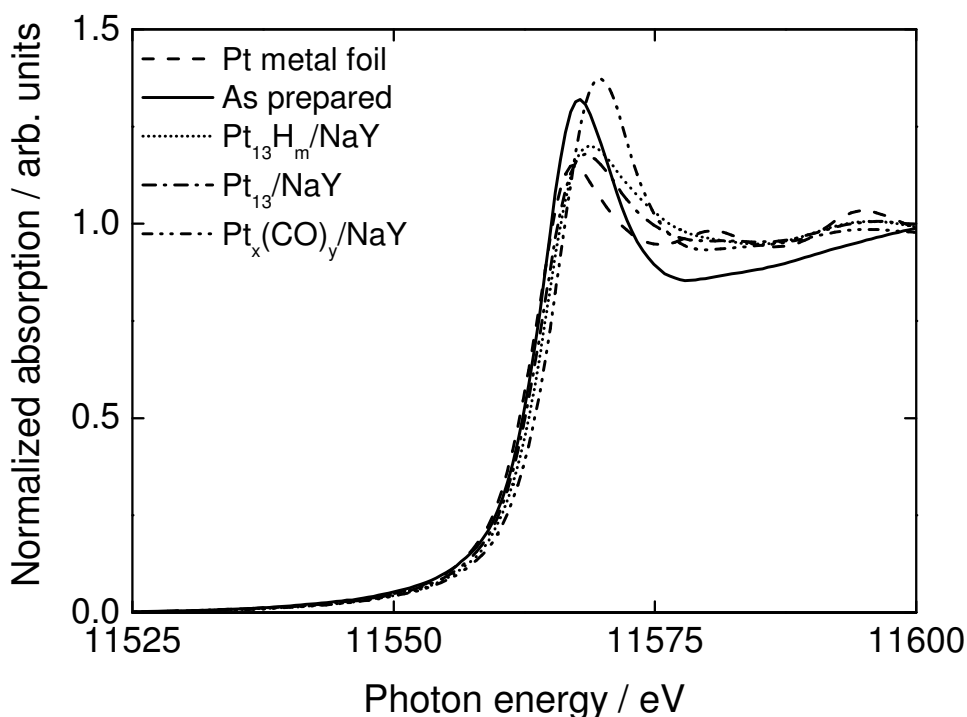


Figure 2.1.: XANES measured at the Pt L<sub>3</sub> edge (11564 eV) for the samples investigated

The XANES region of the samples investigated, given in figure 2.1 shows the difference in shape and height of the white line in the case of the sample prepared by oxygen calcination prior to in situ reduction, after hydrogen reduction and after subsequent argon purging and CO adsorption. Using Q-XAS and the possibility to switch gases and

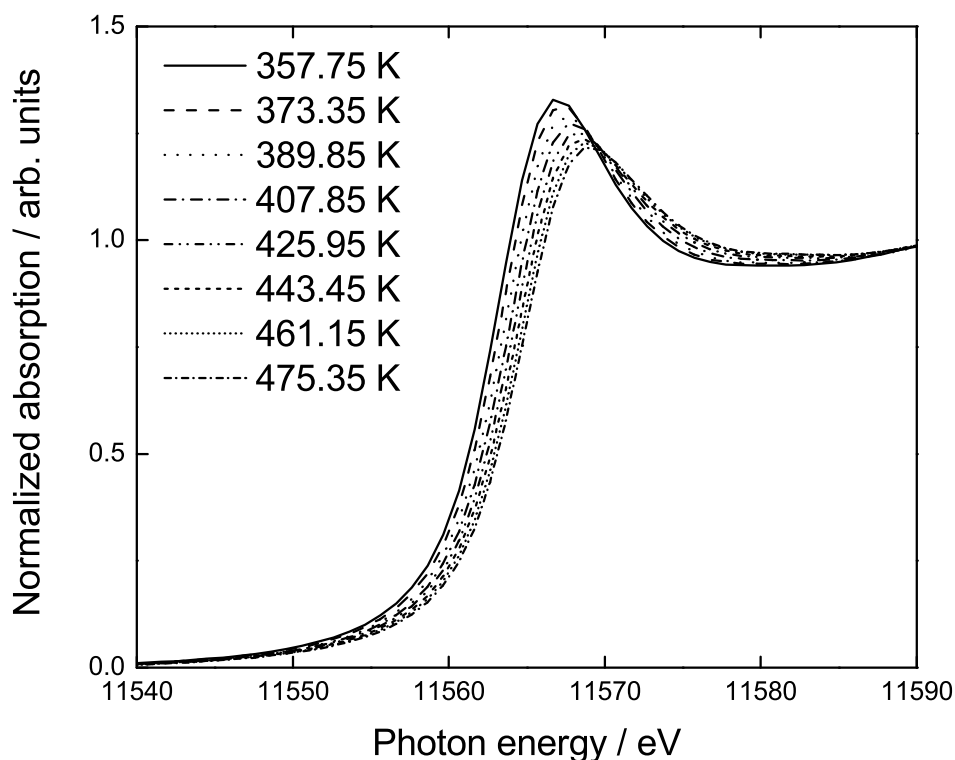


Figure 2.2.: Q-XAS Pt L<sub>3</sub> edge (11564 eV) spectra collected during the temperature treatment under hydrogen gas flow of the as prepared (oxygen pre-calcined) sample

monitor the temperature of the reactor, in addition to the steady state XAS measurements, a series of spectra in a continuous scanning mode were measured during the hydrogen reduction and CO addition. Platinum species in the oxygen calcined sample has a strong white line characteristic of platinum oxide [19] whereas reduced metallic platinum has different white line intensity as well as peak position.

XAS can probe local geometry and at the same time give information that is averaged over all the absorbing centers. Therefore, with the help of Q-XAS it was attempted to monitor in situ the onset of reduction (temperature at a given hydrogen flow rate) as well as the time it takes, after reaching 475.15 K, to observe reduced platinum species. Scans lasting 45 s were carried out during the temperature ramp at the rate of 5 K min<sup>-1</sup>. For reasons of clarity, Q-XAS spectra collected at larger steps of temperature are presented in figure 2.2 from 357.75 K up to 475.35 K and in time steps of 180 s after

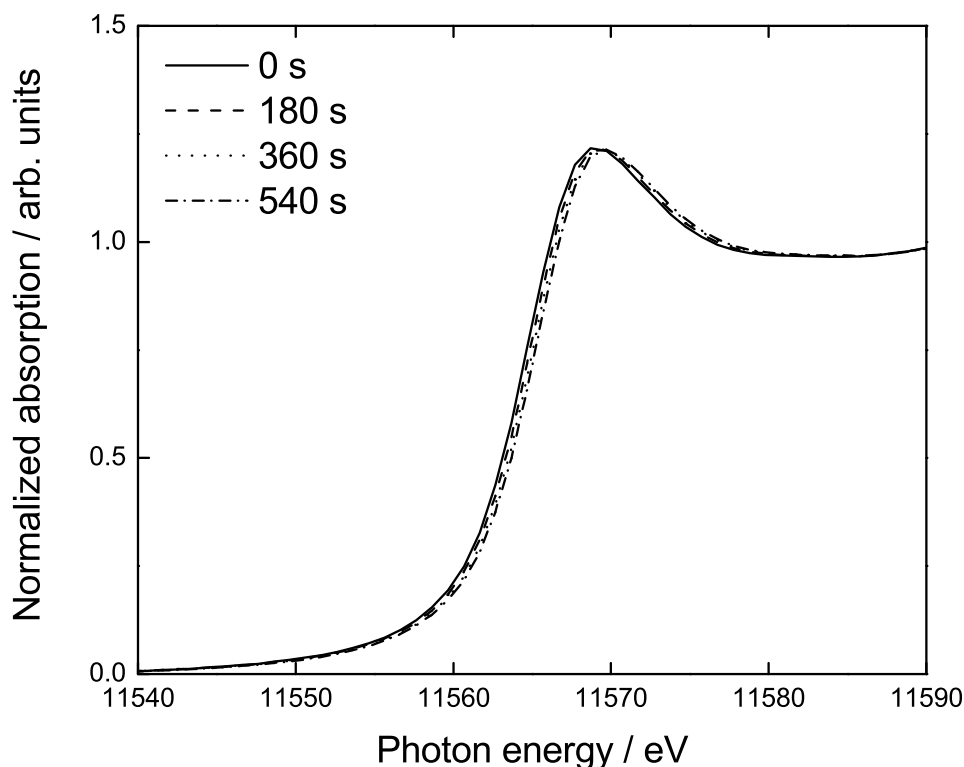


Figure 2.3.: Q-XAS Pt L<sub>3</sub> edge (11564 eV) spectra collected after reaching 475.35 K during the temperature treatment under hydrogen gas flow of the as prepared (oxygen pre-calcined) sample

reaching 475.35 K in figure 2.3. Curve fitting of Q-XAS spectra carried out during CO addition is presented in section 3.2.2 of chapter 3 and only the XANES spectra subjected to the fitting process is presented here in figure 2.4. Upon CO interaction, the white line intensity is found to increase along with a parallel change in the shape of the white line which is indicated by an arrow in the figure.

Qualitatively, from the Q-XAS spectra during temperature treatment, XANES features similar to reduced platinum species is already observed during the first few minutes after reaching 475.35 K indicating that mild reduction conditions are sufficient to produce reduced platinum species for a well dispersed Pt catalyst. Moreover, it also provides vital clues to the temperature and time regime where reduction and further migration of the reduced species could take place in the zeolite. Additionally, the observations also demonstrates the utility of in situ XAS set up and Q-XAS technique to monitor heterogeneous catalytic reactions in real time.

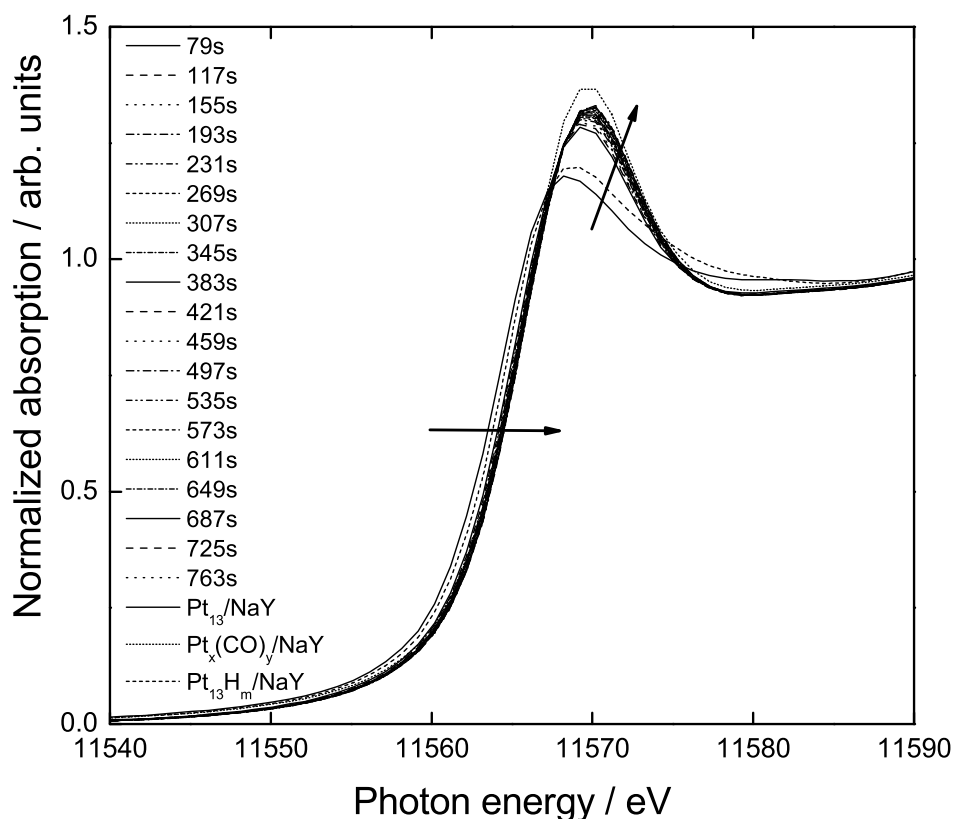


Figure 2.4.: Q-XAS Pt L<sub>3</sub> edge (11564 eV) spectra during CO interaction with platinum cluster at room temperature

The L<sub>3</sub> edge resonance in platinum corresponds to the 2p<sub>(3/2)</sub> to 5d transition. Platinum has electronic configuration given by 5d<sup>9</sup>6s<sup>1</sup> in its ground state and the unoccupied d level is denoted as d<sub>(5/2)</sub>. Depending upon the d electron vacancies in the final state, the intensity of the white line varies. Increase in white line intensity for hydrogen reduced small Pt clusters compared to Pt metal foil has been attributed to changes in d electron vacancies [16]. However in the present case, both the effect of cluster size and the effect of hydrogen adsorption, play a role. In order to decouple these two effects, one has to measure the XANES for bare clusters and hydrogen adsorbed clusters. In this respect, upon Ar purging, reduction in intensity and width of the white line is observed which could be attributed most likely to the partial or complete desorption of hydrogen, although complete desorption could possibly be verified only by using a mass spectrometer connected to the exhaust gas line from the XAS cell. Upon CO adsorption, the increase in the intensity of the white line could be attributed to the bond formation of



Pt with CO. Thus platinum atoms have lower electron density by  $\pi$ -back donation from Pt to CO or a partial positive charge on Pt, or a combination of both [14]. Qualitatively, on passing from the metal foil to smaller clusters in the zeolite with adsorbed hydrogen or CO, the changes in the white line are attributed to increase in d-electron vacancies.

### 2.3.2. EXAFS investigation

XAS measurements and analysis of reduced Pt samples in NaY zeolite prepared in ex situ using similar conditions has already been reported in literature [20]. In contrast to that earlier work, in the present work, the Pt cluster preparation has been carried out under in situ conditions under a high flux of reactant gases so that air oxidation of Pt can be safely ruled out. The experimental and fitted EXAFS functions in  $k$ -space and the corresponding Fourier transforms in real space of platinum clusters after in situ reduction are presented in figure 2.5. The local structure around Pt in Pt<sub>13</sub>H<sub>m</sub>/NaY obtained from the fit, the parameters used in the fitting procedure, the resulting fit parameters, and the estimated errors in their determination are given in 2.2.

In the experimental phase corrected Fourier transformed EXAFS function, one intense peak at around 2.7 Å is observed along with a smaller side lobe at roughly 1.8 Å. It was verified by fitting the experimental spectrum with a theoretical spectrum calculated using only Pt, and oxygen shell at a larger distance. Therefore this peak is certainly not a structure feature from lighter backscattering elements like oxygen which might be present at this distance. This feature can either be due to the complicated structure in the phase and amplitude functions for heavy atoms [21] or Fourier transform truncation errors or a combination of both. However, the contribution of truncation error to this peak could only be minimum due to the usage of a window function over a large  $k$ -range of 3–17 Å<sup>-1</sup> for the Fourier transformation of the EXAFS signal.

In the experimental EXAFS spectrum shown in figure 2.5, only one intense peak at roughly 2.7 Å is present. As further peaks with comparable intensities which are normally present in larger platinum clusters or bulk platinum metal are absent, the addition of higher shells of Pt in the fitting did not give a significant improvement of the fit. The peak at 2.7 Å could be fitted with Pt at 2.77 Å as well as O at 2.72 Å with average coordination numbers of 5.8 and 3.8, respectively. Considerable improvement in the quality of fit justified the inclusion of this oxygen shell in the modeling.

## 2. XAS investigation of platinum clusters in zeolite Y

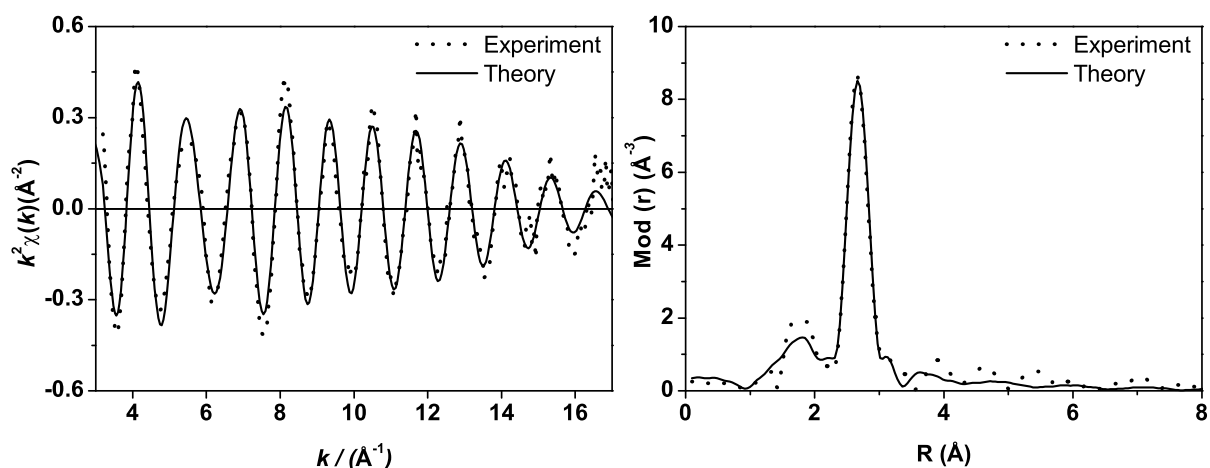


Figure 2.5.: Experimental EXAFS function (left), its Fourier transform (right) and fit to the experimental data of  $\text{Pt}_{13}\text{H}_m/\text{NaY}$

The first shell Pt–Pt average coordination number indicates strongly that very small, probably 13 atom clusters are formed in NaY zeolite. However, despite the small cluster size of circa 0.8 nm, the observed Pt–Pt distance is comparable with the bulk platinum value of 2.77  $\text{\AA}$ , due to the structural relaxation effect by the adsorbed hydrogen atoms. The presence of longer Pt–O distance compared to that observed in  $\text{PtO}_2$ , 2.0  $\text{\AA}$  and the absence of any oxygen shell at this distance exclude the possible oxidation of the platinum clusters and emphasize the necessity of using in situ reduction to characterize such samples. Average coordination number of 5.8 obtained for Pt–Pt shell is compatible with the presence of 13 atom clusters and but that certainly does not exclude other possibilities where a distribution of different cluster sizes exist. A cluster of 13 Pt atoms could also very well fit into the super cages of NaY zeolite with a larger free diameter. In addition, a second shell of oxygen atoms is present at 2.72  $\text{\AA}$  due to contributions from zeolite oxygen [17] and such long Pt–O distances are induced by interfacial hydrogen after reduction [15].

### Effect of CO adsorption

For  $\text{Pt}_x(\text{CO})_m/\text{NaY}$ , the experimental  $k^2$  weighted EXAFS function  $k^2\chi(k)$ , its Fourier transform along with the fit to the data are given in figure 2.6, and the comparison of the experimental spectra alone with  $\text{Pt}_{13}\text{H}_m/\text{NaY}$  is shown in figure 2.7.

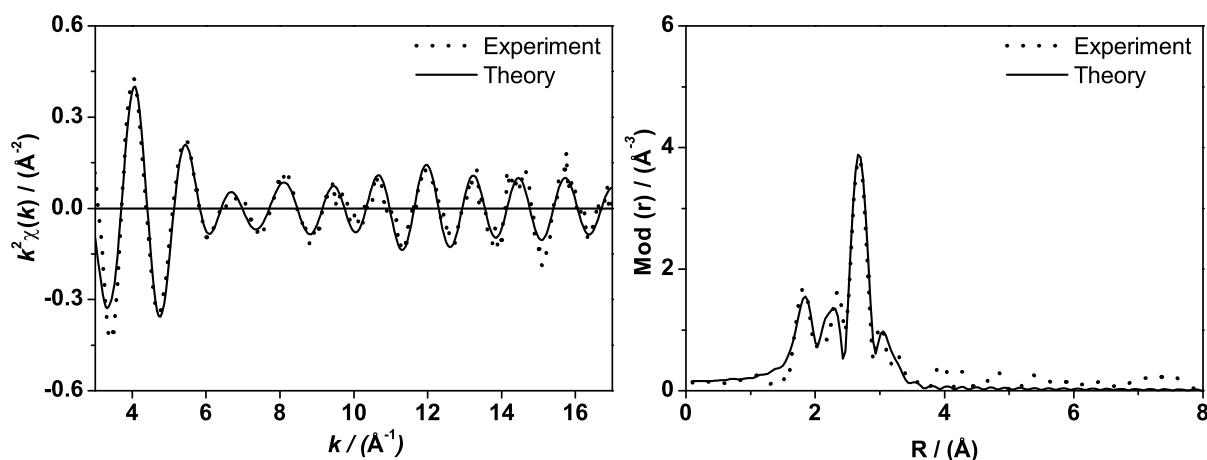


Figure 2.6.: Experimental EXAFS function (left), its Fourier transform (right) and fit to the experimental data of  $\text{Pt}_x(\text{CO})_m/\text{NaY}$

From figure 2.7 significant changes in the EXAFS spectrum upon CO exposure at room temperature can be observed. Changes in the backscattering amplitude, which is the envelope in the EXAFS function, is observed at both low and high  $k$  values. After CO adsorption oscillations in the  $k$ -range range of  $7\text{--}14 \text{ \AA}^{-1}$ , relevant for heavy elements are suppressed, whereas strong oscillations remain in the range  $3\text{--}7 \text{ \AA}^{-1}$ . A considerable decrease in the intensity of the Fourier transform peak near  $2 \text{ \AA}$  is noticed after CO adsorption. In order to quantify the observed changes, experimental spectra were fitted with relevant structure models consisting of Pt–C, Pt–O, and Pt–Pt contributions. Based upon the quality of fit, the most probable structure and eventually the local structure parameters such as average coordination number, average inter-atomic distance and EXAFS Debye-Waller factor for different shells were obtained. The fit results for the different samples considered here are tabulated in table 2.2.

For the CO adsorbed platinum cluster, the model consists of one Pt–Pt, two Pt–C, and one Pt–O (zeolite oxygen) shells. The Pt–Pt distance in  $\text{Pt}_x(\text{CO})_m/\text{NaY}$  contracts to  $2.69 \text{ \AA}$  from  $2.77 \text{ \AA}$ , together with a decrease in the Pt–Pt average coordination number from 5.8 to 0.9. Two Pt–C contributions, one at  $1.95 \text{ \AA}$  and the next at  $2.14 \text{ \AA}$  are obtained with average coordination number of 0.8 and 1.7 respectively.

The preparation of Pt cluster has been carried out under in situ conditions with a high flux of reactant gases so that air oxidation can be safely ruled out. Additionally, the effect of subsequent CO adsorption on the platinum clusters has been investigated.

## 2. XAS investigation of platinum clusters in zeolite Y

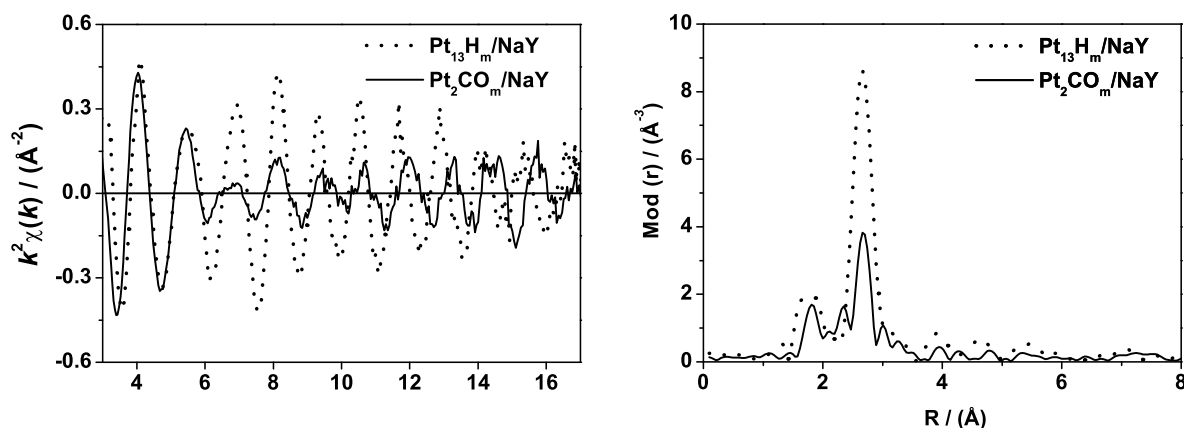


Figure 2.7.: Experimental EXAFS function (left), its Fourier transform (right) of  $\text{Pt}_{13}\text{H}_m/\text{NaY}$  and  $\text{Pt}_x(\text{CO})_m/\text{NaY}$

Insights into the size of the cluster, their location in the zeolite matrix, and the effect of CO adsorption were obtained from the analysis of the local structure around Pt.

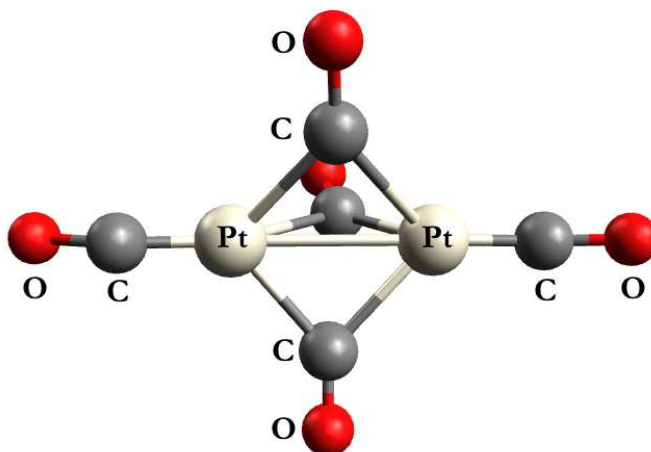


Figure 2.8.: The schematic structure of  $\text{Pt}_2(\text{CO})_m$  in NaY with possible CO bonding scenario

Analysis of  $\text{Pt}_{13}\text{H}_m/\text{NaY}$  after CO adsorption revealed a decrease in Pt-Pt average distance which is very similar to that observed for  $[\text{Pt}_2\text{Br}_2\mu\text{-(CO)}(\text{PPh}_3)]$  compounds with Pt-Pt distance of 2.65  $\text{\AA}$  [22]. The changes in the structure parameters indicate reconstruction of the  $\text{Pt}_{13}$  clusters into smaller aggregates, most likely  $\text{Pt}_2$ . Furthermore, two different Pt-C contributions are obtained. The short Pt-C distance is similar to the

Sample	Abs-Bs <sup>a</sup>	CN(Bs) <sup>b</sup>	R(Bs) <sup>c</sup> Å	$\sigma^d$ Å	$E_F^e$ eV	$k$ -range Å <sup>-1</sup>	R-factor
Pt <sub>13</sub> -H <sub>m</sub> /NaY	Pt-Pt	5.8±0.6	2.77±0.03	0.084±0.001	-10.02	2.92–17.03	24.48
	Pt-O	3.8±0.4	2.72±0.03	0.050±0.001			
Pt <sub>x</sub> (CO) <sub>m</sub> /NaY	Pt-C	0.8±0.1	1.95±0.02	0.055±0.001	-13.44	2.90–17.01	34.73
	Pt-C	1.7±0.2	2.14±0.02	0.092±0.009			
	Pt-Pt	0.9±0.1	2.69±0.03	0.059±0.001			
	Pt-O	4.6±0.7	2.72±0.03	0.081±0.001			

Table 2.2.: Fit results of the EXAFS data of samples Pt<sub>13</sub>-H<sub>m</sub>/NaY and Pt<sub>x</sub>(CO)<sub>m</sub>/NaY.

<sup>a</sup>Absorber(Abs)-back scatterer(Bs). <sup>b</sup>Average coordination number(CN).

<sup>c</sup>Inter atomic distance. <sup>d</sup>EXAFS Debye-Waller factor( $\sigma$ ) with its estimated deviation. <sup>e</sup>see text in section 2.2.1

Pt-C distance observed in compounds like Pt<sub>3</sub>(CO)<sub>6</sub> where CO molecules coordinated to Pt in a linear and bridge like fashion [23]. Therefore, with further evidence from infra red (IR) spectroscopy results from Akdogan [24], it can be inferred that in the present case also, one linear and two bridged CO molecules coordinate to Pt.

A second EXAFS contribution is present at 2.72 Å due to zeolite oxygen with an average coordination number of 4.6 indicating that the Pt carbonyl clusters are in proximity to the zeolite framework. This observation could be attributed to the stabilizing effect of zeolite oxygen atoms on the carbonyl clusters [14,25,26] which are otherwise known to be unstable. Small and most probably, mono disperse Pt<sub>13</sub> clusters in NaY zeolites are very reactive towards CO at room temperature. CO adsorption leads to a complete decomposition of the cluster and to the formation of Pt<sub>2</sub>(CO)<sub>m</sub>/NaY species most probably stabilized by the zeolite walls as shown in figure 2.8.



# 3. Parameterization of resonance absorption at the L edges of Pt

## 3.1. Introduction

In the field of catalysis research arriving at correlation between chemical and electronic properties of a catalyst has been popular and at the same time challenging [27], like for example the establishment of a relationship between the catalytic activity and d-band character of platinum metal catalysts. In this respect, the possibility to obtain the d-band character directly from the white lines in the x-ray absorption edge structure has received considerable attention [28].

In a core-level absorption spectrum, the behavior of the absorption coefficient  $\mu$  of an element is studied as a function of photon energy. The absorption coefficient usually increases dramatically when the photon energy approaches the binding energy of a core level. In certain cases, at photon energies less than the ionization energy of the core level, bound state to bound state transition takes place resulting in well defined absorption features called white lines [29].

The white line primarily probes the unoccupied densities of d states of the metal in the vicinity of Fermi level [3]. Several early observations that the intense white lines are stronger in supported metal catalysts compared to pure metals and that the gas adsorption of the supported catalysts influenced the shape and intensity of white lines lead to a strong interest in parameterization of the white lines [30–35].

A summary of absorption edges of the elements is presented in figure 3.1. In this figure, the electronic shells are labeled as  $(n l_j)^{2j+1}$ , where  $n$ ,  $l$  and  $j$  are the principal, orbital angular momentum, and total angular momentum quantum numbers of the single-electron states,  $(2j+1)$  gives the multiplicity.

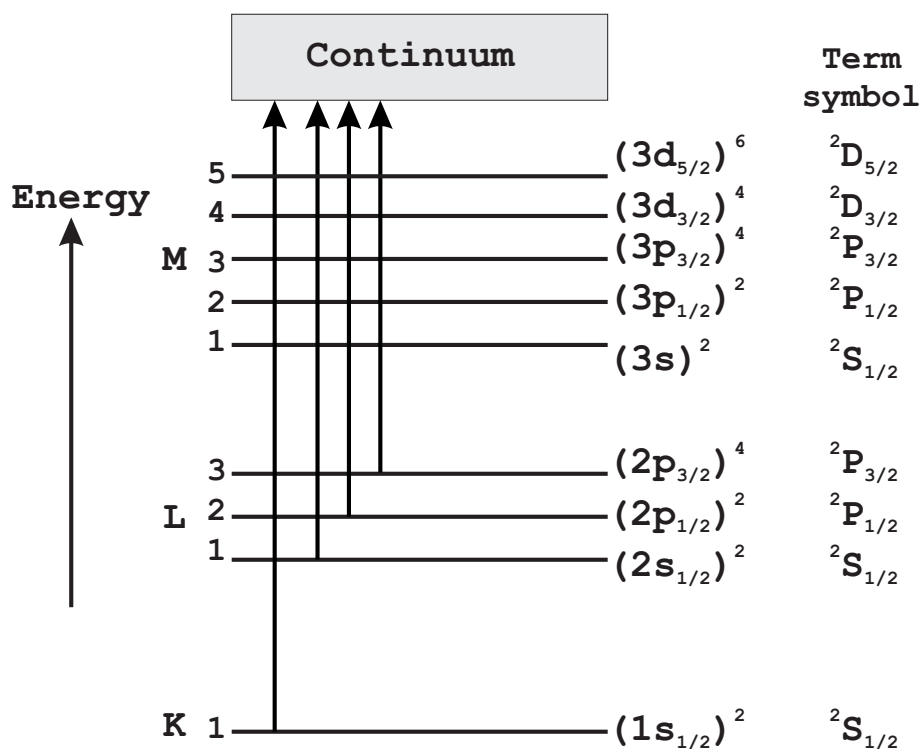


Figure 3.1.: Absorption edges of elements with the electronic shells

### 3.1.1. White lines

Historically, the absorption feature occurring just above the edge on the high energy side was denoted as the Kossel structure and the strong peak near the x-ray absorption edge as a white line or raie blanche (in French) [30]. At the time when this phenomenon was first observed x-rays were detected photographically and the large absorption peak appeared as an unexposed white line on the negative. The cause of the white lines has been qualitatively understood as due to a high density of final states or due to exciton effects [29].

Among K edge and L edge XANES, the L edge white lines are of particular interest in the study of electronic properties of materials because there are three different initial states,  $2s$  ( $L_1$ ),  $2p_{1/2}$  ( $L_2$ ) and  $2p_{3/2}$  ( $L_3$ ), that may be coupled to final states of p, s and d-character respectively [31]. At the  $L_1$  edge, the initial state which has angular momentum  $l=0$ , probes the unoccupied states of p ( $l=1$ ) while at the  $L_2$  and  $L_3$  edges, the initial states with angular momentum  $l=1$ , probe the unoccupied states of s ( $l=0$ ) and d ( $l=2$ ) character due to the selection rule,  $\Delta l = \pm 1$ .



Since one normally expects the s symmetric portion of the density of states to be small but spread out in energy, one does not expect white lines from this symmetry. However, the d symmetric distribution of the density of states can be large and narrow and is thus likely to produce white lines as illustrated in figure 3.2 reproduced from literature [31]. This tendency is verified experimentally and reported widely in literature [29]. Further, an exciton or bound state white line is characterized by a Lorentzian peak shape while a high density of states in a continuum produces an absorption peak which is skewed.

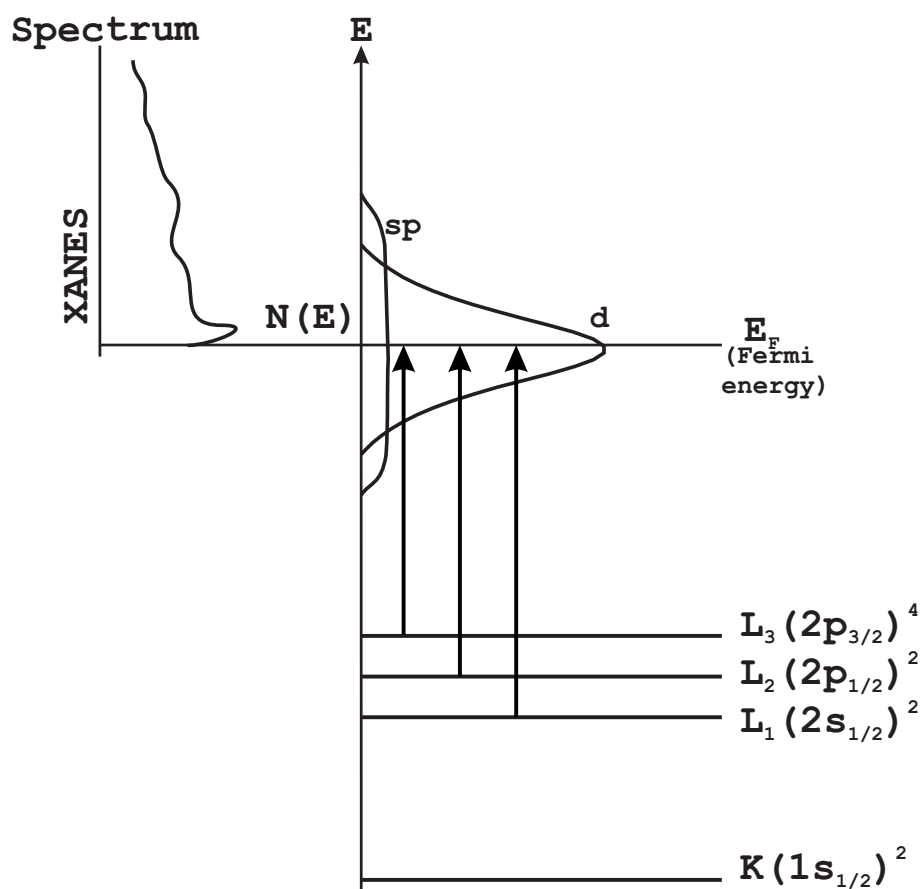


Figure 3.2.: Schematic diagram illustrating the photoabsorption process for noble metals and the resulting XANES spectrum.  $N(E)$  is the density of states which shows a characteristic narrow d-band and free-electron-like  $sp$ -band. White line feature in the XANES shown in the upper left hand side of the figure arise from dipole transitions from core levels to unoccupied states above the Fermi level

Wei and Lytle [30] have analyzed the line shape of the L edge white line of tantalum metal in detail and have found that the white line absorption envelope is slightly better described with a Fano type function than with a Lorentzian line shape, while Horsley [36] has used the scheme of a Lorentzian and an arctan function to describe the L<sub>2</sub> and L<sub>3</sub> edge white lines in a series of platinum and iridium compounds. However, in order to unambiguously answer the questions about the origin of white line intensities in metals, calculations like the one performed by Horsley [36], on relaxation effects after the excitation of a core electron to an excited state would be needed.

#### 3.1.2. L<sub>2</sub> and L<sub>3</sub> edges in Pt

White line in the XANES is only observed at the L<sub>3</sub> edge in platinum. At the L<sub>1</sub> edge there is no sharp line at the near edge region due to transitions into empty d states because the initial core states have s symmetry and thus would not have a significant transition probability to the empty d state due to dipole selection rule [37]. L<sub>2</sub> edge probes those final states which are characterized by a total angular momentum quantum number of ( $j=3/2$ ), while L<sub>3</sub> edge probes those states with total angular momentum quantum numbers ( $j=3/2$ ) and ( $j=5/2$ ) and is depicted in figure 3.3. For the absence of a strong peak at the L<sub>2</sub> edge, Mott [37] proposed that, if the unoccupied d states in platinum are predominantly states with total angular momentum ( $j=5/2$ ), then one expects transitions from L<sub>3</sub> ( $j=3/2$ ) but not from L<sub>2</sub> ( $j=1/2$ ) initial state because of the atomic dipole selection rule<sup>1</sup>  $\Delta j = 0, \pm 1$ .

---

<sup>1</sup>In the dipole approximation the transition is restricted by the following selection rules:

$$\Delta l = \pm 1 \tag{3.1}$$

$$\Delta j = 0, \pm 1 \tag{3.2}$$

where  $l$  is the orbital angular momentum quantum number and  $j$  is the total angular momentum quantum number with

$$j = l \pm \frac{1}{2}. \tag{3.3}$$

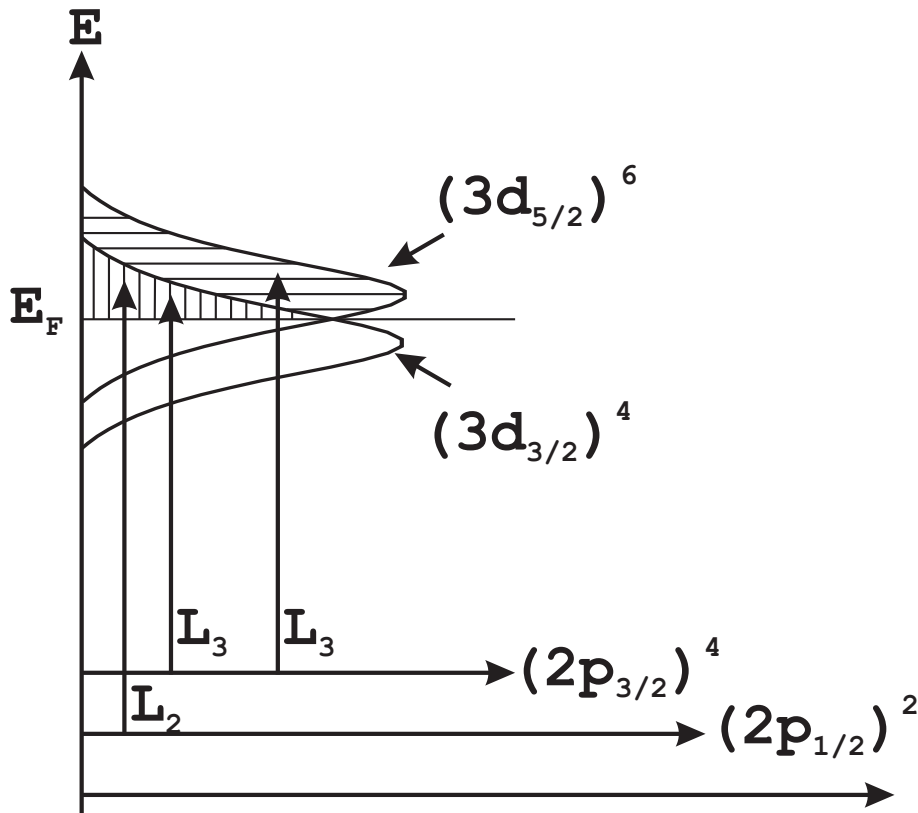


Figure 3.3.: A rough sketch of the density of states in platinum plotted versus energy for the  $L_2$  edge,  $L_3$  edge and conduction band including spin-orbit coupling. The shaded region indicate the unoccupied states above the Fermi level and the double feature in the d-band indicates splitting due to spin-orbit coupling (Reproduced from reference [1])

An exact description of the relationship between the  $L_2$  and  $L_3$  edge XANES and the number of d-band holes<sup>2</sup> around the absorbing atoms depends among many other effects, on many-body effects as well. However as Stern and Rehr mention [38], when a photoelectron either makes a transition into an initially empty shell (band) or fills that shell (band), the description of XANES reduce to an effective single-particle problem. The theoretical formulations on which the methods used in the following section are

<sup>2</sup>Given in simple terms, if  $n_{\text{holes}}$  denotes the number of d holes in the electronic ground state and  $n$  is the number of occupied d states, then

$$n_{\text{holes}} = 10 - n \quad (3.4)$$

based, use this simple description of XANES and apply to the description of platinum L edges. In platinum, as mentioned earlier, the electron transition fills the almost filled d shell (band) and the appropriate density of states to consider is that of the initial system before excitation and not the density of final states.

#### 3.1.3. Method used to extract d-band information

Based on these theoretical considerations, the technique outlined in literature for the extraction of number of unoccupied d states from the experimental Pt edge L<sub>2</sub> and L<sub>3</sub> edge XANES spectra will be applied to platinum containing NaY zeolite material with two different loadings (6 and 12 wt%), under different temperatures (rt and 473 K) and chemical treatments (H<sub>2</sub> or CO).

The absorption coefficient due to the initial-state electrons corresponding to L<sub>2</sub> or L<sub>3</sub> edges denoted as  $\mu_{L_i}$  can be written as a sum of contributions due to d states,  $\mu_{d_i}$  and s states  $\mu_{s_i}$ .

$$\mu_{L_i} = \mu_{d_i} + \mu_{s_i} \quad (3.5)$$

Due to the existence of the unoccupied d states in a narrow band of high density, a sharply peaked function whose area is proportional to total number of unoccupied d states is expected and  $\mu_{s_i}$  consists of the smooth absorption edge broadened by lifetime effects. Therefore isolation of  $\mu_{d_i}$  from  $\mu_{L_i}$  lies at the core of the problem in determining meaningful information from the area under the L edge white line.

Different types of functions are tested to approximate  $\mu_{s_i}$  and among them, assuming an arctan function for  $\mu_{s_i}$  has the disadvantage that the position of the center of the function (threshold energy) along x-axis (energy axis) is not known and should be guessed along with the scaling (or scaled to unity). Though similar uncertainty in scaling and threshold energy determination exists in the second method where the L<sub>2</sub> edge spectrum is subtracted from the L<sub>3</sub> edge spectrum, help is at hand in the form of the x-ray absorption cross section at higher energies (larger than 40 eV above the edge) which should be similar for both the edges. In other words the EXAFS oscillations in the two edges can be compared and aligned with each other to find a suitable threshold energy in a consistent manner.

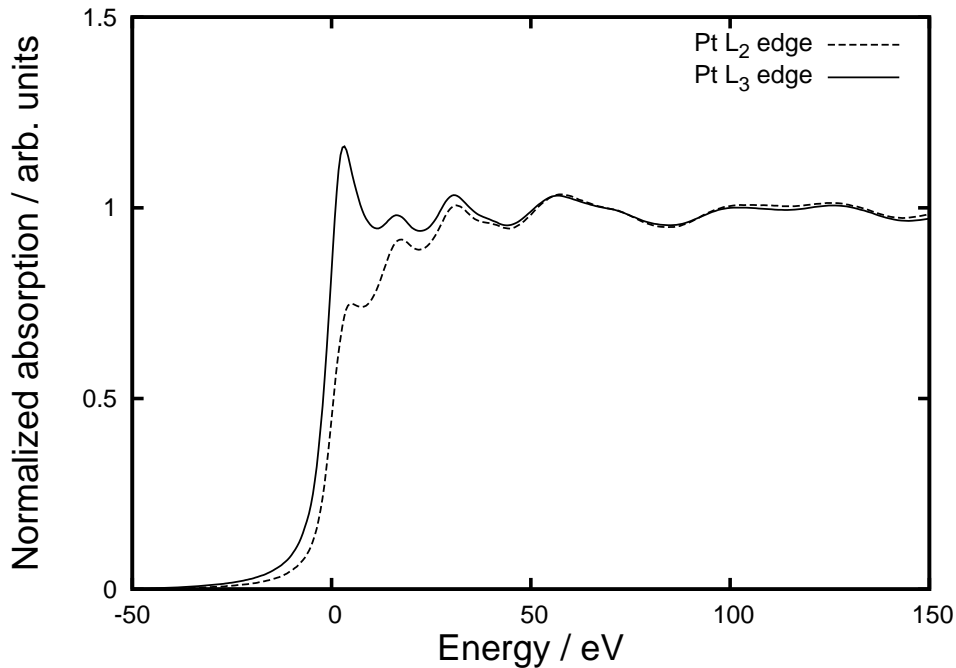


Figure 3.4.: Normalized L<sub>3</sub> and L<sub>2</sub> edge XAS spectra of Pt metal foil

For example, XAS spectra at L<sub>2</sub> and L<sub>3</sub> edges of Pt metal foil where the oscillations are found to be aligned, are shown in figure 3.4 with the zero in the x-axis corresponding to the inflection point in the absorption edges.

Another possibility to approximate  $\mu_{s_i}$  at the Pt edge is to use the featureless Au L<sub>2</sub> edge spectrum. This procedure can be used in order to determine the area under the white lines but here also the uncertainties mentioned above regarding the choice of threshold energy and scaling exist. Therefore, among the three methods available for approximation, the second method using the Pt L<sub>2</sub> edge was chosen for the analysis.

Further, as an alternative to find the total number of unoccupied d states Mansour, Cook and Sayers [1] proposed a method to determine the fractional change in the d-band vacancies relative to the reference material and this method is briefly outlined in the following section.

### 3.1.4. Absorption contribution of the white line

The total absorption  $A$ , contributed by a particular electronic transition or alternatively the total integrated area of the white line at a given edge can be described by equation 3.6:

$$A = \int \mu(E) dE \quad (3.6)$$

where  $\mu$  (in  $\text{cm}^{-1}$ ) is the linear absorption coefficient given by the exponential attenuation law,

$$I = I_0 \exp(-\mu x) \quad (3.7)$$

where  $I$  is the intensity transmitted through a sample of thickness  $x$  with incident intensity  $I_0$ . The linear absorption coefficient  $\mu$  (in  $\text{cm}^{-1}$ ) is related to the total atomic cross section  $\sigma$  (in  $\text{cm}^2/\text{atom}$ ) as

$$\mu = \frac{\rho N_A}{A} \sigma \quad (3.8)$$

where  $\rho$  is the mass density of the target material,  $N_A$  is the Avogadro constant and  $A$  is the atomic weight of the sample material.

Mass attenuation coefficient  $\mu_m$  (in  $\text{cm}^2/\text{g}$ ) is given by

$$\mu_m = \frac{\mu}{\rho} \quad (3.9)$$

Denoting the linear absorption coefficient  $\mu(E)$  near the  $L_2$  and  $L_3$  edges by  $\mu_2(E)$  and  $\mu_3(E)$  and on the basis of the theoretical treatment of the band structure of 5d transition metals by Mattheiss and Dietz [39], the following expressions 3.10 and 3.11<sup>3</sup> can be written for  $A_2$  and  $A_3$  for the bound state resonances.

$$A_2 = \int \mu_2(E) dE = \frac{CN_a \left(R_d^{2p_{1/2}}\right)^2 h_{3/2}}{3} \quad (3.10)$$

---

<sup>3</sup>Equations 3.10 and 3.11 were arrived at by using dipole selection rules while ignoring excitations to outer s states since the matrix elements for these transitions are much smaller than those for excitations to d states.

$$A_3 = \int \mu_3(E) \, dE = \frac{C N_a \left( R_d^{2p_{3/2}} \right)^2 (h_{3/2} + 6h_{5/2})}{15} \quad (3.11)$$

where  $C$  is an universal constant given in terms of fine structure constant  $\alpha$  as:

$$C = \frac{4\pi^2\alpha}{3} \quad (3.12)$$

with  $\alpha$  defined in terms of elementary charge  $e$ , vacuum permittivity  $\epsilon_0$  and speed of light  $c$  as<sup>4</sup>:

$$\alpha = \frac{e^2}{4\pi\epsilon_0\hbar c} \quad (3.13)$$

$N_a$  is the number density of the absorber,  $\left( R_d^{2p_{1/2}} \right)$  and  $\left( R_d^{2p_{3/2}} \right)$  are the radial dipole matrix elements for the excitation of  $2p_{1/2}$  and  $2p_{3/2}$  core electrons to the 5d state (these are assumed equal for the  $5d_{3/2}$  and  $5d_{5/2}$  states),  $h_{3/2}$  and  $h_{5/2}$  are the number of unoccupied d states of corresponding character in the valence band.

The difference in the integrated areas  $\delta A_2$  and  $\delta A_3$  of the  $L_2$  and  $L_3$  spectra of supported metal and bulk metal reference is given by equations 3.14 and 3.15 [33]:

$$\delta A_2 = \int \delta \mu_2(E) \, dE = \frac{C N_a \left( R_d^{2p_{1/2}} \right)^2 \Delta h_{3/2}}{3} \quad (3.14)$$

$$\delta A_3 = \int \delta \mu_3(E) \, dE = \frac{C N_a \left( R_d^{2p_{3/2}} \right)^2 (\Delta h_{3/2} + 6\Delta h_{5/2})}{15} \quad (3.15)$$

where  $\Delta h_{3/2}$  and  $\Delta h_{5/2}$  are the differences in the number of 5d holes of corresponding character between the supported and bulk metal. Normalization<sup>5</sup> to unit step height,

<sup>4</sup>This dimensionless collection of fundamental constants has a value close to  $(1/137)$  and is of broad significance because it is a fundamental constant for the strength of the coupling of a charge to the electromagnetic field [40]

<sup>5</sup>For a detailed description refer the Appendix

### 3. Parameterization of resonance absorption at the L edges of Pt

---

which is used typically in XANES analysis, rescales  $\delta A_2$  and  $\delta A_3$  to account for any differences in the radial integrals  $R$ , the degeneracy of the initial state and the concentration of the absorbing atoms [33].

From equations 3.14 and 3.15 it is clear that the difference in the integrated areas at the  $\delta A_2$  and  $\delta A_3$  is sensitive to difference in  $\left(R_d^{2p_{1/2}}\right)$  and  $\left(R_d^{2p_{3/2}}\right)$ . However, based on the following assumptions [39] that radial matrix elements  $R$  for both  $L_2$  and  $L_3$  edges are the same:

$$\left(R_d^{2p}\right) = \left(R_d^{2p_{3/2}}\right) = \left(R_d^{2p_{1/2}}\right) \quad (3.16)$$

and as Brown, Peierls and Stern [29] found, that if the  $L_2$  edge spectrum of platinum is renormalized by a factor of 2.22, it coincided with the  $L_3$  spectrum at energies 40 eV beyond the edge, equations 3.14 and 3.15 can be solved for  $\Delta h_{3/2}$  and  $\Delta h_{5/2}$ .

$$\Delta h_{3/2} = \frac{3\delta A_2}{C'} \quad (3.17)$$

$$\Delta h_{5/2} = 2.25 \times \frac{(3\delta A_3 + 1.11\delta A_2)}{C'} \quad (3.18)$$

where  $C' = C\left(R_d^{2p}\right)^2$ .

The total density of unoccupied states with d character  $\Delta h_{\text{total}}$  is given by equation 3.19.

$$\Delta h_{\text{total}} = \Delta h_{3/2} + \Delta h_{5/2} = \frac{2.22(\delta A_3 + 1.11\delta A_2)}{C'} \quad (3.19)$$

The explicit determination of  $\delta A_2$  and  $\delta A_3$  is difficult due to the complexity in the determination of  $\mu_{s_i}$  as well as  $C'$ . However, Mansour, Cook and Sayers [1] proposed that the fractional change in the number of d-band vacancies relative to a reference material can be more accurately determined by adopting a consistent approach to each data evaluation step. The fractional change in the number of d-band vacancies relative to a reference material is denoted as  $f_d$ :



$$f_d = \frac{\Delta h_{\text{total}}}{h_{\text{total}}} \quad (3.20)$$

where  $h_{\text{total}}$  refers to the reference material bulk platinum. Now, by expressing  $f_d$  in terms of the difference in areas  $\delta A_2$  and  $\delta A_3$  equation 3.21 is obtained:

$$f_d = \frac{(\delta A_3 + 1.11\delta A_2)}{h_{\text{total}}} \quad (3.21)$$

$h_{\text{total}}$  is known from band structure calculations for the element being investigated and is determined using the values for  $h_{\frac{3}{2}}$  and  $h_{\frac{5}{2}}$  reported by Mattheiss and Dietz [39]. Therefore the fractional change in the number of d-band holes in a sample compared to a reference (in the present case Pt metal foil is the reference) can be obtained quantitatively.

### 3.1.5. Deconvolution of XANES region

The broad  $L_2$  and  $L_3$  absorption edge resonances are superposed on a rising background step like function due to transitions to higher excited states and to the continuum. The XANES region could at first be assumed to have contributions from threshold resonances (peaked functions) and contributions from transitions to a continuum (step function or arctan function). The notion of resonances which are quite often presented in literature were examined from the view point of collision theory by Shore [41]. Rate coefficients or cross sections for collision processes, measured as a function of incident projectile energy  $E$ , often show abrupt variations (called resonances) as the energy passes some value  $E_0$ . Typically, this energy dependence (called profile) follows the simplified dispersion formula [41] given in equation 3.22:

$$Q(E) = C(E) + \frac{(\Gamma/2)B + (E - E_0)A}{(E - E_0)^2 + (\Gamma/2)^2} \quad (3.22)$$

where  $C(E)$  smoothly varies with energy, and  $B$ ,  $A$ ,  $E_0$  (resonance energy) and  $\Gamma$  (resonance width) are energy independent parameters. In addition to the above mentioned parameters, the observed line profiles are of course influenced by finite sample temperature, density and thickness effects. For inelastic collision processes, parameter  $A$  in equation 3.22 vanishes (see equation 3.23) and in absorption spectra such resonances

### 3. Parameterization of resonance absorption at the L edges of Pt

---

appear as absorption lines or spectral lines with a characteristic shape which is either symmetrical or skewed.

$$Q(E) = C(E) + \frac{(\Gamma/2)B}{(E - E_0)^2 + (\Gamma/2)^2} \quad (3.23)$$

Other equivalent parameterizations of the function  $Q(E)$ , like Fano profile [41, 42] given in equation 3.24, have also been suggested and used for white lines in tantalum [30]:

$$Q(E) = \sigma_b(E) + \sigma_a \frac{(\varepsilon + q)^2}{(\varepsilon^2 + 1)} \quad (3.24)$$

$$\varepsilon = \frac{(E - E_0)}{(\Gamma/2)} \quad (3.25)$$

indicates the deviation of the incident photon energy  $E$  from an idealized resonance energy  $E_0$  which pertains to a discrete auto ionizing<sup>6</sup> level of the atom [44]; this deviation is expressed in a scale whose unit is the half width  $(\Gamma/2)$ .  $Q(E)$  represents the absorption cross section for the photons of energy  $E$  whereas  $\sigma_a$  and  $\sigma_b$  represent two portions of the cross section corresponding, respectively, to transitions to states of the continuum that do and do not interact with the auto ionizing state.

---

<sup>6</sup>Attenuation occurs when an atom in state  $A$  absorbs a photon  $\gamma$  to produce the excited atomic state  $A^*$ :



The excited state subsequently decays by emitting one or more photons:



Since few emitted photons reappear in the direction of the incident beam, the encounter depletes the photon beam, and an absorption line develops (in a simplified picture). When the energy of  $A^*$  exceeds exceeds the first ionization limit, electron emission (or auto ionization) may also occur.



At higher energies, as initiated by x-ray photons, this decay process is commonly known as an Auger transition [43]. In turn, decay by photon or electron emission may occur through several decay channels. Auto ionizing states (also called compound states, resonance states, metastable states, collision complexes) can be formed by electron bombardment of  $A^+$  or by photoexcitation of  $A$ .

Concerning the shape of the mathematical function given in 3.22 the following observations are made [41]:

- When  $A = 0$ , the profile  $Q(E)$  is symmetrical about  $E_0$  3.23 usually called Lorentz profile when the background  $C(E)$  only varies smoothly with  $E$
- When  $A \neq 0$ , the profile  $Q(E)$  displays a dip on low energy side and a peak on the high energy side of  $E_0$

The x-ray absorption profiles that were fitted to the normalized XANES white lines of platinum L edge spectra were chosen to be either a Lorentzian distribution/Breit-Wigner profile or a pseudo-Voigt profile or a Fano type profile. The choice of the profile not only was based on the shape of the absorption line but also on the inherent connection to the dispersion formula just discussed briefly in the previous paragraph.

Summarizing the details discussed up until this point, the x-ray absorption edge of metals contains useful information about the local electronic structure. Parameterization of XANES region including the white line in x-ray absorption edges is one of the methods available to extract such information. Brown, Peierls and Stern [29] as well as Mattheiss and Dietz [39] demonstrated that, due to the fully screened core hole in platinum, the edge spectrum probes the unoccupied local partial density of ground state state. If the density of unoccupied states above the Fermi level is described as a step like function and the core hole as a state with width  $\Gamma$  due to its intrinsic life time, the absorption edge can be fitted with an arctan function given in equation 3.29.

$$F(E) = y_0 + \left(\frac{A}{\pi}\right) \arctan\left(\frac{E - E_0}{\Gamma}\right) \quad (3.29)$$

The inflection point of this step-like function gives the position of the Fermi level  $E_f$ .

In addition to this step-like function, L edges of transition metals exhibit a strong peak at threshold where the arctan function is strongly modified by transitions to the unoccupied d states. In platinum for example, the unoccupied density of states have a narrow bandwidth and the  $L_2$ - $L_3$  spin-orbit coupling is substantial (1.5 to 2.5 eV) [33] and the maximum of the white line corresponds to the Fermi level,  $E_f$ .

In the least-squares analysis of the XANES spectra the arctan function modified by a Lorentzian distribution, pseudo-Voigt profile (superposition of a Lorentzian distribution and a Gaussian function) and a Breit-Wigner-Fano type profile could be used. The profile

of these functions have theoretical counter part in the dispersion formula outlined and discussed in literature [41].

## 3.2. Results and Discussion

### 3.2.1. Quantitative determination of the number of d-electron states in Pt/NaY

In order to find out the change in the unoccupied d states of a Pt catalyst dispersed in zeolite material relative to bulk platinum and to obtain the effect of adsorbed hydrogen in altering the same, quantitative determination of the number of d electron states in platinum is necessary. After settling down with a systematic step-by-step approach built upon similar previous studies on platinum, evaluation of the changes that occur due to metal dispersion, gas adsorption and sample temperature, if any, were obtained for the samples listed in table 3.1. The XAS spectra of all the samples listed in table 3.1 were measured at the Pt L<sub>2</sub> and L<sub>3</sub> edges after in situ treatment at beamlines X1 and C at HASYLAB at DESY, Hamburg. Monochromator energy calibration was carried out with platinum metal foil as reference and data reduction steps of background subtraction and normalization was carried out based on the procedure outlined in the section of XAS data reduction in Appendix.

Pt L<sub>3</sub> and L<sub>2</sub> edge spectra of bulk metal and hydrogen adsorbed platinum sample, 12 wt% Pt-H<sub>2</sub>/NaY at 473 K are shown in figure 3.6 as a representative example of the differences in the near edge structure between the dispersed catalyst and the bulk metal. From an extended energy range beyond the near edge region in figure 3.5 the overlap of the EXAFS oscillations 40 eV after the edge can be observed.

Comparison of the L<sub>2</sub>, L<sub>3</sub> edges of Pt metal foil with each individual sample listed in table 3.1 are presented in figures 3.6, 3.7, 3.8, 3.9, 3.10, 3.11 and 3.12 in order to highlight the difference in white line shape and intensities of the samples with respect to bulk platinum metal.

In addition, the visible changes in the XANES region is also reflected in the estimated area under the curves given in table 3.2.

Sample	Temperature
12 wt% Pt-H <sub>2</sub> /NaY	473 K
12 wt% Pt/NaY	473 K
6 wt% Pt-H <sub>2</sub> /NaY	473 K
6 wt% Pt/NaY	473 K
Pt metal foil	rt
12 wt% Pt-H <sub>2</sub> /NaY	rt
6 wt% Pt-CO/NaY	rt

Table 3.1.: List of platinum in zeolite samples subjected to quantitative determination of d-electron states. Pt L<sub>2</sub> and L<sub>3</sub> edge XAS spectra were measured after in situ treatment at the above mentioned measurement conditions

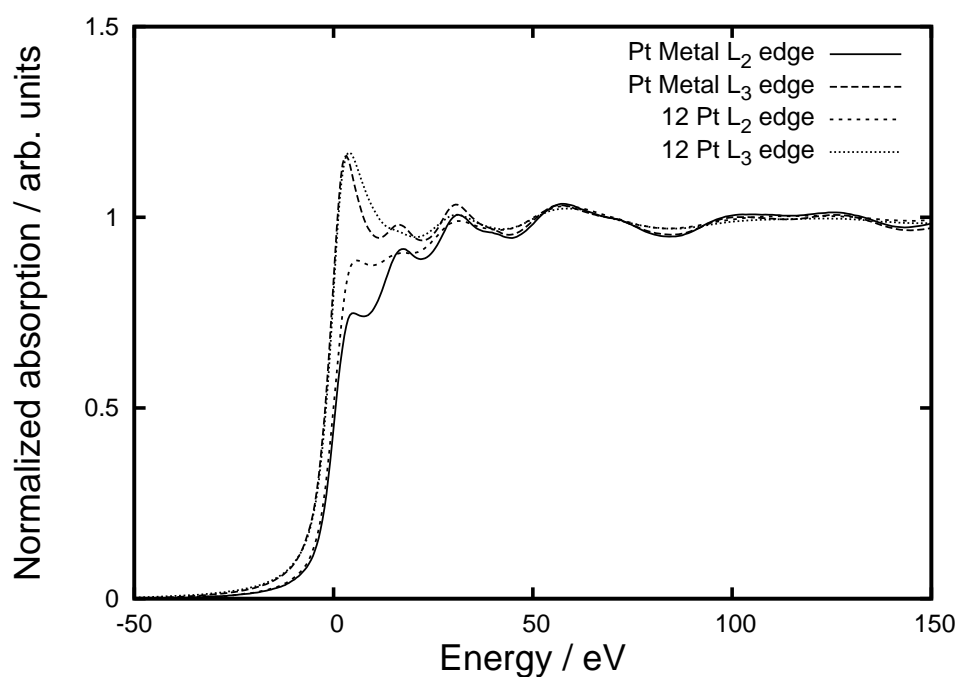


Figure 3.5.: Comparison of the L<sub>2</sub>, L<sub>3</sub> edges of Pt metal foil and 12 wt% Pt-H<sub>2</sub>/NaY at 473 K

The intensity of the white line at both the L<sub>2</sub> and L<sub>3</sub> edges of 12 wt% Pt-H<sub>2</sub>/NaY are observed to be lower than the bare platinum clusters dispersed in NaY. To derive mean-

### 3. Parameterization of resonance absorption at the L edges of Pt

---

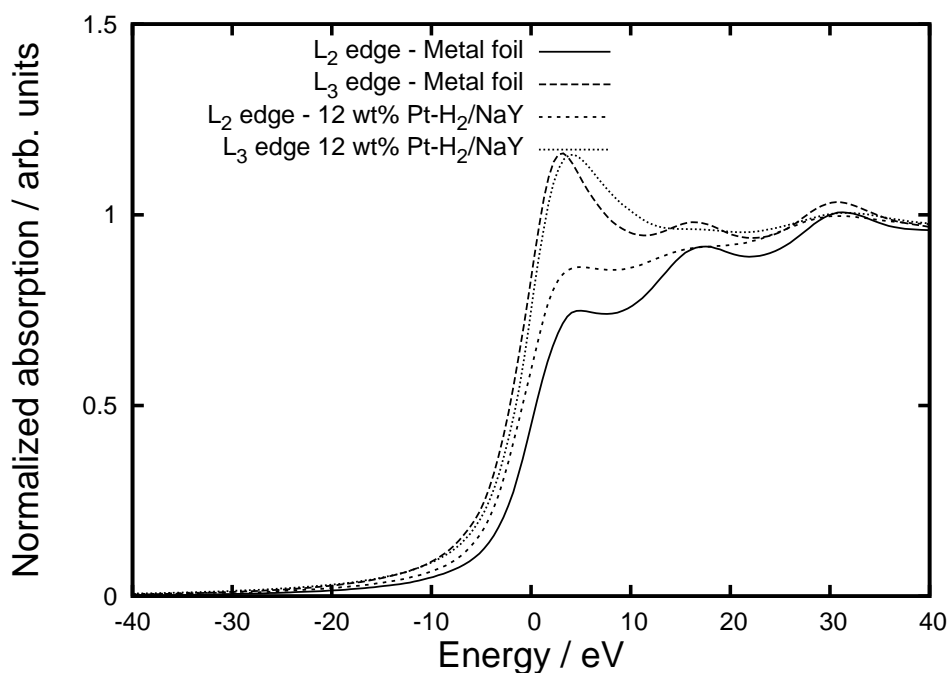


Figure 3.6.: Comparison of the L<sub>2</sub> and L<sub>3</sub> edge spectra of Pt metal foil with 12 wt% Pt-H<sub>2</sub>/NaY at 473 K

ingful information from parameterization of the XAS spectra, a consistent approach in data reduction like energy calibration, background subtraction and normalization should be carried out. Additionally for the derived information to be reproducible, the methodology used in the parameterization should be clearly defined. The following steps were carried out in sequence for the L<sub>2</sub> and L<sub>3</sub> edge data:

- The XAS spectra of the Pt metal foil measured together with each sample were aligned with each other.
- The first point of zero-crossing of the second derivative of the Pt metal spectra was assigned to the tabulated edge energy of Pt and the corresponding XAS spectra of the samples were energy calibrated.

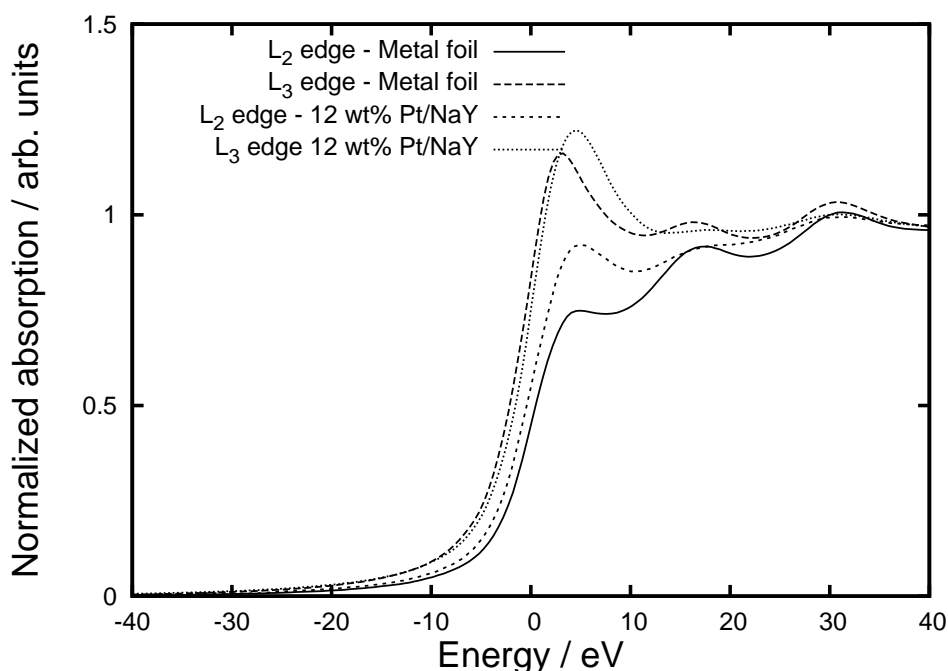


Figure 3.7.: Comparison of the  $L_2$  and  $L_3$  edge spectra of Pt metal foil with 12 wt% Pt/NaY at 473 K after purging with Ar gas flow

- After background removal from the pre-edge region, normalization<sup>7</sup> to unit edge step was carried out.
- The inflection points of the XAS spectra of the samples and the metal foil were determined from their corresponding first derivative plots.

<sup>7</sup>The normalization process involved a regression to the XANES spectrum in the pre-edge region (-130 to -30 eV before the edge energy) and the post-edge region. A linear function is regressed to the pre-edge region, and a three term quadratic function is regressed to the post-edge region. These lines were extrapolated to the absorption edge,  $E_0$ , and the difference in absorption between these projected lines at  $E_0$  was the edge step. Normalized spectra were produced by subtracting the pre-edge line from the entire data spectrum and then dividing the spectrum by the step height. After normalization, the pre-edge region lies along zero absorption and the edge step is 1. However there are two aspects to normalization of XAS data [19] namely energy dependent and energy independent. Energy dependent normalization is necessary for transmission data if comparing to theoretical calculations or data from other absorption edges whereas energy independent normalization removes the effect of sample thickness so that different samples may be directly compared.

### 3. Parameterization of resonance absorption at the L edges of Pt

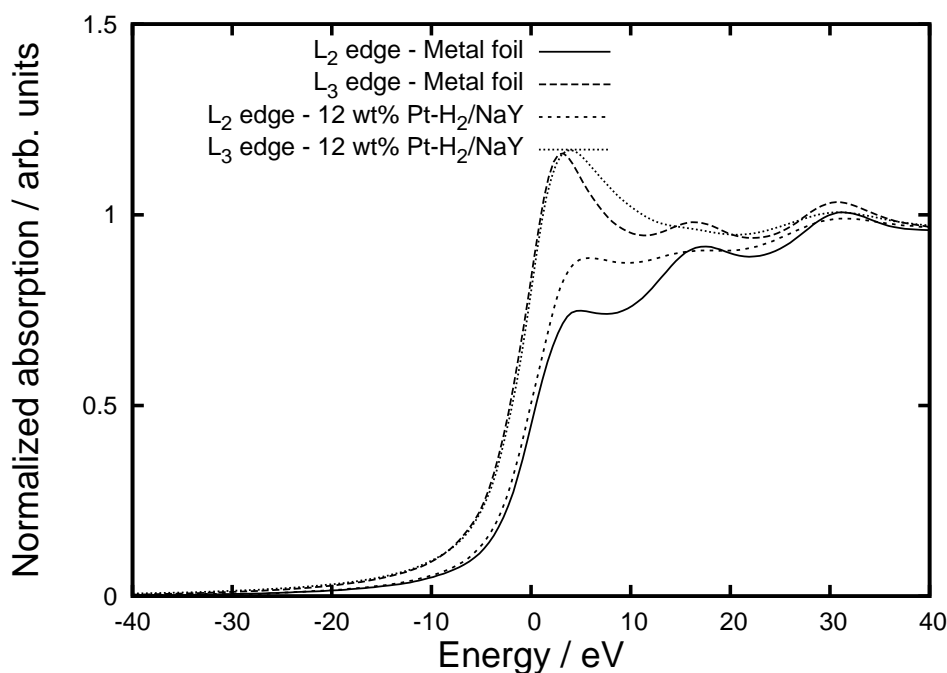


Figure 3.8.: Comparison of the L<sub>2</sub> and L<sub>3</sub> edge spectra of Pt metal foil with 12wt% Pt-H<sub>2</sub>/NaY at room temperature (rt)

- The energy scale (x-axis scale) was shifted using the expression  $(E-E_i)$ , where  $E_i$  is the first inflection point of each sample. After the shift to the energy scale, the L<sub>2</sub> and L<sub>3</sub> edge spectrum of each sample could be overlaid.
- Overlap in the EXAFS oscillations above 40 eV for the L<sub>2</sub> and L<sub>3</sub> was verified in the overlaid spectra
- The area under the curves for each of the investigated sample was determined using Simpson's rule in the range -30 eV to +30 eV.

The area under the curve determined employing the afore mentioned steps for different samples investigated in this study are given in table 3.2.

The numerator in equation 3.21 is given by:

$$(\delta A_3 + 1.11\delta A_2) \quad (3.30)$$

where  $\delta A_3$  is the difference in area under the L<sub>3</sub> edges of the sample and the Pt metal foil and  $\delta A_2$  is the difference in area under the L<sub>2</sub> edges of the sample and the Pt metal foil.



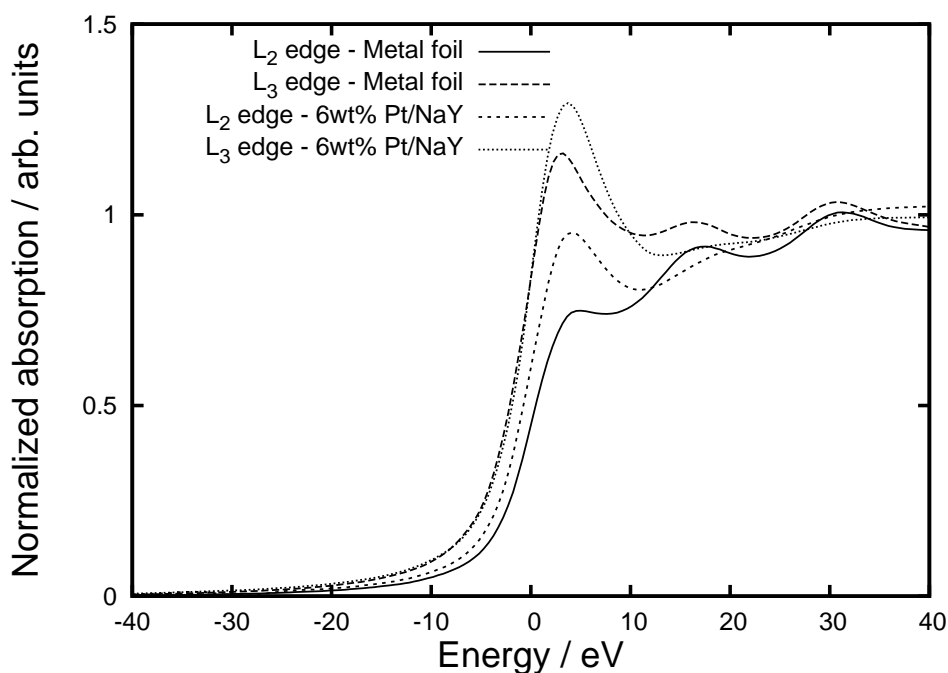


Figure 3.9.: Comparison of the  $L_2$  and  $L_3$  edge spectra of Pt metal foil with 6wt% Pt/NaY at (Bottom) rt after purging with Ar gas flow

Sample	Area / eV	
	( $L_2$ edge )	( $L_3$ edge)
12 wt% Pt-H <sub>2</sub> /NaY	29.56	33.50
12 wt% Pt/NaY	29.30	33.77
6 wt% Pt-H <sub>2</sub> /NaY	28.58	33.83
6 wt% Pt/NaY	29.66	34.21
Pt metal foil	26.86	33.59
12 wt% Pt-H <sub>2</sub> /NaY	28.71	34.00
6 wt% Pt-CO/NaY	32.02	35.11

Table 3.2.: Area under the curve determined using Simpson's rule.

The denominator in equation 3.21 can either be calculated or since it is a constant for a particular element, it can also be used directly from earlier calculations. In this study, the sum of the area under  $L_3$  and 1.11 times  $L_2$  edge area of bulk platinum metal

### 3. Parameterization of resonance absorption at the L edges of Pt

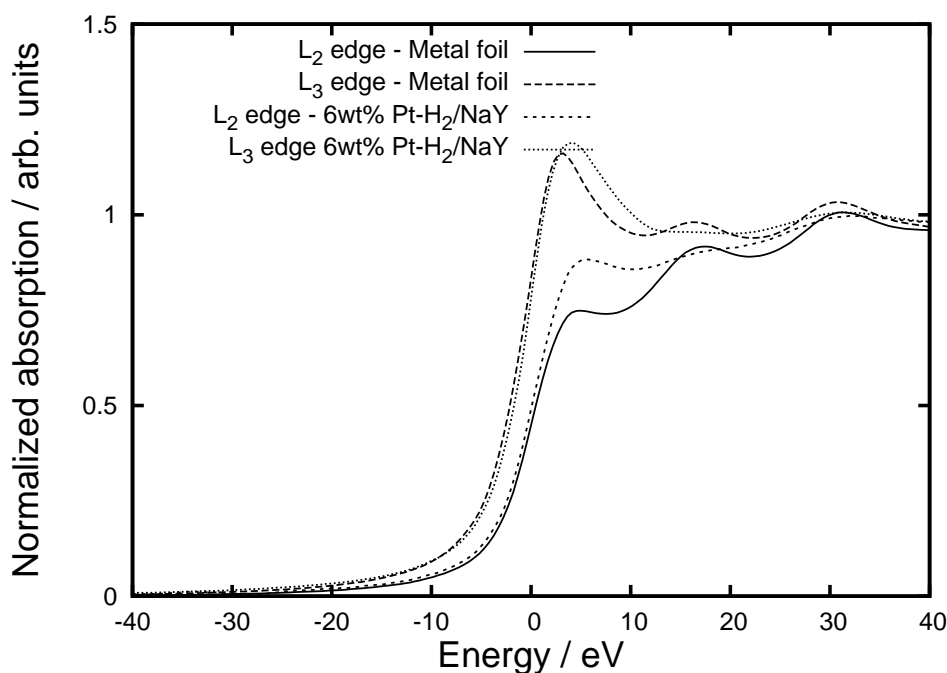


Figure 3.10.: Comparison of the L<sub>2</sub> and L<sub>3</sub> edge spectra of Pt metal foil with 6wt% Pt-H<sub>2</sub>/NaY at 473 K

Sample	$f_d$ / holes	$\Delta h_{\text{total}}$ / holes
12 wt% Pt-H <sub>2</sub> /NaY (473 K)	0.05	$1.41 \pm (0.07)^a$
12 wt% Pt/NaY (473 K)	0.05	$1.40 \pm (0.07)^a$
6 wt% Pt-H <sub>2</sub> /NaY (473 K)	0.04	$1.39 \pm (0.07)^a$
6 wt% Pt/NaY (473 K)	0.06	$1.42 \pm (0.07)^a$
12 wt% Pt-H <sub>2</sub> /NaY (rt)	0.04	$1.40 \pm (0.07)^a$
6 wt% Pt-CO/NaY (rt)	0.11	$1.50 \pm (0.07)^a$

Table 3.3.: Fractional change in d-band vacancies,  $f_d$  and the total density of unoccupied states with d-character  $\Delta h_{\text{total}}$  calculated for different samples. <sup>a</sup>-uncertainty of 5% reported by Sham, Naftel and Coulthard [3]

XANES spectrum is used. After substitution of the different terms, the values obtained for the fractional change in d-band vacancies,  $f_d$  and the total density of unoccupied states with d character  $\Delta h_{\text{total}}$  are given in table 3.3

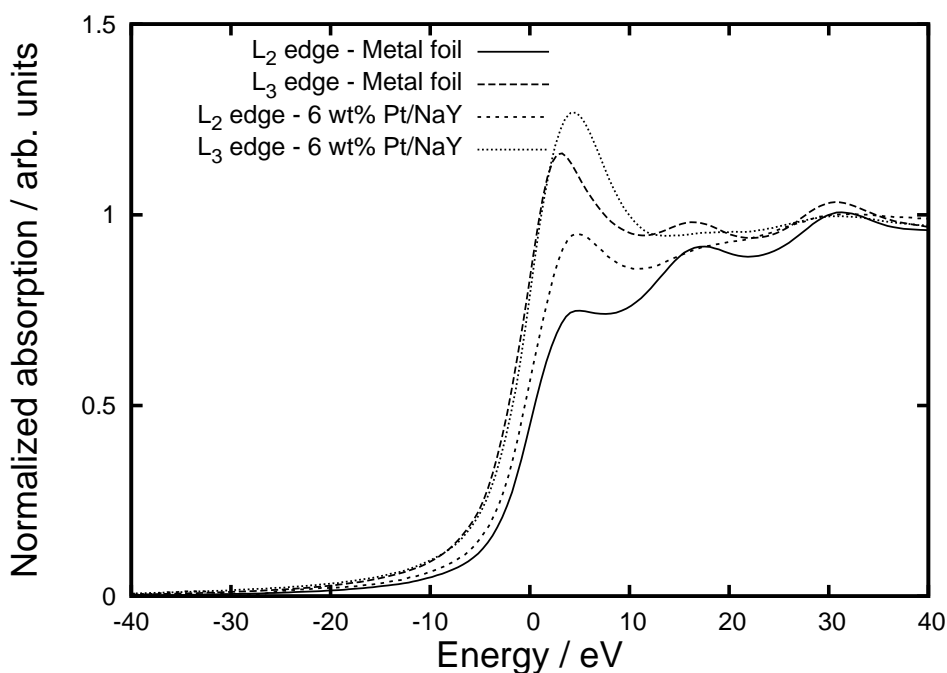


Figure 3.11.: Comparison of the  $L_2$  and  $L_3$  edge spectra of Pt metal foil with 6wt% Pt/NaY at 473 K (Bottom) after purging with Ar gas flow

### 3.2.2. QXAS during CO interaction with 6 wt%Pt/NaY

The Q-XAS spectra of 6 wt% Pt/NaY during CO interaction was recorded in transmission mode with a continuously moving monochromator, energy calibrated with the Pt metal foil, pre-edge background subtracted and unit step normalized. Qualitatively, upon CO interaction with 6 wt% Pt/NaY at 1 bar, the white line at the Pt  $L_3$  edge was found to change in intensity and position of the maximum in the peak as discussed in chapter 2 under section 2.3.1. Q-XAS Pt  $L_3$  edge (11564 eV) spectra during CO interaction with 6 wt% Pt/NaY at room temperature is presented in figure 3.13.

In the in situ Q-XAS measurements shown in figure 3.13, time dependent change of the white line is observed and in order to quantify the changes, the area under the curves were determined using numerical integration method of Simpson's rule. The profile was also subjected to curve fitting analysis and fitted as a superposition of a arctan function and pseudo-Voigt function. The trends in the two different approaches were similar but an interesting observation was made where the area under the curve

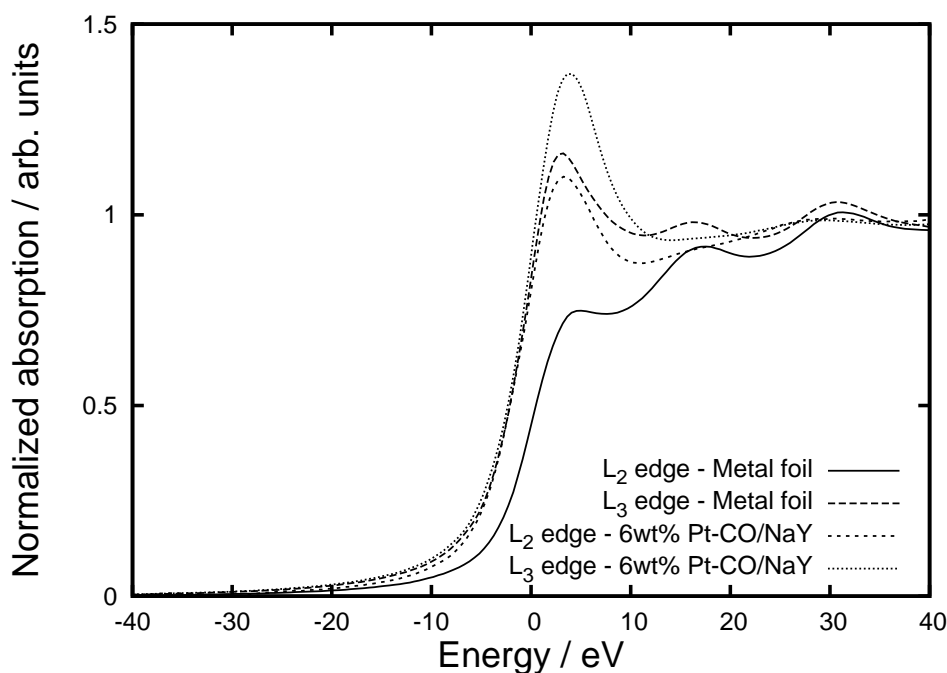


Figure 3.12.: Comparison of the L<sub>2</sub> and L<sub>3</sub> edge spectra of Pt metal foil with 6wt% Pt-CO/NaY at room temperature following reduction under hydrogen flow, argon flow to remove adsorbed hydrogen and subsequent CO flow

remained almost constant with time when a large energy range [11540 to 11580 eV] was chosen for the area determination. The area determined in the range [11568 to 11580 eV] and [11540 to 11580 eV] are given in table 3.4 and plotted against time in figure 3.14 while the same in the range [11540 to 11580 eV] is plotted against time in figure 3.15.

From the Q-XAS measurements during CO interaction, the intensity of the white line increases with time along with a small shift in the edge position towards higher energy. When a larger energy range is chosen to determine the change in the area under the curve with time, the increase in area due to increase in intensity of white line is accompanied with a decrease in area due to edge position shift. This tendency is a direct result of the constant energy range used for area determination. As a result, the plot of area under the curve determined in the range [11540 to 11580 eV] against time, shown in figure 3.15, gives a trend line parallel to x-axis.

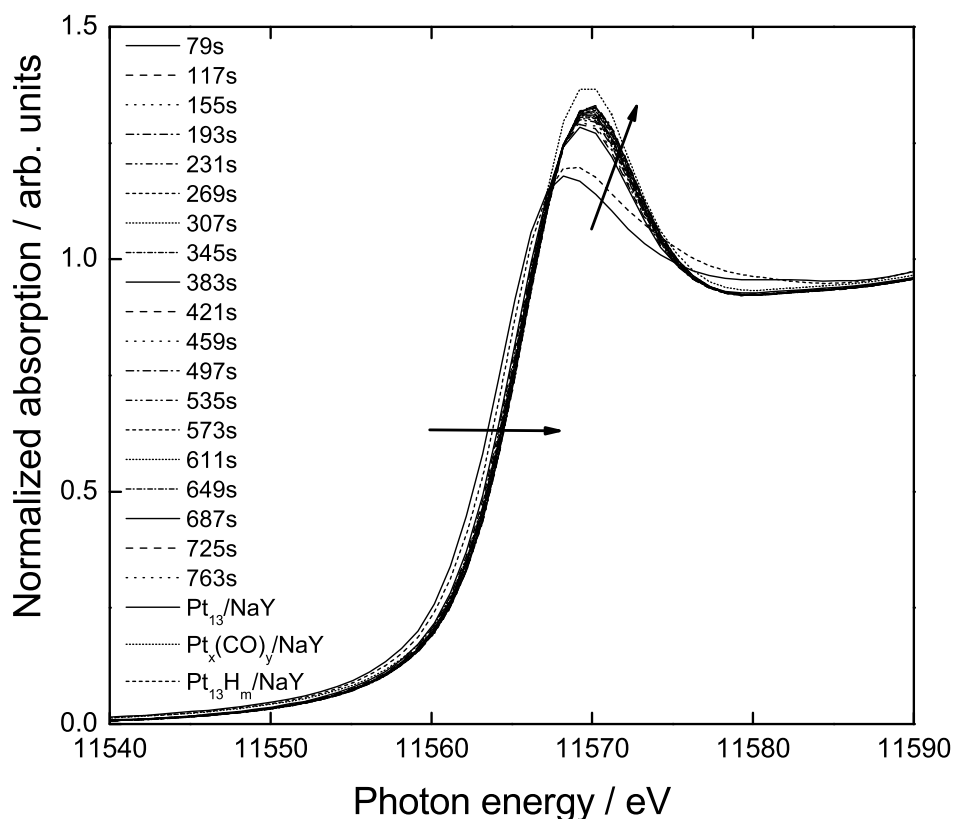


Figure 3.13.: Q-XAS Pt L<sub>3</sub> edge (11564 eV) spectra during CO interaction with platinum cluster at room temperature

However, when the area of integration is chosen to be from the isosbestic point (refer figure 3.13) in the rising edge at 11568 eV up to 11580 eV where the different curves merge into one, an almost linear increase in area under the curve with time is clearly observed as shown in figure 3.14. Therefore, compared to the qualitative picture of increase in white line intensity with time the quantitative picture shows a mixture of two effects, namely the shift in edge energy and the simultaneous increase in white line intensity. As discussed in the section 3.1.5 about deconvolution of XANES region by arctan function and a pseudo-Voigt function, the observations mentioned above point towards a scenario with variable center for the arctan functions, pseudo-Voigt peak height and a constant pseudo-Voigt peak position. To verify this hypothesis, curve fitting of the Q-XAS spectra with a arctan function, first with a fixed x-coordinate of the center of arctan and second with a flexible x-coordinate of the center of arctan, pseudo-Voigt function with variable width and height was performed. In total, nineteen Q-XAS spectra and

### 3. Parameterization of resonance absorption at the L edges of Pt

---

Time / s	Area / eV	
	11568 to 11580 eV	11540 to 11580 eV
79	12.95	19.32
117	12.98	19.26
155	13.00	19.23
193	13.05	19.23
231	13.06	19.21
269	13.08	19.21
307	13.10	19.21
345	13.11	19.20
383	13.13	19.21
421	13.15	19.19
459	13.15	19.18
497	13.16	19.17
535	13.18	19.16
573	13.19	19.15
611	13.21	19.18
649	13.22	19.14
687	13.24	19.15
725	13.24	19.13
763	13.25	19.14

Table 3.4.: The numerically integrated area under the curve during CO interaction measured in Q-XAS mode using two different integration (energy) ranges

one XAS spectrum of the equilibrium 6 wt% Pt-CO/NaY were subjected to curve fitting analysis and the change in centers of the arctan function and the area under the peak of pseudo-Voigt function were determined as a function of time.

By coding a routine in GNU plot to perform the curve fitting analysis using the user-defined functions and convergence criteria, the fit parameters were obtained. Care was taken during curve fitting procedure that all the different spectra are fit in a consistent manner. The parameters iterated in the fitting procedure were the x-coordinate center

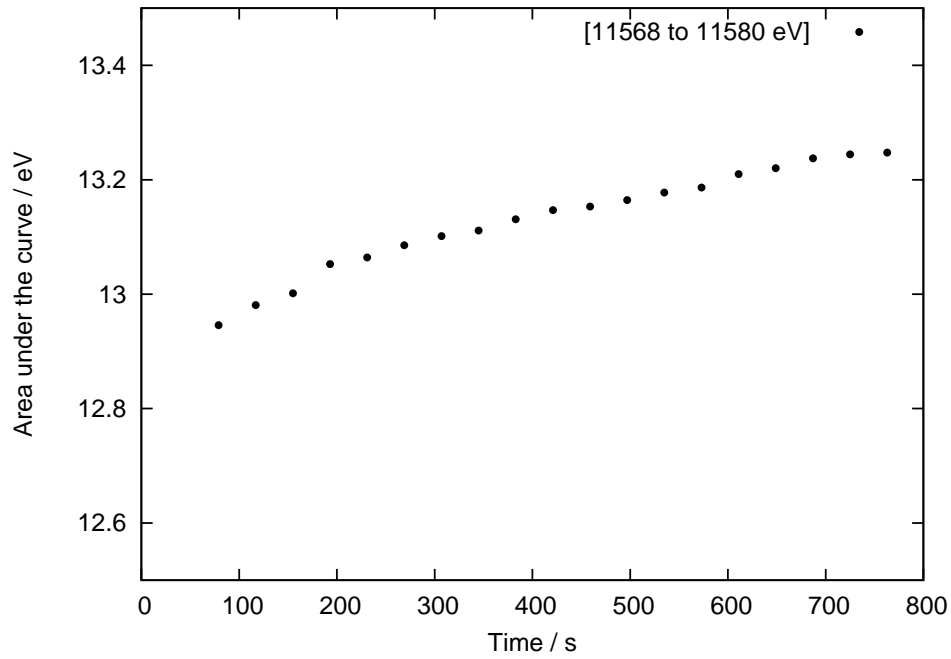


Figure 3.14.: Area under the curve determined in the range [11568 to 11580 eV]

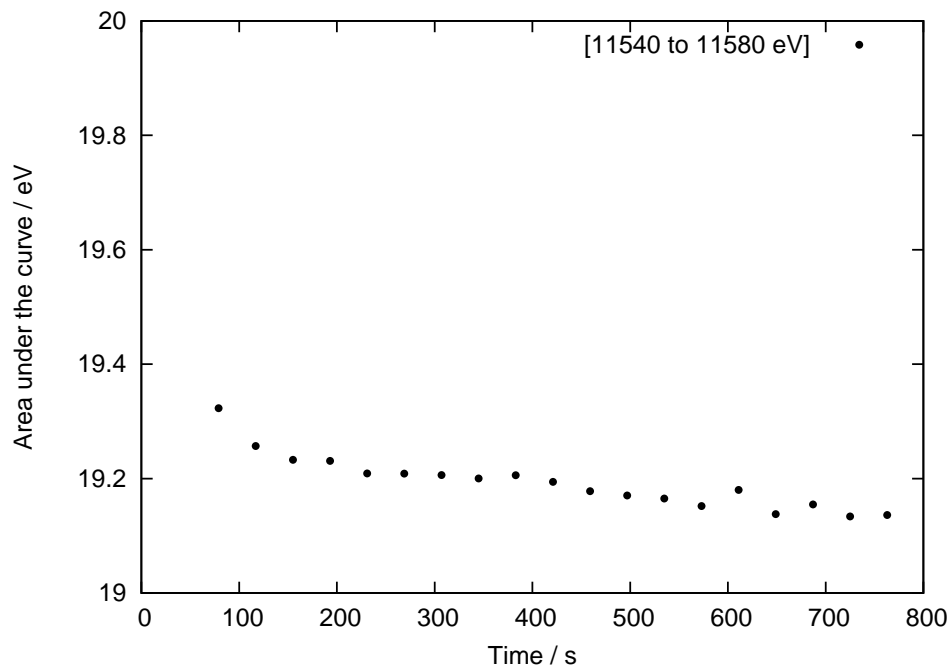


Figure 3.15.: Area under the curve determined in the range [11540 to 11580 eV]

### 3. Parameterization of resonance absorption at the L edges of Pt

Time / s	Center of arctan / eV	Area under the pseudo-Voigt Function / eV
79	11575.7	12.84
117	11575.6	12.72
155	11575.5	12.65
193	11575.4	12.57
231	11575.3	12.52
269	11575.3	12.51
307	11575.3	12.47
345	11575.2	12.44
383	11575.2	12.41
421	11575.1	12.36
459	11575.1	12.33
497	11575.1	12.30
535	11575.0	12.26
573	11575.0	12.23
611	11575.0	12.22
649	11574.9	12.13
687	11574.9	12.12
725	11574.8	12.08
Pt-CO/NaY	11575.7	13.44

Table 3.5.: The centers of the fitted arctan function and the area estimated by numerical integration under the fitted pseudo-Voigt function during CO interaction with Pt/NaY material.

of arctan and width of the arctan function (called  $x_0$  and  $w_a$ ), full width at half maximum (FWHM) of the pseudo-Voigt function (called  $w_v$ ), the height of the peak (called  $h$ ) and fraction of contribution from Lorentzian and Gaussian distribution to the pseudo-Voigt function (called  $m$ ). (For the details about the curve fitting routing, refer Appendix)

The experimental Q-XAS spectra and the fit to the spectra along with the fit to the XANES spectra of 6 wt% Pt-CO/NaY are given in the appendix section A.3 in figures A.5 to A.9.



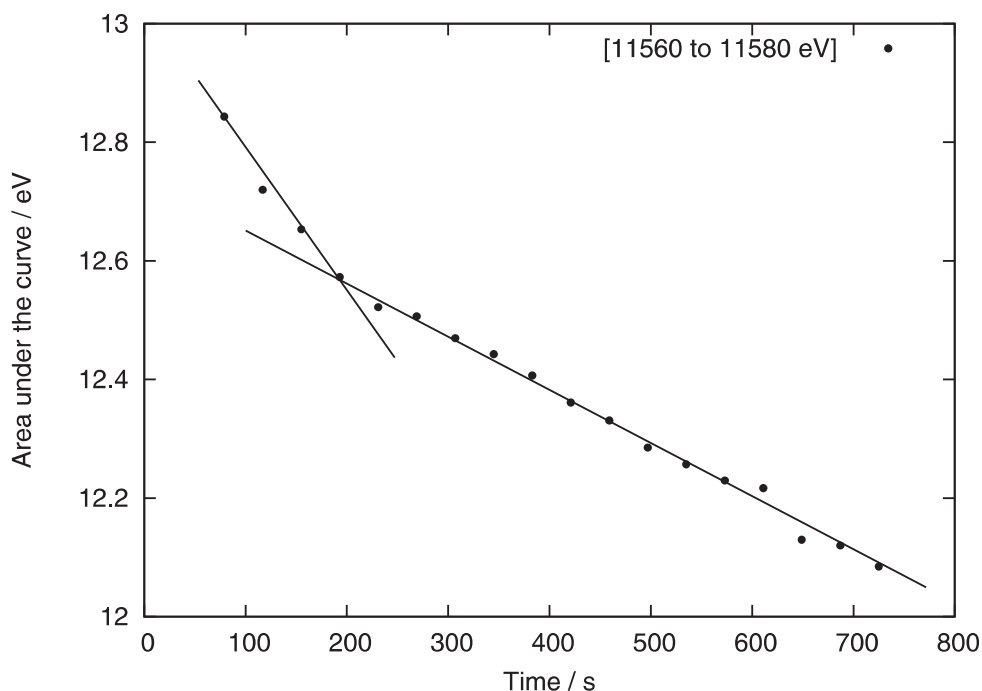


Figure 3.16.: Area under the curve (pseudo-Voigt function) estimated in the range [11560 to 11580 eV] as a function of time and the linear fit to the data in two regions indicating the kinetic behavior

The reliability of the absolute parameters obtained from curve fitting procedure is not good, however when a consistent approach is used, the tendencies in the change of certain parameters over a series of spectra could provide some useful information. One such example is the center of the arctan function which represents the threshold edge energy and the area under the pseudo-Voigt function determined at different times. The area under the pseudo-Voigt function in the range [11560 to 11580 eV] were estimated using numerical integration and are presented in table 3.5 along with the center of arctan function.

Numerical integration was carried out by employing the QAG algorithm (Gauss-Kronrod 61 point rule) from the GNU scientific library where the integration region is divided into subintervals, and after each iteration the subinterval with largest error is bisected. In general, this algorithm applies an integration rule adaptively until an estimate of the integral over a range is achieved within a desired error limit.

From table 3.5 it can be noted that the center of the arctan determined from the fit remains constant within the error limit. The area under the pseudo-Voigt function

### 3. Parameterization of resonance absorption at the L edges of Pt

---

shows a gradual change with time in two regimes as shown in figure 3.16. Until 193 s, a linear fit to the data with slope of  $13.00 \pm 0.03 \text{ eV s}^{-1}$  and from 193 s up to 725 s, a linear fit with slope of  $12.74 \pm 0.01 \text{ eV s}^{-1}$  are obtained. The reaction is observed to be of zero order which is generally observed when the surface of the catalyst is saturated by the reactants. The rate expression for a zero-order reaction in simple terms is given by:

$$\frac{-dc}{dt} = k \quad (3.31)$$

where  $c$  denotes concentration and  $k$  denotes the reaction rate coefficient (or rate constant). Upon integrating this differential equation the integrated zero-order rate expression:

$$|c - c_0| = -kt \quad (3.32)$$

where  $c$  represents the concentration of the chemical of interest at a particular time, and  $c_0$  represents the initial concentration.

In the present case, the reaction is of zero order and when the intensity of white line is plotted versus time the result is a straight line. The slope of the resulting line gives the zero order reaction rate coefficient  $k$ . These observations are different from those observed when the total area under the curve was determined by direct numerical integration of the curve with a larger energy range. Notable increase in the area and shift in the center of arctan function are also observed for the final product of the CO interaction, which from previous results of EXAFS analysis corresponds to a Pt-CO species stabilized in the zeolite material. Therefore from the evaluation of Q-XAS data, kinetic information with an estimate of the extent of changes that take place with time has been obtained quantitatively.

# 4. Multi-resolution wavelet analysis of EXAFS spectra

## 4.1. Introduction

Multi-resolution wavelet based analysis of EXAFS spectra of model system was performed to demonstrate the capabilities and limitations of wavelet transform (WT) to complement the conventional Fourier transform (FT) EXAFS analysis.

FT is the primary step in the interpretation of EXAFS spectra and the selection of a theoretical fitting model to the experimental data [45]. Modulus of FT provides information about the number of coordination shells and their distance from the absorbing atoms. However, it is difficult to separate the scattering contributions of nearest neighbor atoms with similar distances using FT analysis. Using the example of Zn-Al layered double hydroxides, Funke, Scheinost and Chukalina [46] demonstrated that it is possible to separate the scattering contributions of nearest neighbor atoms at similar distances but with different atomic numbers using Morlet wavelet transform.

Wavelet transform using continuous Cauchy wavelet was used by Muñoz, Argoul and Farges [47] to visualize EXAFS spectra in three dimensions: the wave vector  $k$ , the interatomic distance uncorrected for phase shifts  $r$  and the continuous Cauchy wavelet transform (CCWT) modulus. Shao and Zhao [48] used WT to extract EXAFS signal from a measured x-ray absorption spectrum. A more sophisticated wavelet based analysis of EXAFS data has been published by Yamaguchi et al. [49] where Daubechies wavelet was utilized in the formulation of a linear inverse problem algorithm to solve the EXAFS equation based on Galerkin-method.

Wavelet analysis of x-ray diffraction pattern for glass structures [50], in particular to understand the real and reciprocal space structural correlations contributing to the

first sharp diffraction peak in silica glass [51], extraction of instantaneous frequency and amplitude of rapidly varying, superimposed amplitude-modulated and frequency-modulated signal components [52] are some examples where wavelet analysis has been used.

For XAS analysis Funke, Scheinost and Chukalina [46] suggested to complement FT by WT, which not only provides radial distance resolution but simultaneous  $k$  resolution. This complementary information is useful for the discrimination of shells by the type of element that contributes to a shell, especially if more than one type of atom from a same distance contribute to the FT peak. Since WT by design provides good localization in both time and frequency, for an EXAFS signal which is a function of photoelectron wave vector  $k$ , WT provides good localization in radial distance  $r$  and  $k$ . However, application of WT routinely to EXAFS data analysis requires proper description of the boundary conditions and other limitations.

Wavelet investigation of Co K-edge EXAFS data of  $\text{La}_{0.5}\text{Ca}_{0.5}\text{CoO}_{3-\delta}$  by Morlet wavelet with aims similar to that of the present study but using theoretical EXAFS signal generated using FEFF code was published in 2007 [53]. The authors argued that Morlet wavelet was not suitable to differentiate between Co–La and Co–Ca scattering contributions to a single FT peak because of dissimilarity of the chosen wavelet to the real EXAFS signal. Therefore, modifying the Morlet wavelet to another wavelet that resembles the EXAFS signal was further suggested.

In the present work however, the limitations of Morlet wavelet are arrived at in more detail and additionally recommendations suggested in the afore mentioned publication are elaborated with specific examples. The conclusions that are arrived in this study with regard to limitations of WT are general in nature to any wavelet study and therefore can be applied to a broad class of problems even outside the XAS field. Some general information about wavelets and wavelet analysis are presented along with basic formulations of WT in the following sections.

## 4.2. Formulation

Wavelets are functions that satisfy certain mathematical requirements and are used in representing data or other functions. Approximation of certain functions using superpo-

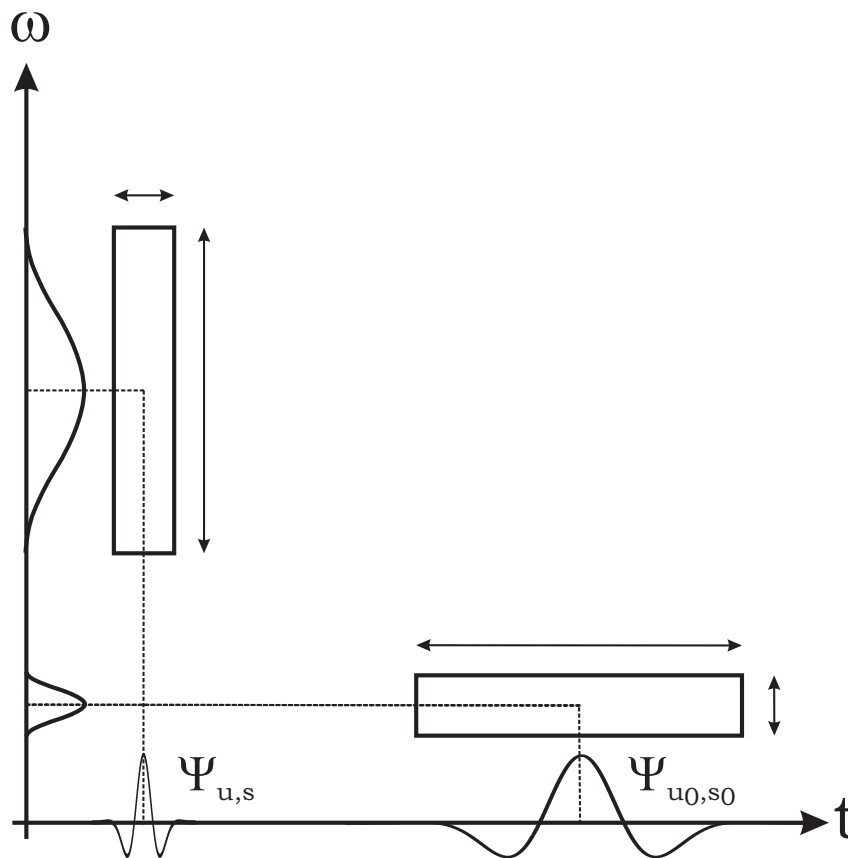


Figure 4.1.: Time-frequency boxes of two wavelets  $\psi_{u,s}$  and  $\psi_{u_0,s_0}$ . When the scale  $s$  decreases, the time spread is reduced but the frequency spread increases and covers an interval that is shifted towards higher frequencies

sition of other functions has been known for a long time since Joseph Fourier discovered that he could superpose sines and cosines to represent other mathematical functions. Like a windowed FT, a WT can measure the time frequency variations of spectral components, but with a different time-frequency resolution. In wavelet analysis the scale that is used to look at data plays a special role and wavelet transform algorithms process data at different scales or resolutions.

The analysis procedure using wavelets is to adopt a wavelet prototype function, called an analyzing wavelet or mother wavelet. Temporal analysis is performed with a contracted, high frequency version of the prototype wavelet, while frequency analysis is performed with a dilated, low frequency version of the same wavelet. Because the original signal or function which is analyzed can be represented in terms of a wavelet

expansion (using coefficients in a linear combination of the wavelet functions), data operations can be performed using just the corresponding wavelet coefficients.

One of the mathematical requirements that a wavelet satisfies is that a wavelet  $\psi$  is a function of zero average [54]:

$$\int_{-\infty}^{+\infty} \psi(t) dt = 0, \quad (4.1)$$

which is dilated with a scale parameter  $s$ , and translated by  $u$ :

$$\psi_{u,s}(t) = \frac{1}{\sqrt{s}} \psi\left(\frac{t-u}{s}\right) \quad (4.2)$$

The wavelet transform of a function  $f(t)$  at the scale  $s$  and position  $u$  is computed by correlating  $f$  with a wavelet  $\psi_{u,s}$

$$Wf(u,s) = \int_{-\infty}^{+\infty} f(t) \frac{1}{\sqrt{s}} \psi^*\left(\frac{t-u}{s}\right) dt \quad (4.3)$$

In the time-frequency plane, a wavelet  $\psi_{u,s}$  is symbolically represented by a rectangle centered at  $(u, \frac{\eta}{s})$ . The time and frequency spread is proportional to  $s$  and  $\frac{1}{s}$  respectively. When  $s$  varies, the height and width of the rectangle change but its area remains constant, as illustrated in figure 4.1.

Goupliaud, Grossmann and Morlet invented a modulated Gaussian wavelet, known as Morlet wavelet [55]. Using time-frequency terminology for simplicity and considering the signal to be an input function of time  $f(t)$ , the Morlet wavelet has been expressed in equation 4.4 as

$$\psi(t) = \frac{1}{\sigma\sqrt{2\pi}} \left[ \exp i\kappa t - \exp\left(-\frac{\kappa^2}{2}\right) \right] \exp\left(-\frac{t^2}{2\sigma^2}\right) \quad (4.4)$$

Here  $\kappa$  specifies the number of oscillations under the Gaussian envelope in the case when  $\sigma=1$ . The criterion for choosing a wavelet for a particular type of signal processing depends on the fact that the components appearing in the signal have a close resemblance to the form of the chosen wavelet. The plots of the Morlet wavelet for  $\kappa = 14$ ;  $\sigma = 2$  and  $\kappa = 2$ ;  $\sigma = 1$  are given in figure 4.2.

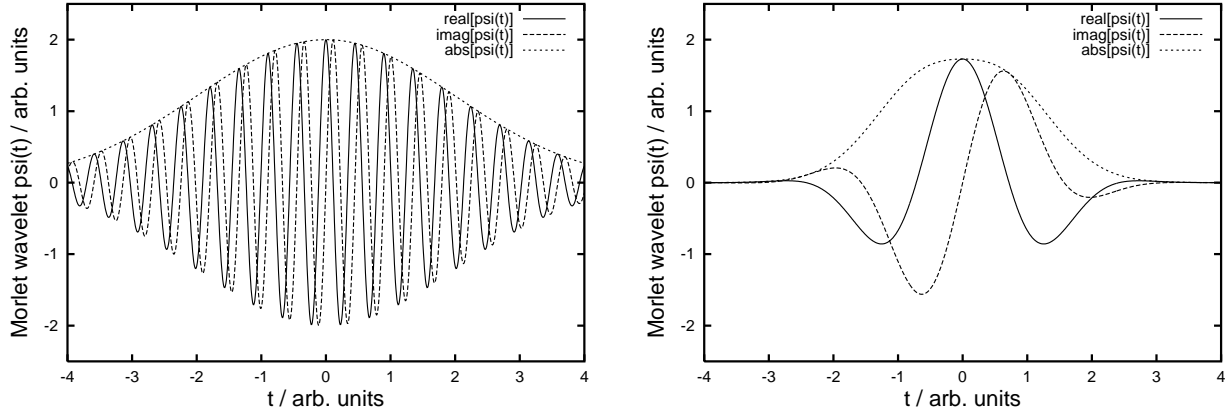


Figure 4.2.: Morlet wavelet as a function of variable  $t$  with  $\kappa = 14$ ;  $\sigma = 2$  (Left) and  $\kappa = 2$ ;  $\sigma = 1$  (Right)

The model signal used in the illustration of WT is based on equation 4.5 [46].

$$f(t) = \frac{A_1}{\sigma\sqrt{2\pi}} \sin(2r_1t + \delta_1) \exp\left(-\frac{(t-C_1)^2}{2\sigma^2}\right) + \frac{A_2}{\sigma\sqrt{2\pi}} \sin(2r_2t + \delta_2) \exp\left(-\frac{(t-C_2)^2}{2\sigma^2}\right) \quad (4.5)$$

Equation 4.5 was used to generate the signals in figure 4.8 which were then subjected to FT. It is helpful to introduce the parameter  $\Delta C$  given simply by  $\|C_2 - C_1\|$  in order to discuss the effect of superposition of two input signals on the WT which will be discussed in a later section. Modified and recompiled FORTRAN code of program HAMA [46] together with Origin lab and MATLAB software were used to calculate and visualize the wavelet transformation.

## 4.3. Results and discussion

### 4.3.1. Wavelet analysis of model EXAFS spectra

Model EXAFS signals were generated using EXCURV98 [2] package in order to subject them to rigorous analysis using wavelet transform. The aim of the analysis is to decipher

#### 4. Multi-resolution wavelet analysis of EXAFS spectra

the influence of  $k$ -weighting on the input signal on the information retrievable from wavelet transform. The model EXAFS signal with silver absorber and two neighboring shells one with silver and the other with gold were generated using the parameters given in table 4.1.

Model	Abs-Bs <sup>a</sup>	CN(Bs) <sup>b</sup>	R(Bs) <sup>c</sup> Å	$\sigma$ <sup>d</sup> Å	E <sub>F</sub> <sup>e</sup> eV	$k$ -range Å <sup>-1</sup>
1	Ag-Ag	6.0	2.88	0.071	0.0	3.00–18.00
	Ag-Au	6.0	2.88	0.071	0.0	3.00–18.00
2	Ag-Ag	12.0	2.88	0.071	0.0	3.00–18.00

Table 4.1.: Parameters used in the generation of the model EXAFS signal.

<sup>a</sup>Absorber(Abs)–backscatterer(Bs). <sup>b</sup>Average coordination number(CN).

<sup>c</sup>Interatomic distance. <sup>d</sup>EXAFS Debye-Waller factor( $\sigma$ )

The EXAFS signal so generated was subjected to wavelet transformation in order to check if it is possible to distinguish between Ag–Au and Ag–Ag backscatterers located at equal distances. It is reported by Funke, Scheinost and Chukalina [46] that particular  $k$ -weighting used for the input EXAFS signal has a marked effect on the wavelet transform and that care should be taken that higher weighting like  $k^2$  or  $k^3$  does not lead to misinterpretation. Therefore the EXAFS signal was subjected to four different sample weighting schemes namely  $k^0$ ,  $k^1$ ,  $k^2$  and  $k^3$  weighting.

In order to visualize the effect of  $k$ -weighting on model EXAFS signal, the magnitude of the backscattering amplitude of Ag and Au backscatterers generated using EXCURV98 [2] is plotted against  $k$  with different weightings in figure 4.3. From the first look at these plots it is difficult to tell which weighting scheme would be more suitable to differentiate between the two backscatterers but on closer look, lower weighting like  $k^1$  or  $k^2$  have non-overlapping centers around 4 and 8 Å<sup>-1</sup> for Au and 5 and 8 Å<sup>-1</sup> for Ag.

As a consequence, in practice the differentiation between Ag and Au should be feasible with the normal curve fitting procedure employing the envelope of backscattering amplitude with the EXAFS analysis. When the difference in the goodness of fit parameter while using the two options available is not very large, it is difficult to predict either Au or Ag or a mixture of both is present at a particular distance. In short, there exists



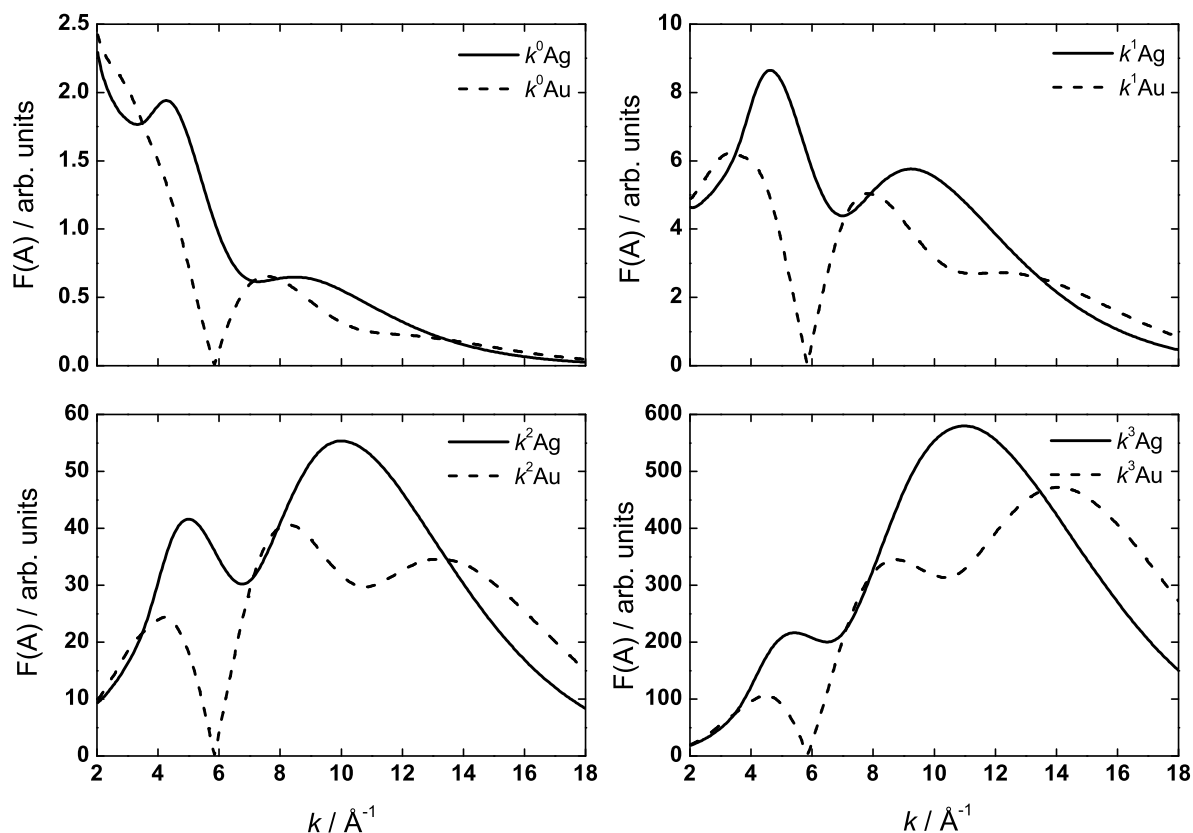


Figure 4.3.: Magnitude of backscattering amplitude of Ag and Au with different  $k$  weightings generated using EXCURV98 [2] package

a problem in distinguishing the type of backscatterer if they are at the same distance from the absorbing atom. For samples whose type of near neighbor has to be determined from a fit, magnitude of Fourier transform without either the real or imaginary parts of the transform does not provide any valuable hint. Even though some distinction is possible as seen for an ideal model signal in figure 4.4, wavelet transform might provide a better visualization than FT due to its inherent resolution in both  $k$  and  $r$  domain simultaneously. This in turn could be useful to choose an appropriate EXAFS fitting model.

To verify this hypothesis, the model signal was subjected to wavelet transformation using Morlet mother wavelets in overview (type 1) and resolved transform mode (type 2) (refer table 4.2). The  $k$ -range and  $r$ -range of the EXAFS signal chosen for the transform were 3–18  $\text{\AA}^{-1}$  and 1–4  $\text{\AA}$  respectively. Appropriate values for the wavelet param-

#### 4. Multi-resolution wavelet analysis of EXAFS spectra

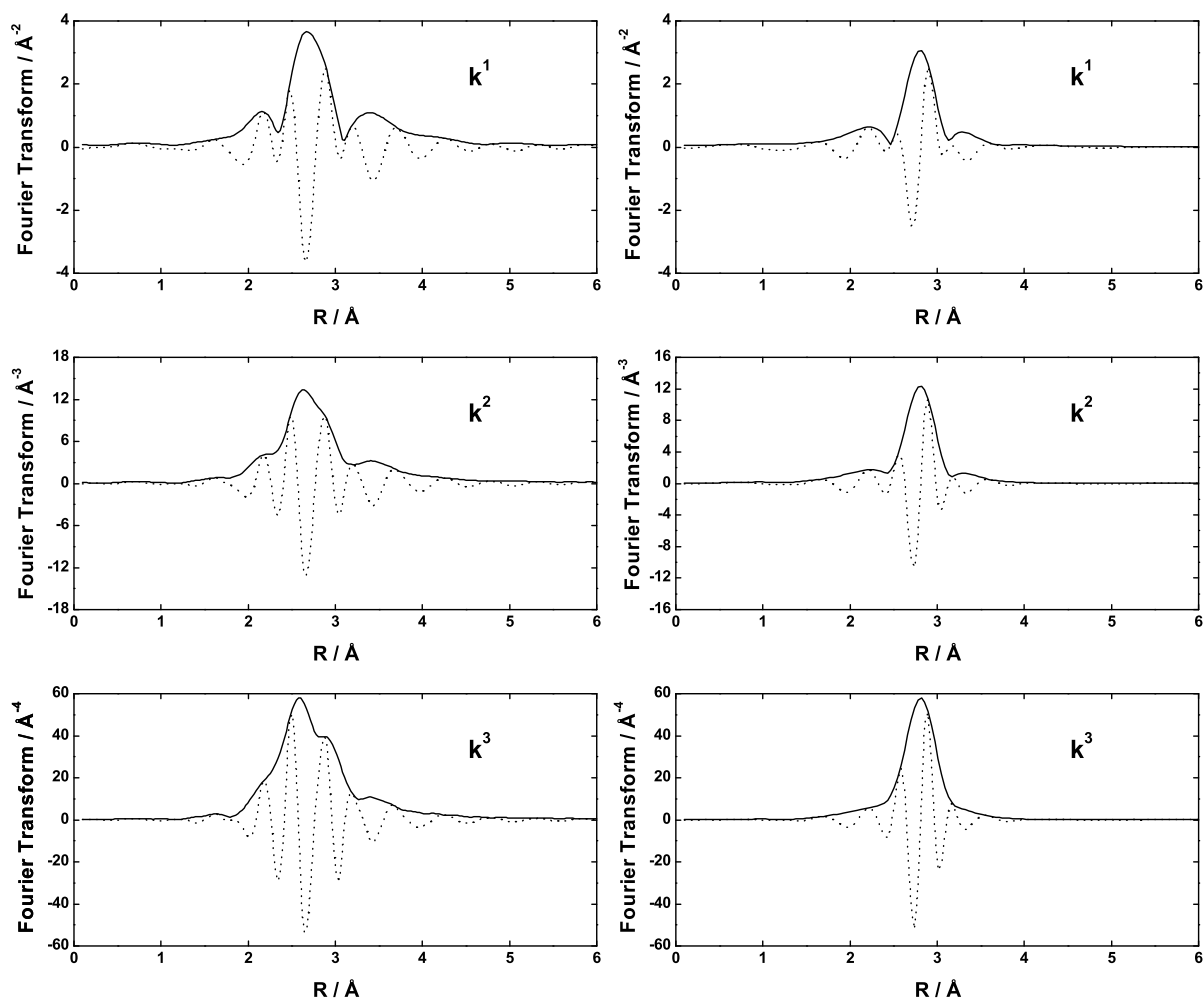


Figure 4.4.: Fourier transform (Solid line) of model EXAFS signals 1 (left) and 2 (right) along with the sine transform (dashed line) with  $k$ -weighting of 1, 2 and 3 (top–bottom)

eters must be chosen before subjecting a signal to wavelet transform depending upon the  $r$ -range of interest, in the present case around 2.88 Å. The choice of  $\kappa$  Morlet and  $\sigma$  Morlet for the overview transform were 14 and 2 respectively and for the resolved transform the values were 2 and 1. For a quick grasp of the difference between the two types of wavelet functions, the real and imaginary parts of the Morlet wavelet function are presented in figure 4.2.

Evidently, wavelet of type 1 is more suitable to extract  $k$ -space contribution over a larger  $r$ -range while type 2 is suitable to extract the same information but over a

Morlet wavelet type	$\kappa$	$\sigma$
Type 1 (Overview transform)	14	2
Type 2 (Resolved transform)	2	1
Type 3	3	1
Type 4	4	1
Type 5	5	1

Table 4.2.: Wavelet parameters used in the present study to vary the resolution of the wavelet transform

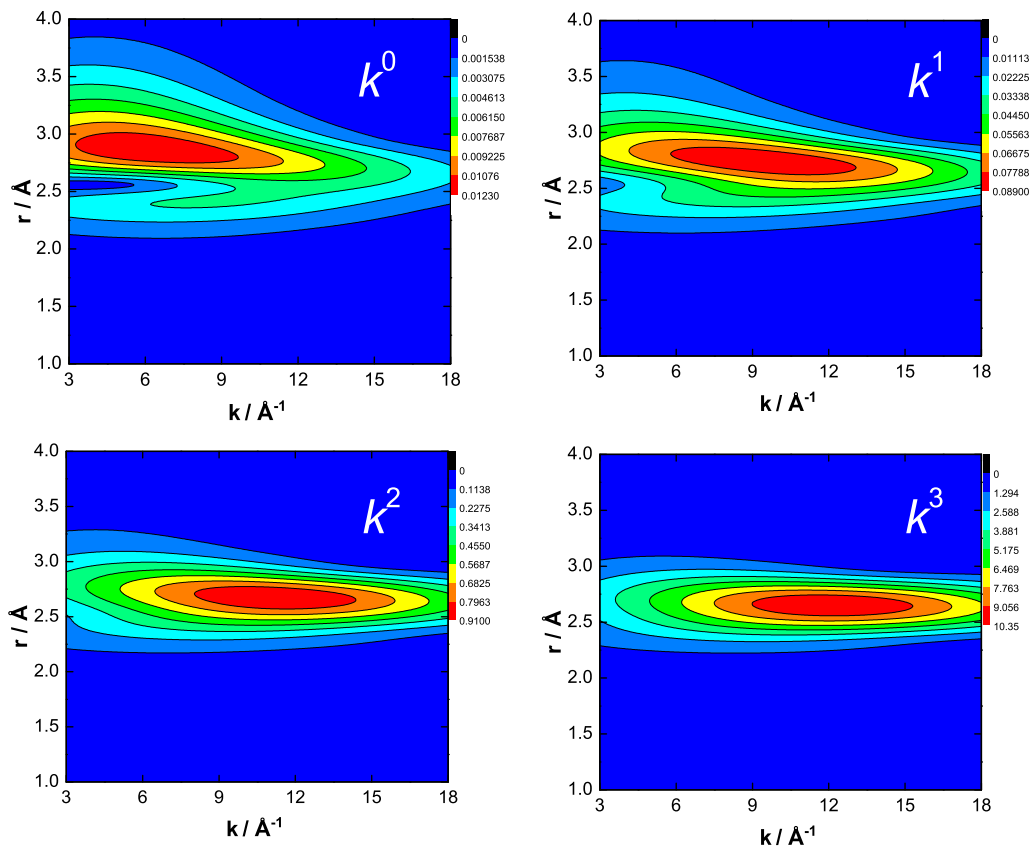


Figure 4.5.: Contour plots of the overview wavelet transform of EXAFS signal 1 with  $k$ -weighting of 0, 1, 2 and 3

#### 4. Multi-resolution wavelet analysis of EXAFS spectra

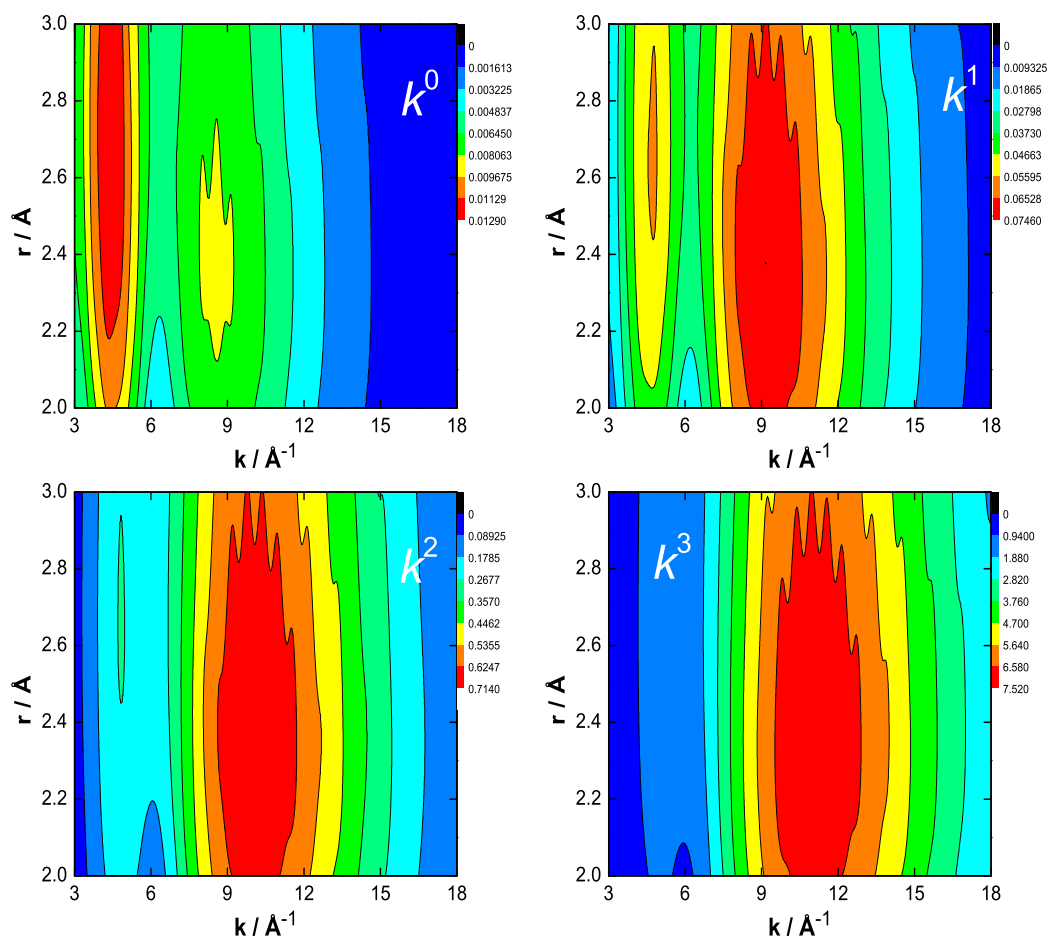


Figure 4.6.: Contour plots of the resolved wavelet transform of EXAFS signal 1 with  $k$ -weighting of 0, 1, 2 and 3

shorter  $r$ -range of interest. This unique possibility to change the resolution or multiple-resolution is possible with Morlet wavelets and the limiting factor towards the resolution comes from the Heisenberg boxes [46]. This is evidenced from the resulting transforms using type 1 and type 2 wavelets as seen in figures 4.5 and 4.6 where it can be seen that higher the  $r$ -space resolution poorer the  $k$ -space resolution and *vice versa*. Further note of caution in using WT and limitations in resolution obtainable are discussed in section 4.3.2.

The results obtained from analyzing the model signal exposed a few limitations of the use of the particular mother wavelet called Morlet wavelet for providing good  $k$ - $r$

resolution. WT using type 1 and type 2 Morlet wavelets of signal 2 for the four different weighting schemes are given in figures 4.5 and 4.6 respectively.

From the contour plots<sup>1</sup> of the wavelet transform magnitude obtained, it can be broadly observed that it is possible to adjust  $r$ -space resolution for better  $k$ -space resolution as evidenced by the wavelet centers spread in  $k$  in figure 4.5 but resolved in  $r$  and vice versa.

Another important observation is that  $k$ -weighting has a marked influence on the resulting wavelet centers so obtained. At this stage it is also evident that only for lower  $k$ -weighting, the centers in the wavelet transform match with the profile of backscattering amplitude of either Ag–Ag or Ag–Au backscatterers given in figure 4.3. Effect of  $k$ -weighting on the wavelet transform patterns with overview wavelet is minimal whereas it is pronounced when a wavelet with low frequency oscillations is used. In figure 4.6 a minimal  $k$ -weighting of  $k^1$  is found to be appropriate to see two distinctive centers in the wavelet transform which points towards two different backscatters. That the centers in WT match with the maxima of the envelope of backscattering amplitude gives additional proof that input information is less distorted by the wavelet transform. This property might be useful in cases where the wavelet transformed signal needs to be back transformed to recover the original signal.

$k$ -weighting	Wavelet center with maximum magnitude			
	Type 1		Type 2	
	$k / \text{\AA}^{-1}$	$r / \text{\AA}$	$k / \text{\AA}^{-1}$	$r / \text{\AA}$
0	6.4	2.8	4.3	8.5
1	9.4	2.7	4.6	9.2
2	11.2	2.7	4.9	10.3
3	12.1	2.6	-	10.9

Table 4.3.: The centers in the wavelet transformed EXAFS signal along the  $k$  and  $r$  coordinates corresponding to maximum magnitude of wavelet transformed signal

<sup>1</sup>Contour plots display the projection of the z-axis on to the x-y plane of the paper and in WT the z-axis corresponds to the magnitude of wavelet transform

#### 4. Multi-resolution wavelet analysis of EXAFS spectra

As a note of caution, it is noted that spurious transform artifacts could easily be misinterpreted as due to real structure feature when a structure model has to be fit to the data. In this regard, the danger of spurious peaks is even higher in WT compared to FT due to several variables and parameters that could affect the outcome of the WT. The centers of the WT contour plots with maximum intensity were surveyed for each  $k$ -weighting scheme and the values are tabulated in table 4.3.

##### 4.3.2. Limitations in resolution achievable using Morlet wavelets

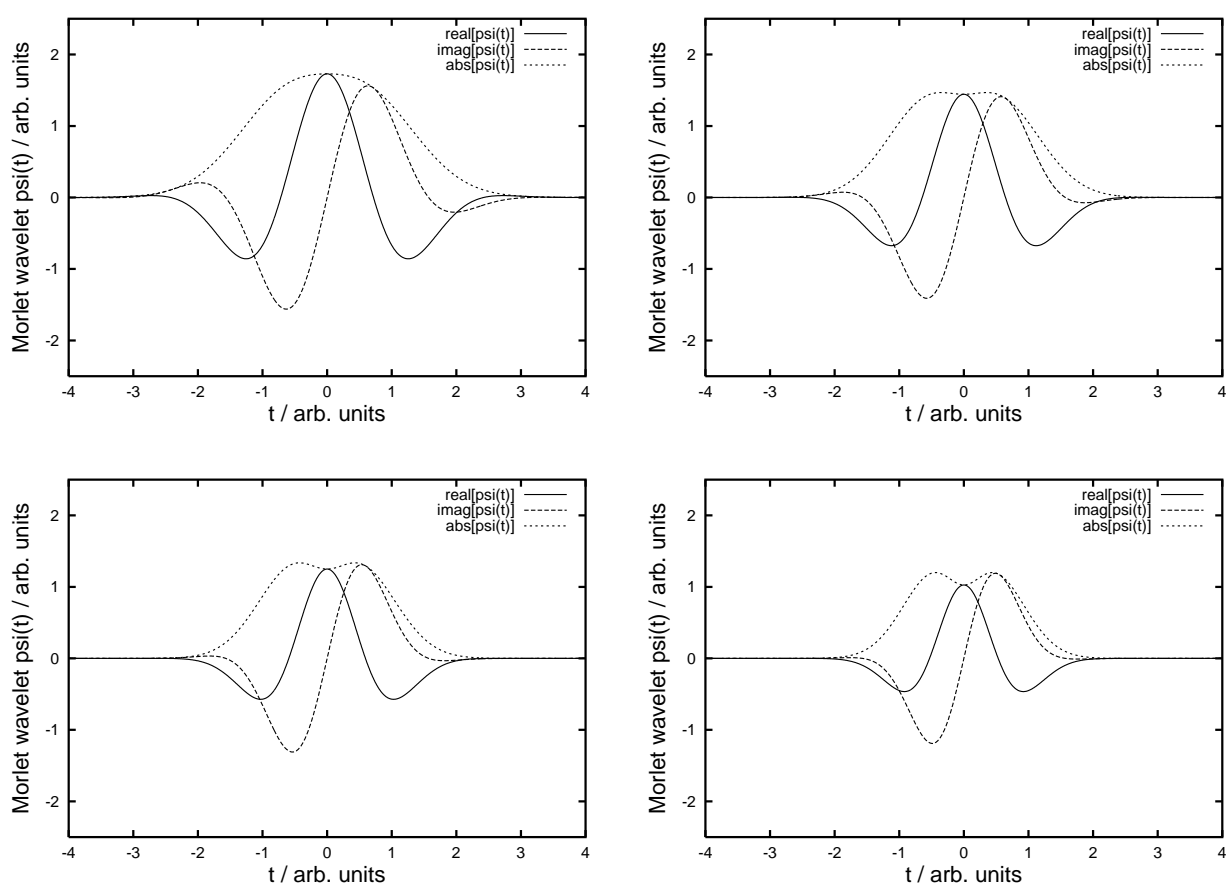


Figure 4.7.: Wavelet of type 2 as a function of variable  $t$  with  $\kappa = 2$ ;  $\sigma = \{1, 0.8, 0.7, 0.6\}$  (top left–bottom right)

One important limitation of WT will be discussed in this section and general conclusions will be drawn about the choice of wavelets suitable for usage in signal analysis and a simple screening procedure will be outlined. While Morlet wavelets overcome a

major drawback of fixed time-frequency resolution by providing flexibility in controlling the number of oscillations in the Gaussian envelope as shown for type 1 and type 2 wavelets, another important limitation exists. As shown in figure 4.7, with lower  $\sigma$  values like 1 the envelope of the wavelet is still unimodal but when values less than 1 were used, uni-modality changes to bi-modality with a split envelope [52].

Wavelet transform of a signal, for example the model EXAFS signal 2 with only Ag–Ag contribution, using a wavelet with bimodal envelope results in spurious artifacts seen at more than one  $k$ -center. Further, such a feature could easily be misunderstood to be due to a different type of backscatterer.

### 4.3.3. Effect of superposition of two constituent signals on the wavelet transform

In the case discussed so far, the Ag–Au and Ag–Ag bond distances in model 1 were the same. In real systems however, this may not be the case always and the separation of the two centers also has a marked effect on the resolution obtained using wavelet transform. To be able to resolve this issue for a real system it is informative to simulate similar scenarios using a model signal consisting of two parts whose centers are sequentially set apart and then subjected to investigation using a range of different wavelets. Moreover additional tests with the same model signal but with different amplitudes for the two parts were also carried out. This in turn would simulate real time EXAFS contribution from different type of atoms located at close distances and within the same FT peak.

The input signals with  $\Delta C = \{1, 2, 3, 4, 5\}$  and their FT spectra are given in figure 4.8 which were subjected to WT using Morlet wavelet with four sets of parameters namely  $\kappa = \{5, 4, 3, 2\}$  and  $\sigma = \{1\}$ . As observed in figure 4.8 all the signals exhibit similar FT modulus and they convey little to no information about varying  $\Delta C$ , other than the frequency of the individual components that constitute the signal. After an extensive test with different wavelet transform parameters for the model signals subjected to FT, a set of wavelet transforms were obtained using suitable WT parameters and they are presented in figures 4.9–4.13 denoting the WT parameters used.

From the WT presented in these figures, it is clear that the information content of WT is better when compared to FT and it is also found to be highly dependent upon the

#### 4. Multi-resolution wavelet analysis of EXAFS spectra

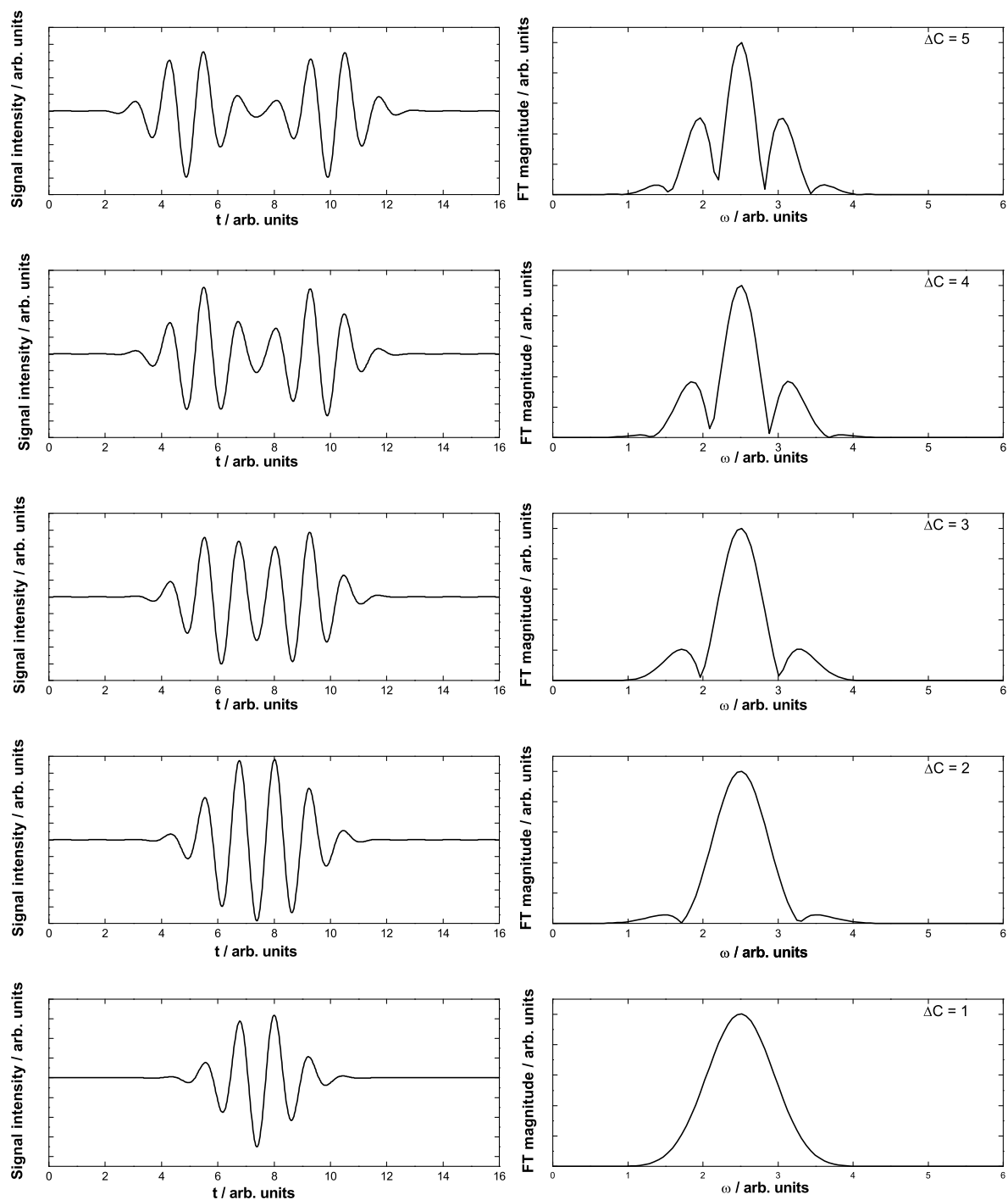


Figure 4.8.: Model input signals with different  $\Delta C$  values (given on the figures in the right side) and their FT modulus



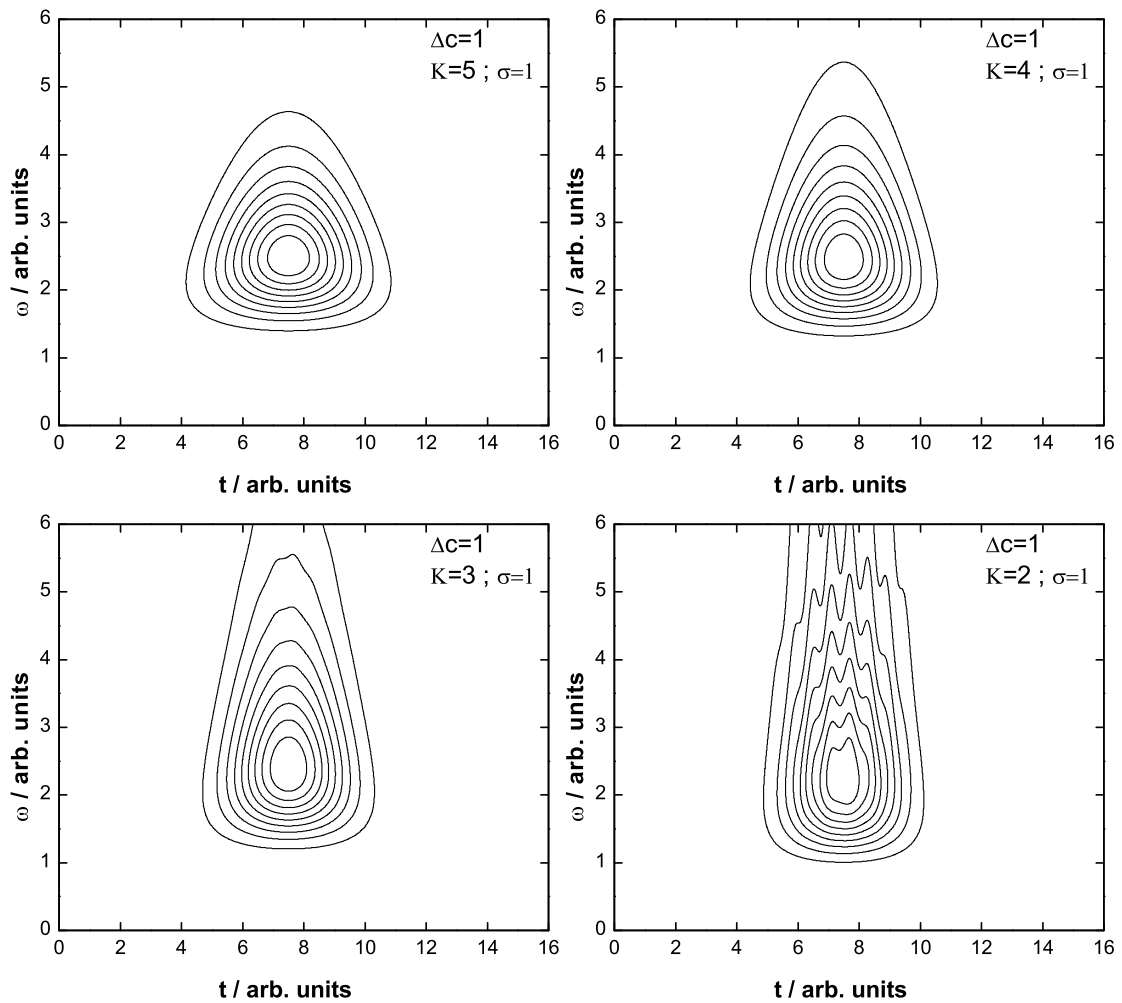


Figure 4.9.: Wavelet transform of the input signal with  $\Delta C=1$  using different wavelet parameters given with each plot

transform parameters used. Artifacts are observed with smaller  $\sigma$  values used in WT for all the signals but the transform helps to identify the presence of two components in the signal, unlike in the FT modulus. Only for signals whose  $\Delta C \geq 2$ , WT is able to show the presence of two distinct signals.

In EXAFS signal analogy, by using the relation  $t \Rightarrow k$  and  $2\pi\omega \Rightarrow 2r$ , this means that only signals whose centers of  $F(A)$  envelopes are well separated in  $k$  space can be resolved using WT. On the other hand, the WT of signals  $\Delta C \geq 2$  demonstrate that WT can be

#### 4. Multi-resolution wavelet analysis of EXAFS spectra

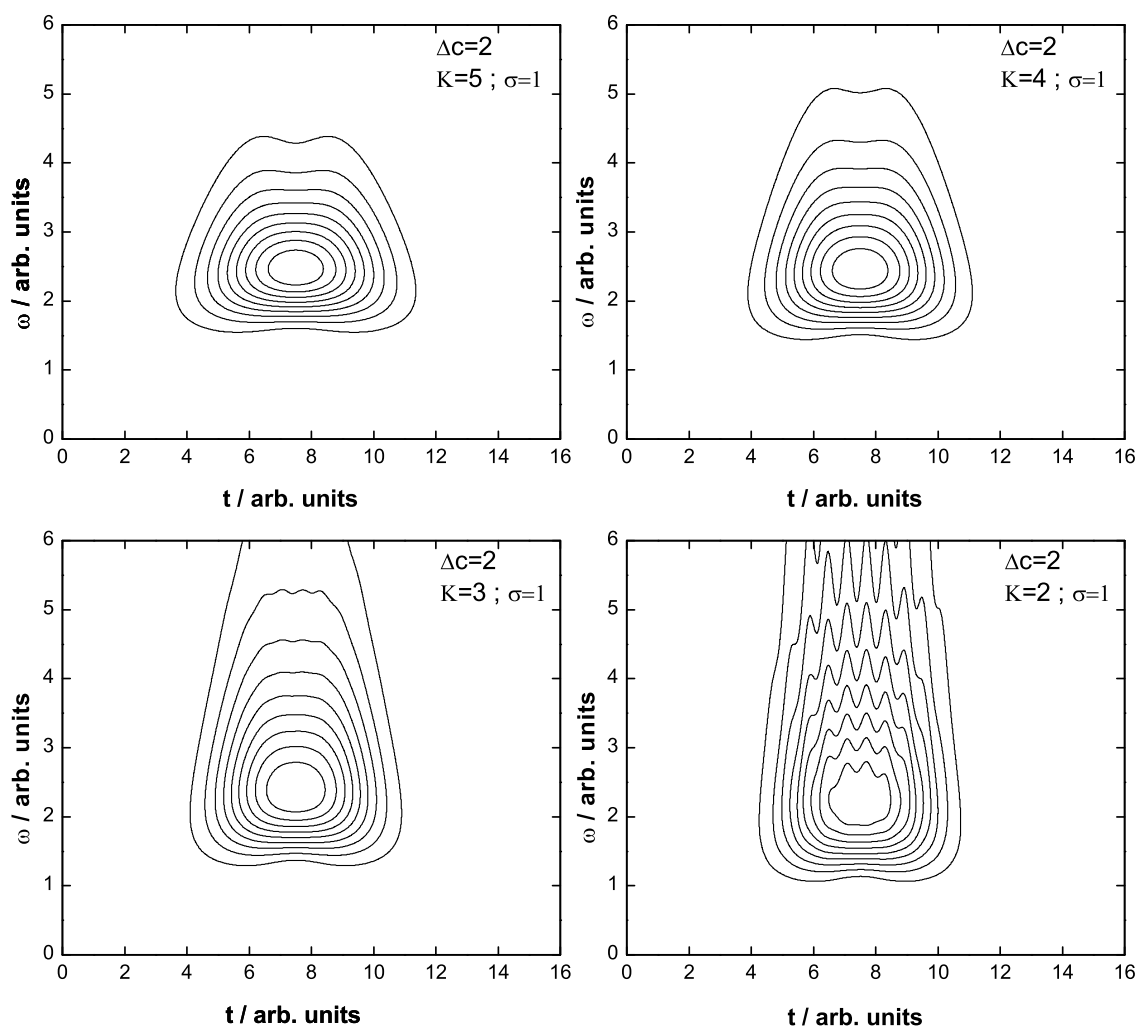


Figure 4.10.: Wavelet transform of the input signal with  $\Delta C=2$  using different wavelet parameters given with each plot

used to complement FT to discern contributions from two signals in a composite signal.

For composite signals with  $\Delta C$  values of 1 and 2, even a wavelet with  $\kappa=\{2\}$  and  $\sigma=\{1\}$  is not sufficient to resolve the individual components and using lower  $\sigma$  values is not permitted due to the bimodal behavior of wavelet. For signals with  $\Delta C=2$ , WT using  $\kappa=\{3\}$  and  $\sigma=\{1\}$  wavelet is at least required to achieve the desired result of identifying two constituent signals. In the case of signals with  $\Delta C \geq 3$  though, all the

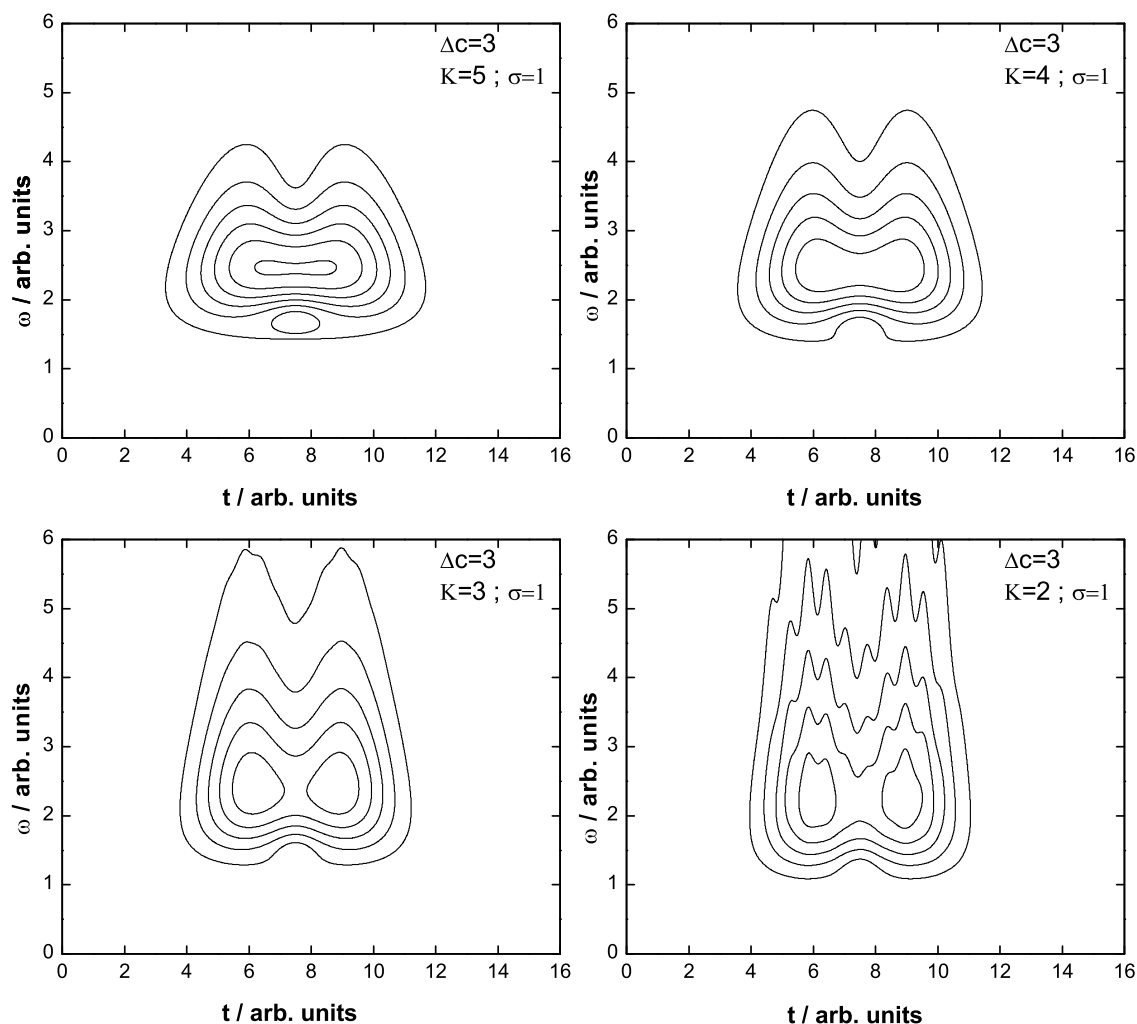


Figure 4.11.: Wavelet transform of the input signal with  $\Delta C=3$  using different wavelet parameters given with each plot

five Morlet wavelets provide the desired result showing two distinct signals with good resolution.

In defining the composite signal so far, the amplitude of the two constituent signals were chosen to be the same but in reality it is found that even a difference in amplitude of the constituent signals with a large  $\Delta C$  has a marked effect on the effectiveness of WT. Only when the amplitude difference is large, say for example the  $F(A)$  variation observed for a low atomic number scattering contribution and a high atomic number contribution, will it be possible to use WT for EXAFS analysis.

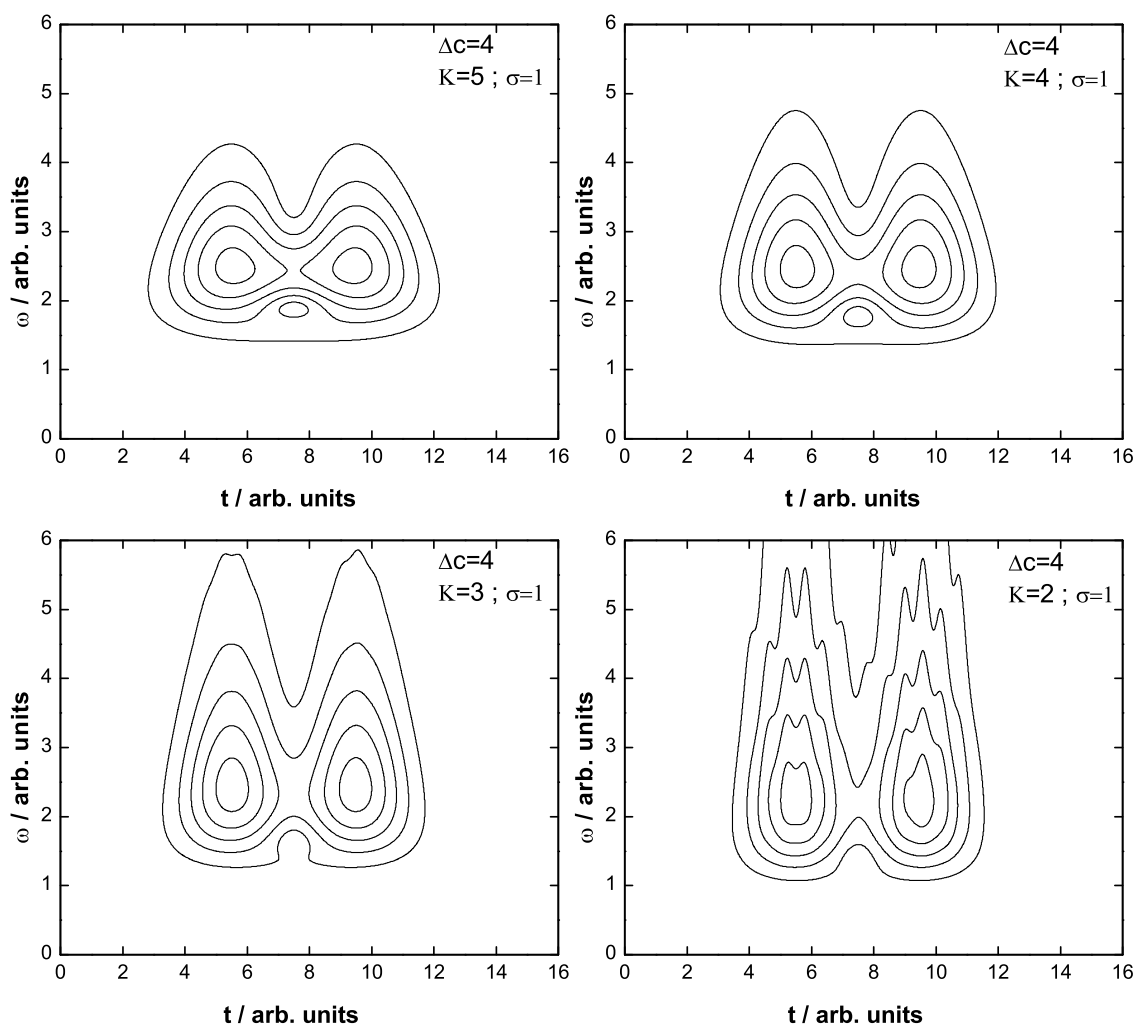


Figure 4.12.: Wavelet transform of the input signal with  $\Delta C=4$  using different wavelet parameters given with each plot

In conclusion, WT using Morlet wavelets has been demonstrated to be useful in EXAFS analysis complementing the FT for special cases where a straightforward theoretical model fitting is difficult. Limitations and boundaries exist as to what kind of wavelets are actually able to provide the required resolution in  $k$ - $r$  space. The complexity of the input signal plays an important role in the outcome of the WT in EXAFS analysis. Clear indications about various factors that contribute to spurious signals in WT like higher  $k$ -weighting and amplitude of the signals were suggested. Feasibility of using WT analysis

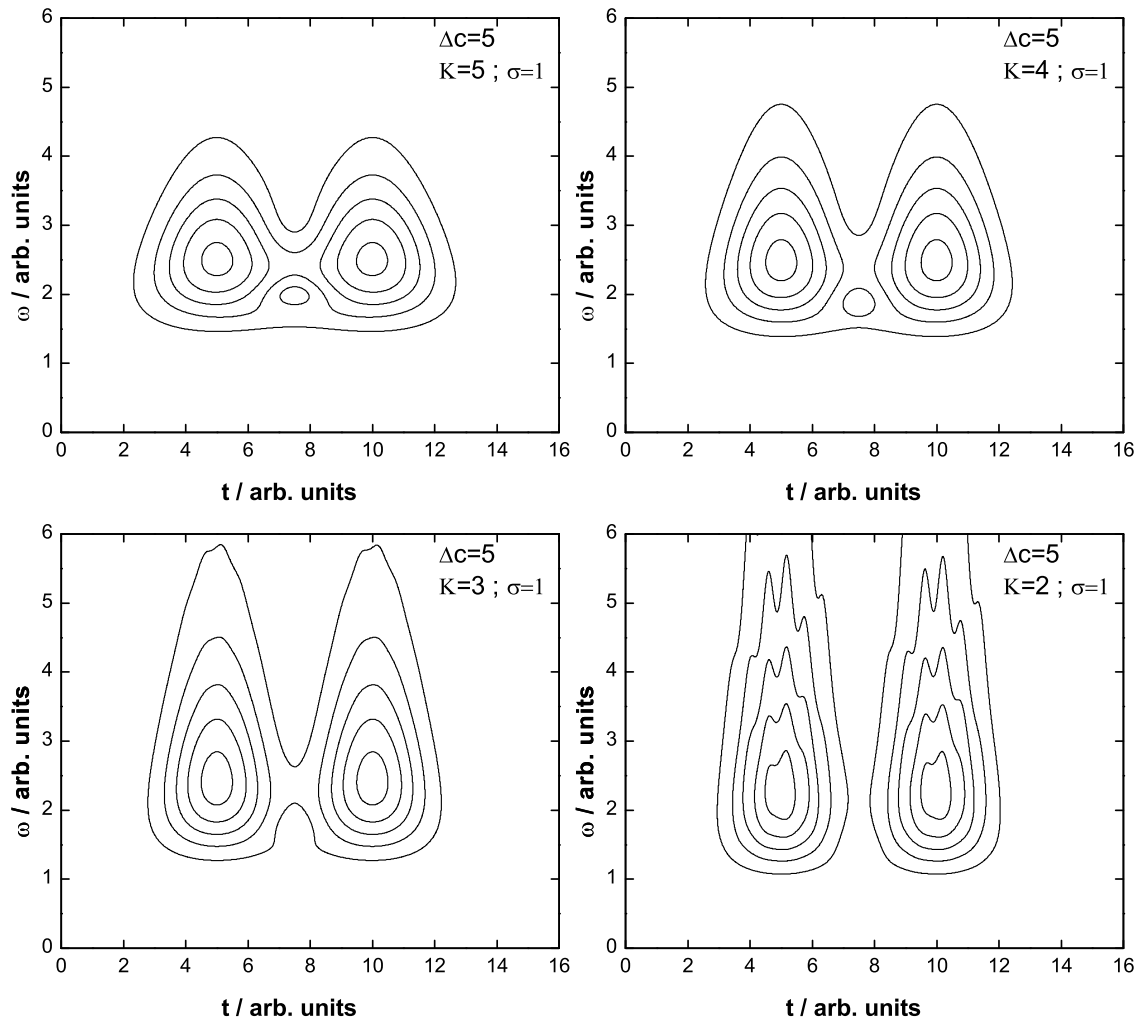


Figure 4.13.: Wavelet transform of the input signal with  $\Delta C=5$  using different wavelet parameters given with each plot

for model signals with varying complexities defined using different constituent signals was demonstrated.



# 5. Ruthenium based catalysts in zeolite

## 5.1. Introduction

Supported catalysts represent the largest group of heterogeneous catalysts and are of major economic importance, especially in refinery technology and the chemical industry. Supported catalysts are heterogeneous catalysts in which small amounts of catalytically active material, especially metals or metal oxides, are anchored to the surface of porous, mostly inert solids. Typical catalyst supports include porous solids such as aluminum oxides, silica gel, MgO, TiO<sub>2</sub>, ZrO<sub>2</sub>, aluminosilicates, zeolites, activated carbon and ceramics. The reasons for the predominant use of supported catalysts in industry are many including easy isolation of product, cost, activity, selectivity and ease of regeneration which are influenced by the type of support used [56].

In the design of shape and size selective catalysts, confined geometries and size defined clusters of active species like metal or metal oxide play a crucial role. Zeolites provide confined geometries which can be utilized to control accessibility of the active center to reactants as well as growth of the clusters within [57, 58]. However, in order to reap the confinement benefits of zeolites in practice, successful synthesis procedures of such materials should be developed. Yet another important step in this direction is to structurally characterize these materials and verify the confinement of guest clusters in the zeolite pores by common analytical methods like IR, NMR, ESR, Mössbauer and other spectroscopic techniques, which are used to characterize catalysts on support. By using x-ray structure determination methods, it can be ascertained whether a particular preparation method is able to produce the desired catalyst materials. However, when the guest clusters are not detectable by diffraction experiments either due to lack of long range order or very small size or a mixture of both, it becomes impossible to directly verify whether encapsulation was successful.

XAS provides an opportunity to investigate such difficult cases and to throw light on the success or failure in encapsulation of active centers by a particular preparation method. Compared to the straight forward XAS analysis in metal clusters the XAS analysis is inherently more tedious in oxides due to their structural complexity, thermal disorder, effect of multiple scattering and above all availability of authentic model compounds [59]. In addition to the afore mentioned concerns, verifying that the metal oxide clusters are indeed mono dispersed in size is very difficult. Care was therefore taken in the present EXAFS analysis that instead of accumulating numbers for the coordination numbers, interatomic distances and disorder for numerous coordination shells, to develop and test plausible theoretical structure models and report if a given model confers with the experimental data or not. EXAFS spectra of model compounds were thoroughly investigated before the samples of interest were investigated.

Ruthenium oxide clusters were previously deposited in FAU (faujasite) [60], MFI (ZSM-5) [61] and encapsulated in LTA [62, 63] zeolite cages using hydrothermal synthesis and XAS was used to probe the ruthenium oxidation state after reductive or oxidative treatments [64]. Competitive hydrogenation experiments specific to a zeolite type complements the XAS results and provide valuable information about the location of clusters in zeolites [63]. Ruthenium in encapsulated ruthenium oxide which interact strongly with the zeolite host through Ru–O–Si linkages are difficult to reduce under mild reduction conditions (below 393 K) whereas Ru in larger ruthenium oxide domains are easier to reduce. Weakly interacting Ru in zeolites with counter ions of Na<sup>+</sup> or K<sup>+</sup> also undergo rapid reduction compared to strongly interacting Ru–O–Si in RuO<sub>2</sub> grafted onto hydroxylated SiO<sub>2</sub> surfaces [64, 65].

Zeolite carrier materials with ruthenium as guest were prepared, structurally characterized and tested for catalytic activity within the framework of SFB706 *Selective oxidation of n-alkanes with molecular oxygen*, under project A1. The catalytically active metal or metal oxide centers of ruthenium were immobilized in wide and narrow pore structured matrices of Silicalite-1, Na-A and Na-ZSM-5. The preparation of the materials were carried out by the research group of Prof. Weitkamp and the preparation method has been published elsewhere [61]. Ru K edge XAS measurements of the resulting materials were carried out primarily to ascertain the oxidation state, coordination geometry and local environment of Ru. More specifically the EXAFS investigations were aimed at getting information about the presence of either dispersed or agglomerated



clusters, dimensions of the clusters and presence of Ru–O–Si type interactions. Structure models for Ru species in zeolite were constructed based upon the extensive crystal structure data available for Ru compounds with oxide ligands [66, 67] and theoretical EXAFS spectra of the various models were generated using the multiple-scattering EXAFS formalism of FEFF6. Good fit of a particular theory model to experimental EXAFS spectrum of a catalyst was used as a criteria to choose an appropriate model to describe the real system.

Among several aspects which need to be taken into account to build structure models for Ru catalysts the role of zeolite structure is very important. Zeolites exist in numerous varieties which range from very narrow pores to wide open pore systems, three-dimensional intersections of different channels to one-dimensional pore systems, charged zeolites to cation stabilized ones *etc* [68]. Some basic structure aspects of the zeolite framework types used in this study and electronic and structure aspects of ruthenium oxide and ruthenium hydroxide are presented in the following section.

### 5.1.1. Zeolites

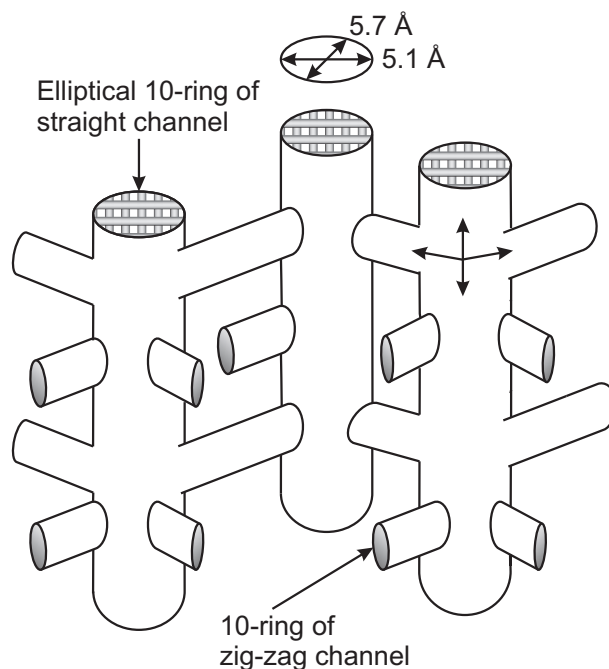


Figure 5.1.: Idealized picture of channel system in silicate shown along with the dimensions of the channels

The origins of inorganic molecular sieves go back to 1756, when the Swedish mineralogist Cronstedt first discovered intriguing crystals in nature that seemed to froth or boil when heated in a blowpipe flame. Cronstedt called this new mineral a *zeolite*, derived from the Greek words, *zeo* meaning *to boil* and *lithos* meaning *a stone*. Compared to the early times, the zeolite nomenclature is well established today by the International Zeolite Association (IZA). Three letter framework-type codes suggested by the IZA [68] will be used to refer to the zeolite frameworks used in this study, namely MFI and LTA.

Silicalite-1 and ZSM-5 belong to the MFI framework type and their basic building units are tetrahedral Si–O entities. Silicalite is a polymorph of SiO<sub>2</sub> and has a tetrahedral framework that encloses a three dimensional system of intersecting channels defined by 10-member rings of oxygen ions wide enough to adsorb molecules up to 0.6 nm diameter [69]. Silicalite is hydrophobic and is stable under heat treatment up to 1300 °C. The idealized channel system in silicalite and the dimensions of the straight channel are given in figure 5.1 [69].

The basic building blocks of SiO<sub>4</sub> tetrahedra can be combined in arrays with sharing oxygen atoms and form a secondary building unit (SBU) comprised of 12T atoms, where T is an aluminum or silicon atom and is given in figure 5.2 for the building scheme for MFI [68, 70]. These SBUs can be linked to form chains and such chains can be generated by applying the operations of 2-fold screw axis to a SBU. Such chains can then be interconnected to form layer as outlined in figure 5.3.

When the chemical composition of a zeolite is given by  $A_{(x/y)}^{m+} [(SiO_2)(AlO_2^-)_y] \cdot zH_2O$  where  $A^{m+}$  is the counter ion, the ratio  $(x/y)$  is given in terms of  $(n_{Si}/n_{Al})$ . The Si end member of the ZSM-5 compositional series of  $(n_{Si}/n_{Al})$  is called Silicalite and when some Si atoms in this structure are replaced by Al atoms, the resulting aluminosilicate is referred to as ZSM-5, an industrially important catalyst [71].

Another secondary building block called sodalite can be visualized as an arrangement of 24 primary building blocks, namely, SiO<sub>4</sub> and AlO<sub>4</sub> tetrahedra to form a truncated octahedron. When the sodalite cages are stacked in a widely spaced manner connected by bridging oxygen ions between the four-membered oxygen rings, an interesting structure called zeolite-A [72] is obtained and is depicted in figure 5.4.

Zeolites can be classified as either wide, medium or narrow-pored materials and the pore dimensions of LTA and MFI zeolites used in this study are given in table 5.1 [71].

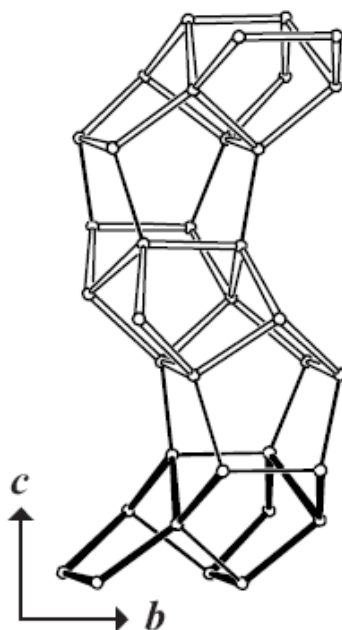


Figure 5.2.: Secondary building unit (bold) along with the chain-type building block

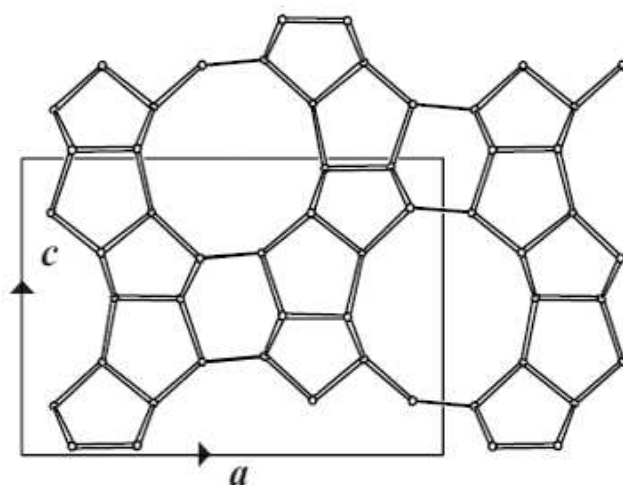


Figure 5.3.: Skeletal diagram of ZSM-5 layer with the chains of figure 5.2 around the channel opening

### 5.1.2. Local structure of ruthenium oxide and hydroxide

Pure  $\text{RuO}_2$  is a metallic conductor due to a d-band conduction mechanism [73]. Single crystals of anhydrous  $\text{RuO}_2$  exhibit conductivity on the order of  $10^4 \text{ S cm}^{-1}$  at

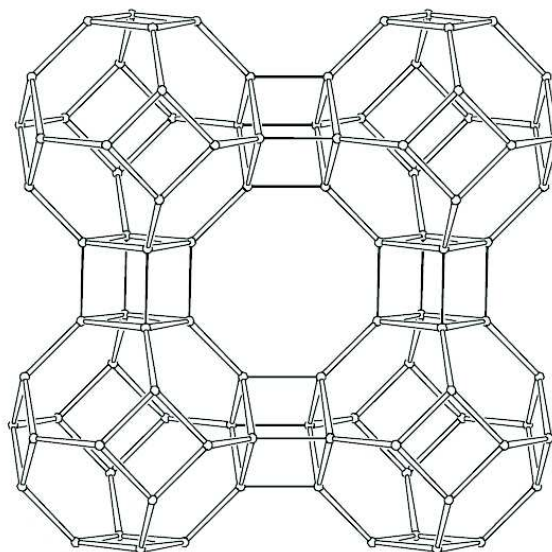


Figure 5.4.: Depiction of sodalite cages connected to form Zeolite-A

Zeolite	No. of oxygen atoms in the ring	Dimension of 10 ring aperture / nm
ZSM-5 or Silicalite	10	0.51x0.55 ; 0.54x0.56
Zeolite-A	8	0.41

Table 5.1.: Zeolites used in this study and their pore dimensions

20 °C [74, 75]. Anhydrous  $\text{RuO}_2$  finds application as a thick-film resistor [76], while hydrous ruthenium oxide is preferred in electro catalysis [77].  $\text{RuO}_2$  electrodes are typically prepared by thermal decomposition of  $\text{RuCl}_3 \cdot y\text{H}_2\text{O}$ , producing materials which are hydrous and more correctly described as  $\text{RuO}_x \cdot y\text{H}_2\text{O}$  or  $\text{RuO}_x\text{H}_y$  [77, 78].

Structure of  $\text{RuO}_x \cdot y\text{H}_2\text{O}$  has earlier been investigated by McKeown *et al.* [79] using TGA, XRD and XAS and its implications on charge storage and electrochemical properties were documented. The disorder in the structure of the Ru–O octahedra in the material is related to the amount of water of hydration of  $\text{RuO}_2$  and larger the degree of hydration, larger is the disorder in the structure. The structure models proposed by McKeown *et al.* [79] for mildly hydrated ruthenium oxide denoted as  $\text{RuO}_2 \cdot 0.29 \text{H}_2\text{O}$  and strongly hydrated ruthenium oxide denoted as  $\text{RuO}_2 \cdot 2.32 \text{H}_2\text{O}$  based on XAS analysis are reproduced in figure 5.5 for a quick overview.

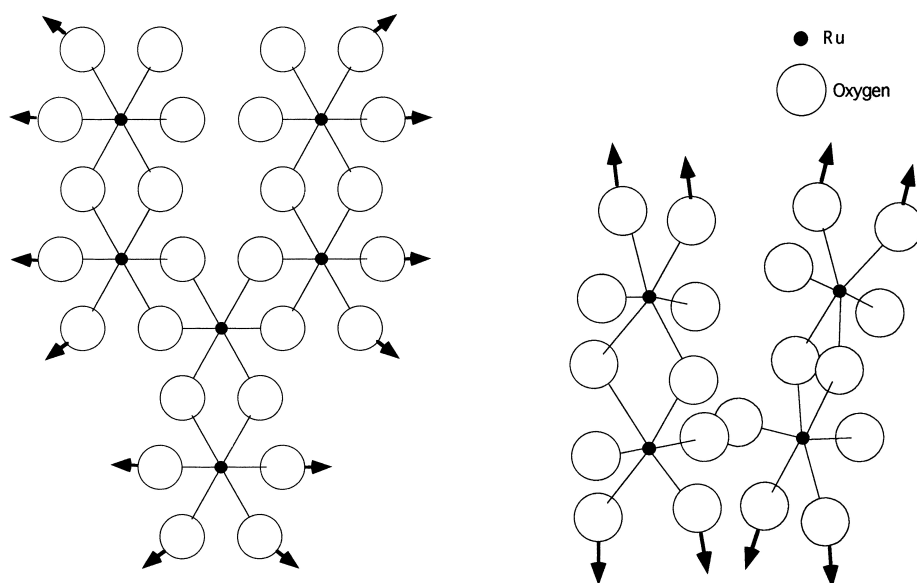


Figure 5.5.: Structure models of  $\text{RuO}_2 \cdot 0.29\text{H}_2\text{O}$  featuring  $\text{RuO}_6$  octahedral dimers (left) and  $\text{RuO}_2 \cdot 2.32\text{H}_2\text{O}$  (right) with disordered  $\text{RuO}_6$  linked in twisted unconnected chains [79]

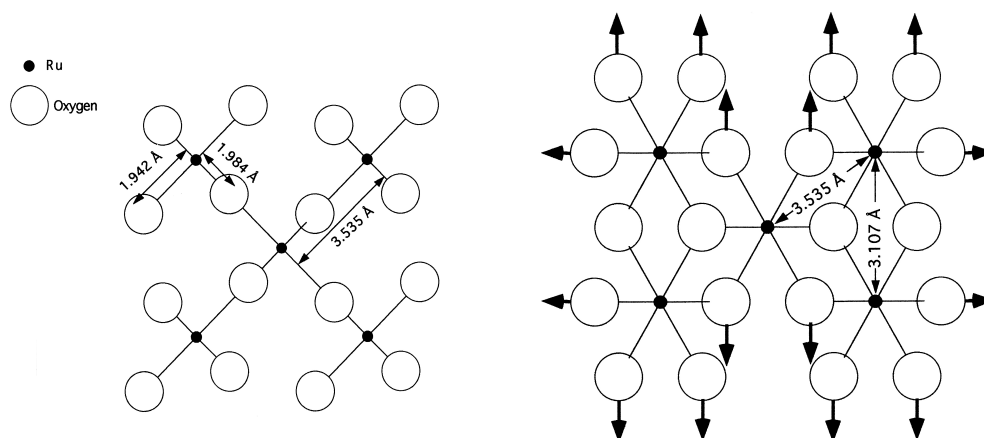


Figure 5.6.: Structure model of anhydrous  $\text{RuO}_2$  featuring c-axis projection (left) and b-axis projection (right) [79]

Similarly, the  $\text{RuO}_2$  crystal structure with Ru–O and Ru–Ru bond distances for anhydrous sample is presented in figure 5.6 where the vertical arrows indicate an infinitely extending chain and horizontal arrows indicate chains connected perpendicular to the c-axis.

### 5.1.3. In situ XAS set up

Prior to in situ measurements, normal XAS spectra of Ru catalysts and the references were measured at the Ru K edge at 22117 eV at X1 and C beamlines at HASYLAB at DESY, Hamburg using a double crystal Si (311) monochromator in energy scanning mode. Anhydrous ruthenium dioxide reference and Ru/Si1-c and Ru/Si2-c samples were measured in a quartz tube sample holder and the other catalyst samples as pellet on 1.3 cm diameter in transmission mode.

In the structure determination of chemically sensitive catalyst materials it is important to verify if samples measured under in situ and ex situ conditions yield same results. In many cases when the results are not the same there is a need for in situ treatment of the catalyst in a special cell to avoid contamination of the catalyst surface by oxygen or any other gas. The high dispersion of the active material on the support of a heterogeneous catalyst makes this material very vulnerable to attack by gaseous compounds.

The active material in 1 g of catalyst may easily have a surface area of a few square meters and this amount can, for instance, be covered by all oxygen molecules present as a 1 ppm impurity in 1000 L of inert gas [19]. This means that the contents of an ordinary glove box, which is filled with an extremely pure inert gas, contains enough oxygen to cover and transform the active material present in a 1 g catalyst sample. Results obtained on catalysts that have been exposed to air, even for very short periods of time, cannot be trusted to represent the actual catalyst and even results obtained from catalysts handled in good quality glove boxes should not be taken for granted. Therefore, catalyst preparation has to be performed in in situ cells, in which both treatment and measurement can be carried out. In order to investigate the heterogeneous catalysts by XAS after reductive or oxidative treatments an in situ set up is helpful. Therefore a specialized in situ XAS set up like a flow reactor, referred to as quartz cell, for heterogeneous catalysis was designed, constructed and tested. During the period when the quartz cell was under development, significant modifications and improvements to an already existing set up for pelletized sample was carried out to couple the cell to a mass spectrometer. Gas mixing, regulation of flow rate and remote operation of the mass flow controllers which are common to both the set ups, were developed and tested at different XAS beam lines in Hamburg and Karlsruhe. The newly designed set up will be called quartz cell and the modified set up, copper cell.

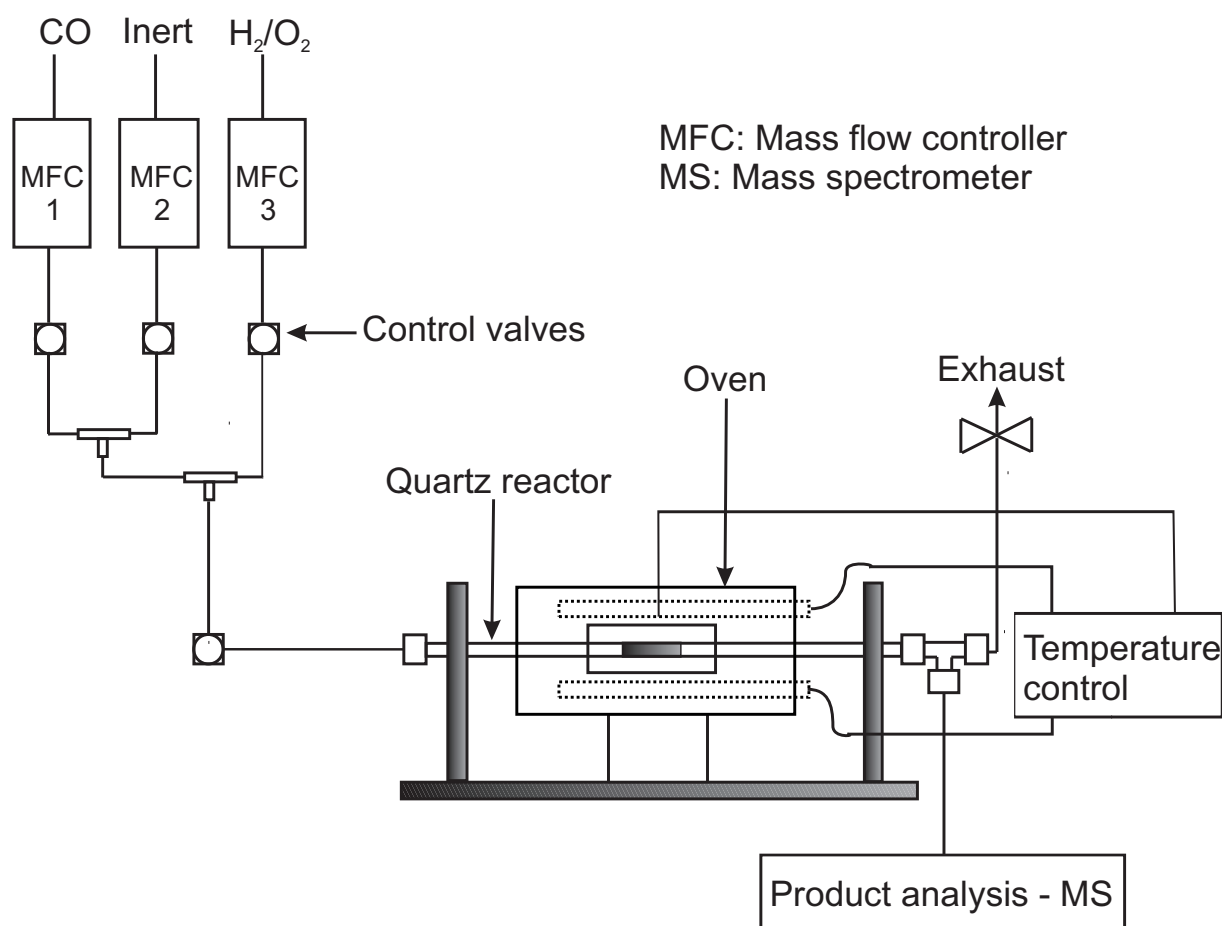


Figure 5.7.: Schematic of the quartz catalytic reactor used as high-temperature flow reactor and simultaneously as a good x-ray transmission cell for XAS measurements along with the gas mixing and supply unit

### Quartz cell

The quartz catalytic reactor can be used as high-temperature flow reactor and simultaneously as a good x-ray transmission cell for XAS measurements. The sample in the quartz cell should preferably be in powdered or granulated form, so that gas can flow through it without considerable pressure drop across the catalyst bed. This particular in situ cell has the advantage that one can use powdered or sieved catalytic material without having to grind and press a disk from it.

Inconel alloy heating oven, three-part fused thin walled quartz tube catalytic reactor, ultra-tight gas fittings to connect quartz to a metal tube for outlet and inlet gases are

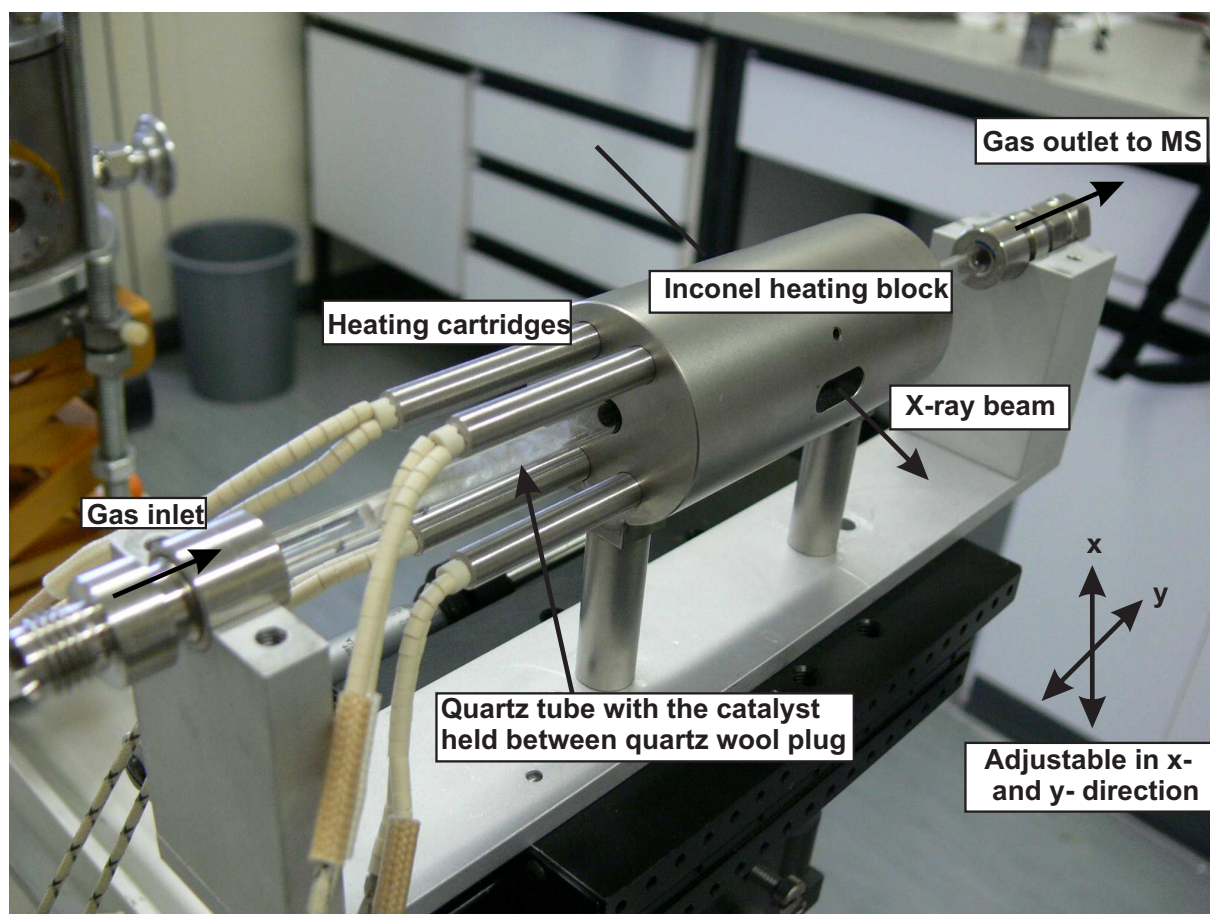


Figure 5.8.: Picture of the quartz cell with an operating temperature range starting from RT to 623 K

some of the essential components of the set up as shown in figure 5.7. The oven with open windows for the incident and exiting x-ray beam is heated using four heat cartridges two above and two below the quartz tube to minimize temperature gradient as shown in figures 5.7 and 5.8. Sieved catalyst is filled in the quartz tube and sealed on both ends by quartz wool which permits gas flow and minimize pressure drop across the catalyst bed. This set-up has been tested until 350 °C using  $ZrO_2$  powder under gas flow. This set up can be coupled to a mass spectrometer and the gas supply system with ultra-tight Swagelok fittings. In figure 5.8, the direction of the x-ray beam and the gas flow are marked along with the vertical and horizontal alignment possibilities of the mounting device. Testing of the quartz cell was carried out at beam lines X1 and C



at HASYLAB Hamburg and beam line XAS at ANKA Karlsruhe after conforming to the safety regulations of the respective facilities.

Compact design and good heat isolation for temperatures up to 350 °C, adjustable x-y axis table mount with micrometer precision (Newport instruments) provide quick installation and focusing of the synchrotron x-ray beam on to the sample inside the quartz tube. Alignment of the sample cell in the beam at XAS beamline of ANKA was performed with a x-ray camera. Eurotherm controller and K-type thermocouple were used for temperature measurement and regulation which were later extended to include automatic temperature recording mechanism in a given time interval using a Labjack module.

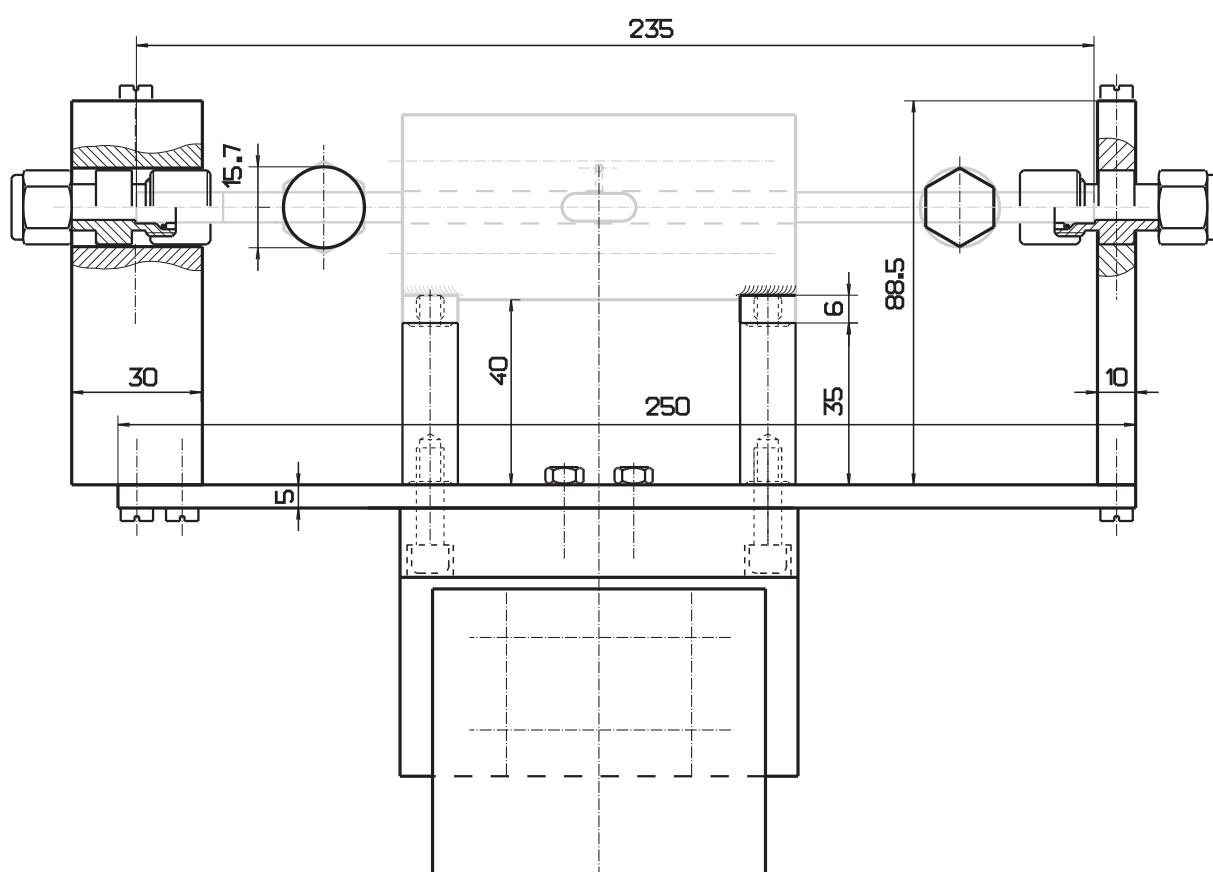


Figure 5.9.: Technical drawing of the adjustable mounting platform of the inconel alloy heating block and the modified ultra-tight gas connectors used to connect the metal tubes to the quartz reactor (dimensions given in mm)

## 5. Ruthenium based catalysts in zeolite

The quartz cell was filled with the sieved catalyst as grains of defined size distribution. XAS spectra of anhydrous  $\text{RuO}_2$  was measured using the quartz tube as sample holder and EXAFS signal in the  $k$ -interval ( $3 \leq k \leq 18$ )  $\text{\AA}^{-1}$  was obtained.

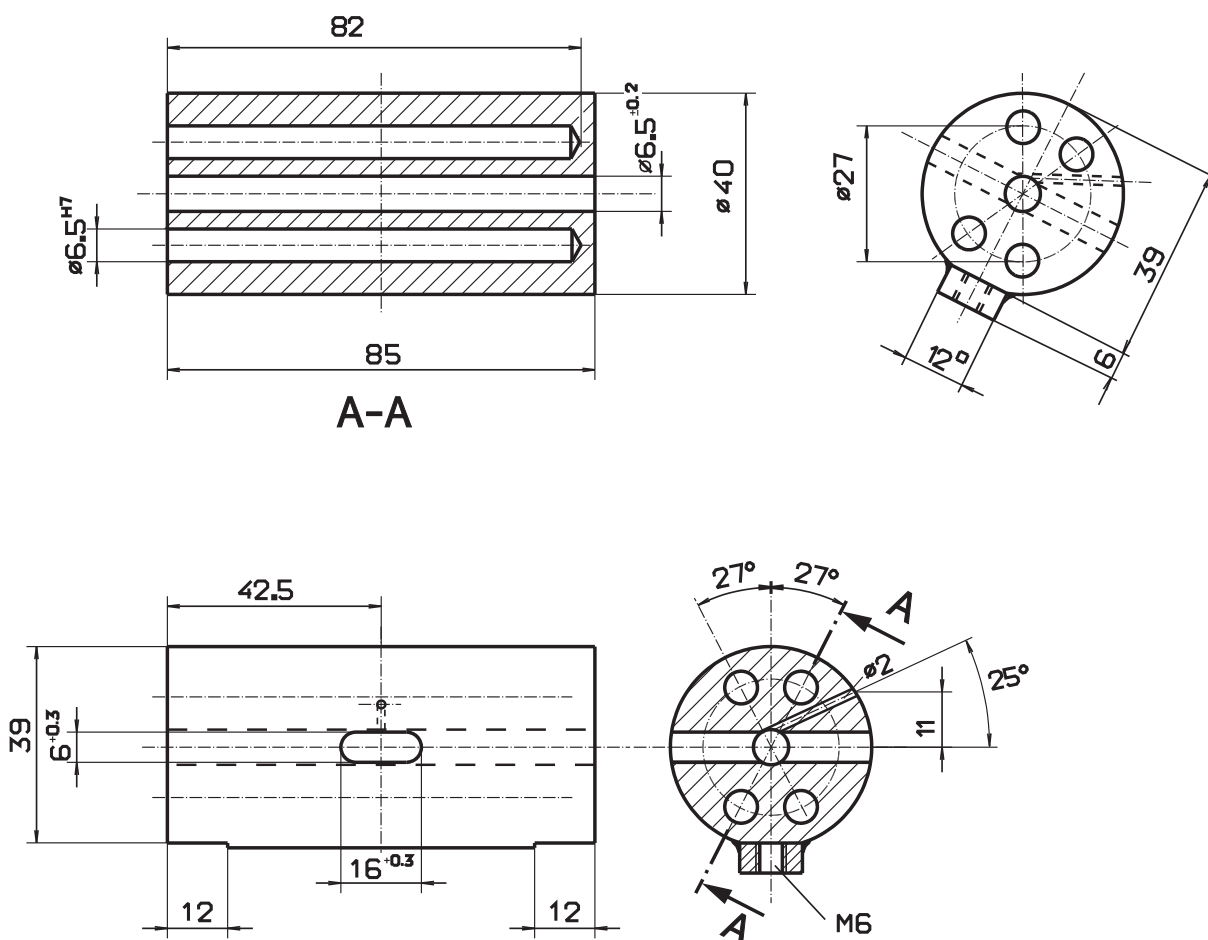


Figure 5.10.: Technical drawing of the inconel alloy heating block of the quartz cell indicating the dimensions in mm

### Copper cell

A copper cell was developed in our group to investigate platinum catalyst as pellets [80]. The copper cell is given in 5.11 and the following modifications were carried out to the set up.

- Coupling of the copper cell to a mass spectrometer to analyze the outlet gases

- Changing to an efficient heating and temperature control module for easy operation
- Electrical isolation according to the safety regulation prescribed by HASYLAB at DESY, Hamburg

The copper cell was coupled to a mass spectrometer with unit *amu* resolution installed at HASYLAB. Short residence time of the exhaust gas in the exit line essential to correlate the mass data with the XAS data correctly was achieved by using very short stainless steel capillary tube of diameter (1/16) inch. The exhaust line is heated to prevent any condensation of gaseous products before reaching the mass analyzer. At the exhaust line, a non return valve was used to prevent back flow of atmospheric air or gas into the reactor.

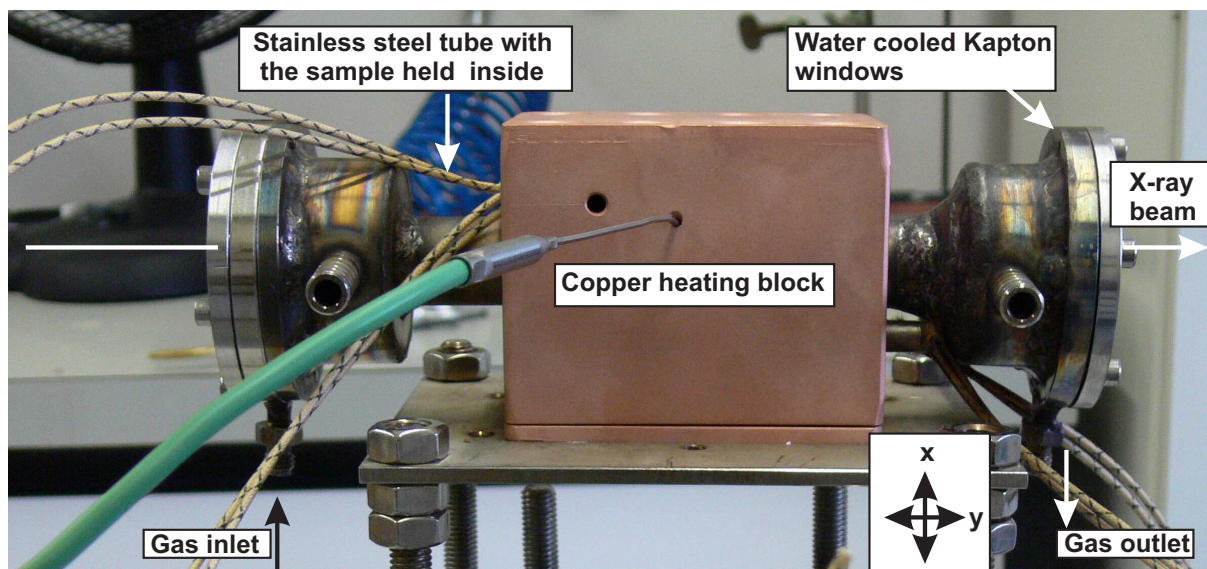


Figure 5.11.: Stainless steel cell with temperature range from RT to 553 K

### Gas-mixing and supply

The flow of gases to the reactor was controlled by Bronkhorst mass flow controllers (MFC). Regulation of gas supply inside the beam line hutch during XAS measurements required certain commands to be sent to the MFCs from outside the beam line hutch. This was achieved with the help of remotely controlled digital MFC through a computer interface. Additionally a gas mixing unit as shown earlier in figure 5.7 was constructed

using three analog MFCs to prepare mixtures of different gases which was fitted with Swagelok regulator valves and taps which operate even with reactive and corrosive gases. The gas mixing unit was built in such a way as to minimize dead volume for the gases and prior to the deployment of the MFCs in measurement, they were calibrated using a simple soap bubble meter.

## 5.2. Results and discussion

### 5.2.1. XANES investigation

The zeolite supported ruthenium catalysts investigated by XAS are listed in table 5.2 along with the type of the zeolite used.

Sample	Zeolite	wt% of Ru	pre-treatment
1 Ru/Si1-1	Silicalite-1	0.52	not calcined
3 Ru/Si2-c	Silicalite-1	0.38	calcined
4 Ru/Si1-c	Silicalite-1	0.56	calcined
6 Ru/NaA1	Na-A	0.40	not calcined
7 Ru/NaA2	Na, K-[Al,Ru]-A	0.51	not calcined
9 Ru/ZSM-5-c	Na-ZSM-5	1.10	calcined
References			
1	$K_2RuO_4$		
2	$RuO_2$ -Anhydrous		
3	$RuO_2$ -Hydrous ( $RuO_2 \cdot xH_2O$ )		
4	Ru-metal		

Table 5.2.: Ruthenium containing zeolite samples and the references used in the XAS investigation

Characteristic features in the XANES of reference materials can be used as fingerprints to indicate the phases present in a catalyst material. The signatures in XANES are marked with straight lines given in XANES spectra of samples presented in figures 5.12 and 5.13. The discussion with respect to the catalyst materials using a fingerprint approach is given in the following paragraphs.

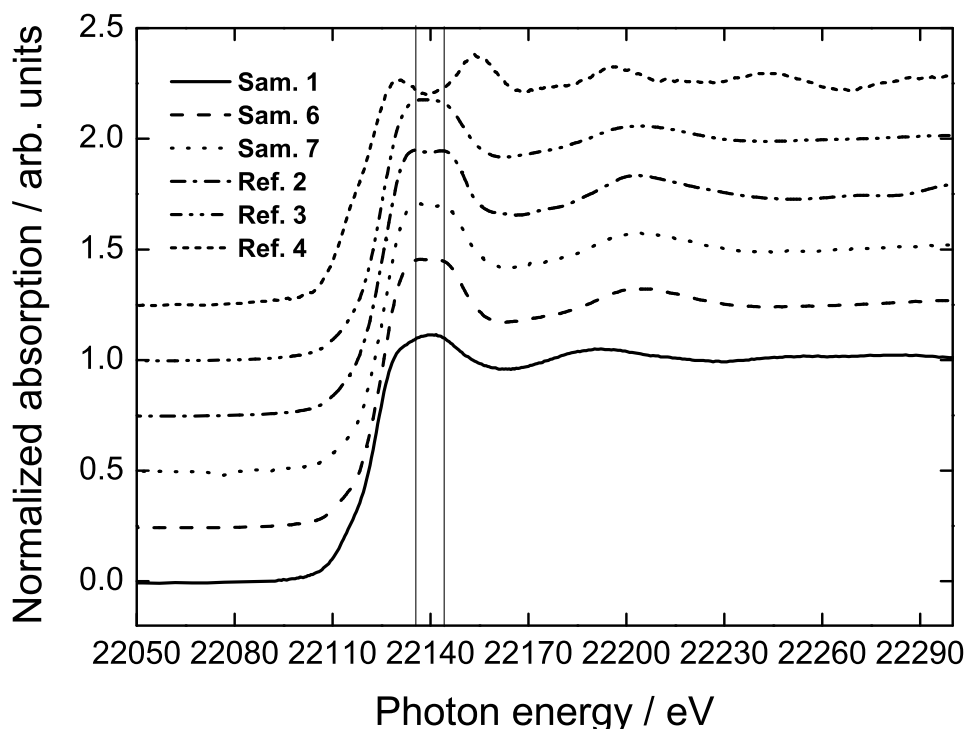


Figure 5.12.: Ruthenium K edge XANES spectra of reference samples of Ru-metal, anhydrous RuO<sub>2</sub>, hydrous RuO<sub>2</sub> and ruthenium catalysts without the calcination step. For the notation see table 5.2

At the Ru K edge, the XANES spectra of Ru-metal and anhydrous RuO<sub>2</sub> have some distinctive features. The half-maximum of the unit normalized XANES spectra of Ru-metal is shifted by roughly 6 eV from anhydrous RuO<sub>2</sub> on the low energy side. Moreover, in anhydrous RuO<sub>2</sub>, a split peak (first at 22135 eV and second at 22143 eV) immediately after the absorption edge is visible with a saddle point. Ru-metal, on the other hand has two peaks (first at 22130 eV and second at 22154 eV) with a minimum in between which coincides with the saddle point of anhydrous RuO<sub>2</sub>. Unlike in anhydrous RuO<sub>2</sub> no split double peak is observed in hydrous RuO<sub>2</sub> but the edge energies remain the same. This minimal difference in the XANES region signifies that the local structure around Ru in RuO<sub>2</sub> changes with hydration.

The oxidation state of ruthenium in all the samples investigated is similar to that in anhydrous RuO<sub>2</sub> and hydrous RuO<sub>2</sub>, i.e. +IV. This is reflected by the similar XANES spectra of RuO<sub>2</sub> and samples Ru/Si2-c, Ru/Si1-c and Ru/ZSM-5-c. Upon closer look at the XANES spectra, in the region near the absorption edge, ruthenium in silicalite

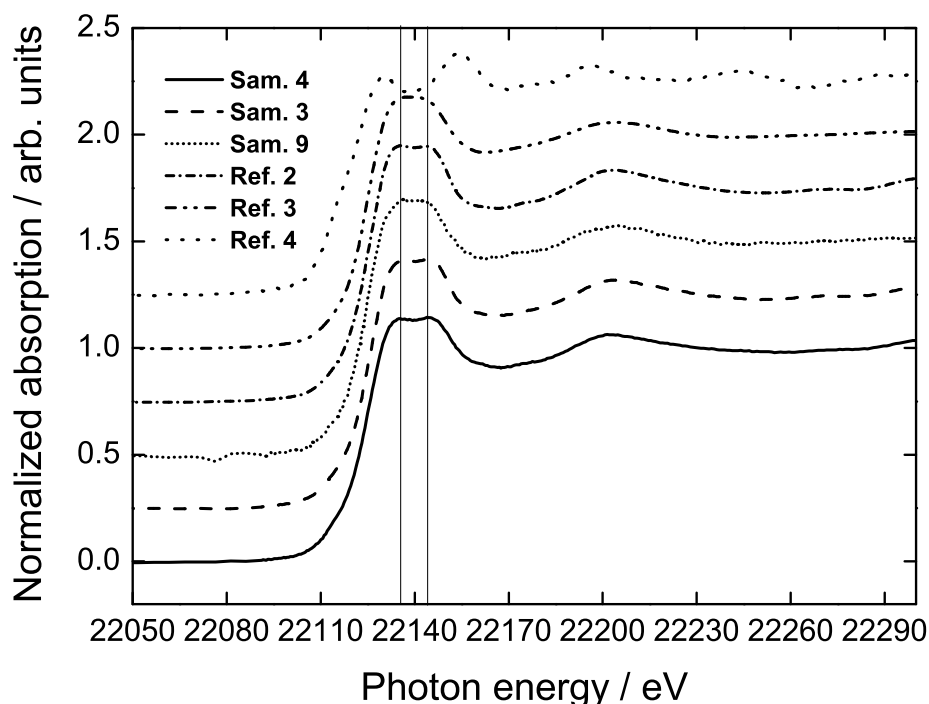


Figure 5.13.: Ruthenium K edge XANES spectra of reference samples of Ru-metal, anhydrous  $\text{RuO}_2$ , hydrous  $\text{RuO}_2$  and ruthenium catalysts after calcination post-treatment. For the notation see table 5.2

samples Ru/Si1-c and Ru/Si2-c which differ in the ruthenium content only exhibit two maxima like in anhydrous  $\text{RuO}_2$ . On the other hand samples Ru/Si1, Ru/NaA2 and Ru/ZSM-5-c exhibit only one maximum like in hydrous  $\text{RuO}_2$ . These differences suggest that the calcined samples in silicalite-1 are similar to the anhydrous  $\text{RuO}_2$  with the rutile modification consisting of Ru–O octahedra and not the structurally disordered hydrous  $\text{RuO}_2$ .

Samples Ru/Si1 and Ru/Si1-c as the names suggest refer to the same preparation type and zeolite material but prepared with and without calcination post-treatment in order to study the effect of calcination on local structure. While the XANES region of Ru/Si1 neither resembles anhydrous nor hydrous  $\text{RuO}_2$ , it resembles the XANES region of the starting material of  $\text{RuCl}_3$  used as a precursor in the synthesis [60]. Upon calcination of Ru/Si1, the XANES region of Ru/Si1-c looks completely different which suggests that upon calcination Ru is completely oxidized to Ru (IV). The similarity of the zeolite loaded ruthenium samples with either anhydrous or hydrous  $\text{RuO}_2$  clearly suggests that

the samples have nearest neighbor octahedral  $\text{RuO}_6$  environment similar to the oxide references used. Further evidences to this effect were also obtained from a detailed EXAFS analysis outlined in section 5.2.2.

In situ XANES investigation was performed on one of the ruthenium in NaA zeolite sample, Ru/NaA2 during its reduction under  $25 \text{ ml min}^{-1}$   $\text{H}_2$  flow at 393.15 K. The feasibility of reduction of ruthenium containing zeolite Y at a temperature of 393 K has earlier been used to gather insights into the local structure of Ru [64]. The XANES spectrum of the sample was measured at two different temperatures and at different time intervals of in situ treatment.

The exact conditions used in the experiment called a, b, c and d for short explanation are listed in table 5.3 and the corresponding in situ XANES spectra measured at each step are compared in figure 5.14.

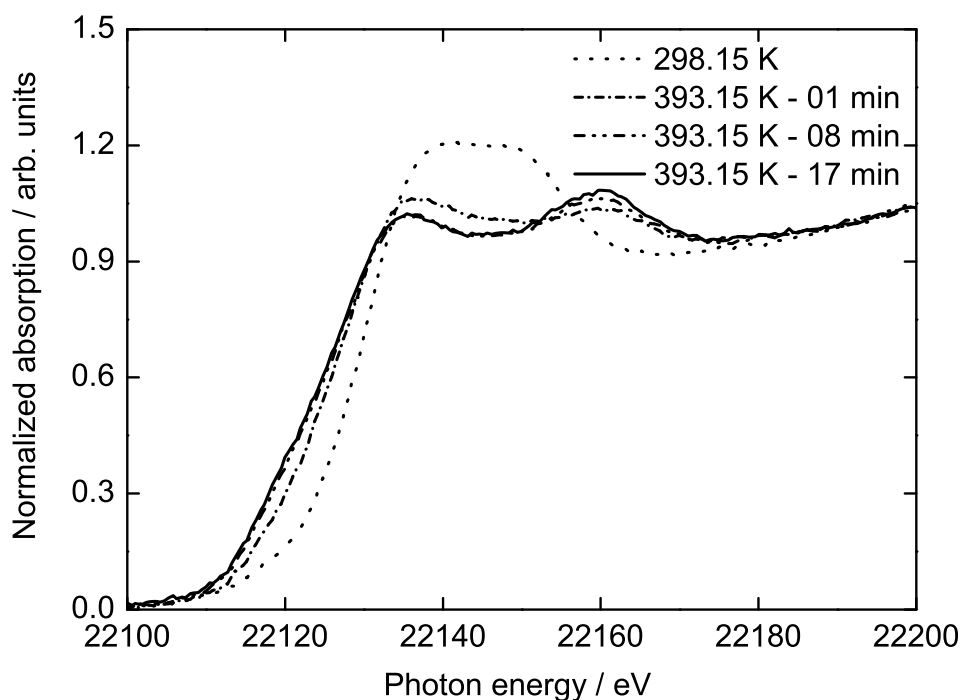


Figure 5.14.: XANES region of sample 7 at 393.15 K under hydrogen flow and minutes after reduction measured in situ under  $25 \text{ ml min}^{-1}$  hydrogen gas flow. For comparison the XANES spectrum of the sample before reduction is also given

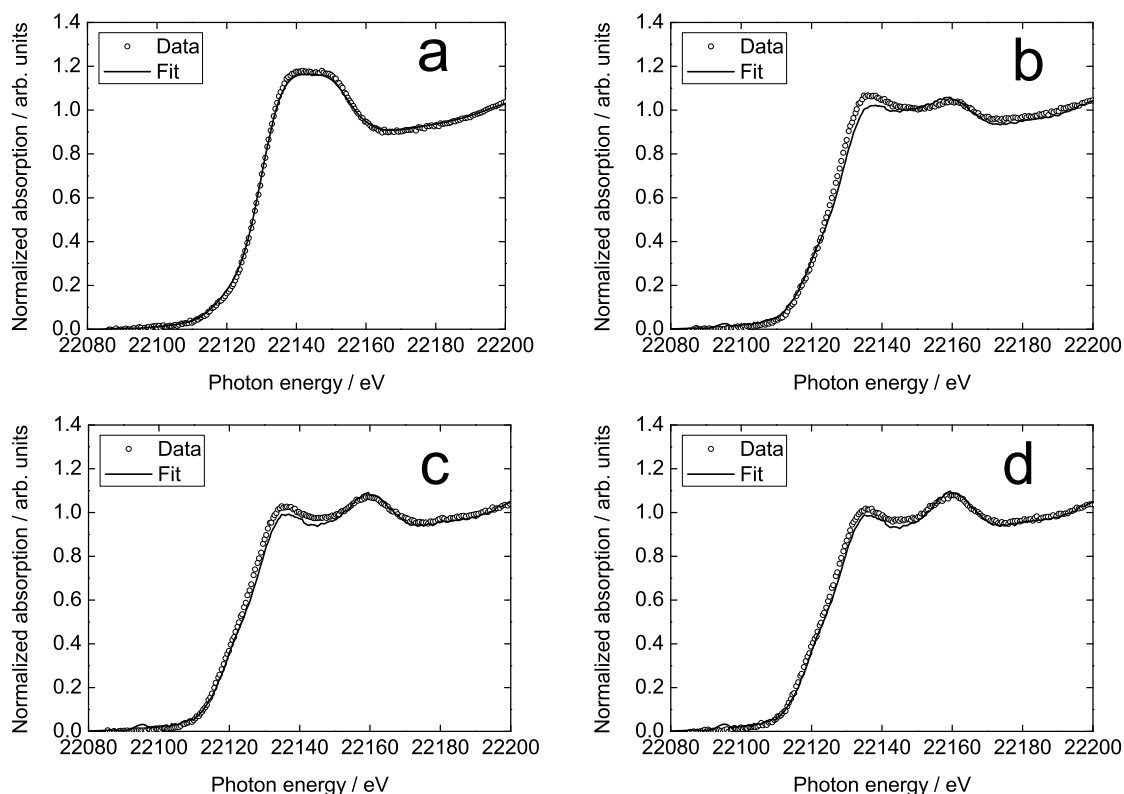


Figure 5.15.: XANES spectra of Ru/NaA2 at measurement conditions of a–d along with the fit obtained as a linear combination of XANES spectra of hydrous RuO<sub>2</sub> and Ru-metal

Time dependent changes, both in the absorption edge position and shape of the double peak, are observed for the sample at 393.15 K. Initially upon heating Ru/NaA2 under 25 ml min<sup>-1</sup> hydrogen gas flow, from room temperature up to 393.15 K, a weakly split double peak very close to the edge characteristic to hydrous RuO<sub>2</sub> is observed. Later, the shape changes to a broader overlying peak that resembles Ru-metal. From a hydrous RuO<sub>2</sub> species in higher oxidation state, Ru-metal is generated upon reduction. Therefore, linear combination XANES (LC-XANES) fit was carried out using hydrous RuO<sub>2</sub> and Ru-metal as references and the weighting factors of each component in the measured spectra were obtained. The normalized XANES spectra were fitted using routine procedure in the energy range of 22080–22200 eV. LC-XANES fit to the measured spectra are presented in figure 5.15 and the results in terms of weighting factor of the two reference spectra necessary to obtain a good fit are given in table 5.3.



Sample 7 Ru/NaA2	Weighting of hydrous RuO <sub>2</sub>	Weighting of Ru-metal
a (at 298.15 K)	1.000	0.000
b (at 393.15 K for 1 min)	0.296±0.017	0.704±0.017
c (at 393.15 K for 8 min)	0.072±0.015	0.928±0.012
d (at 393.15 K for 17 min)	0.032±0.013	0.968±0.013

Table 5.3.: Weighting fraction of the reference spectra determined by LC-XANES fit for sample NaA2 measured under different conditions

From the weighting fractions of the two components and the XANES spectra presented in figure 5.14 it can be inferred that after 17 min of hydrogen flow at 393.15 K, the sample completely resembles Ru-metal, which proves the feasibility to reduce Ru/NaA2 sample 7 under mild conditions within a relatively short period. This observation also indicates that the catalytic active species when ruthenium oxide loaded zeolites are used under reductive atmosphere is metallic ruthenium. Complete reduction of RuO<sub>2</sub> to Ru-metal is also confirmed by weighting fraction LC-XANES analysis of the XANES spectra.

Another possible reason for the facile reduction under mild conditions could be that highly dispersed ruthenium particles in zeolites have a oxide layer and this surface oxide layer is reduced upon contact with hydrogen. Such observations were earlier reported [81] in the XANES studies of carbon supported Pt-Ru electro catalyst for polymer electrolyte fuel cells where metallic ruthenium was observed during in situ studies. For the present case however, the scenario of dispersed hydrous RuO<sub>2</sub> with weak interactions with the zeolite walls seems to match with the EXAFS results obtained for the samples. Similar in situ experiments for each sample taken up in this study could provide more valuable information about the cluster-host interactions, but the availability of precious measurement time at synchrotron radiation sources is an important factor to be taken into consideration.

### 5.2.2. EXAFS investigation

EXAFS analysis of metal oxides is complicated compared to pure metals due to their structural complexity, thermal disorder, effect of multiple scattering and the availability of authentic model compounds [59]. To tackle these problems in the EXAFS analysis of RuO<sub>2</sub> catalysts in zeolites, FEFF based EXAFS analysis was carried out. With the help of good reference compounds of anhydrous RuO<sub>2</sub> and hydrous RuO<sub>2</sub> the boundaries of determining structure parameters were deduced.

FEFF code [82] is known to offer the possibility to calculate theoretical EXAFS paths originating from different absorption sites which might be present in a complex oxide material and the possibility to identify and list out all important single and multiple scattering paths for a given arrangement of atoms within a defined distance around the absorbing atom. Structural chemistry of inorganic oxides is often complex due to non-equal sites which are very similar. An approach where a low point symmetry is accounted for in terms of disorder which is not a Gaussian distribution of interatomic distances about an average could lead to unrealistic structure parameters [59].

### 5.2.3. Theoretical standards in EXAFS analysis

Once  $\chi(k)$  has been isolated from the measured absorption spectra as explained in the appendix section, the EXAFS equation can be used to extract the atomic species, coordination numbers and interatomic distances of the neighboring atoms from the absorbing atom. There are different approaches to determine these parameters using a prior knowledge of the scattering amplitudes and phase shifts. Most commonly among them is the method using theoretically calculated backscattering amplitude and phase shifts from first principles like the FEFF code.

General approach for determining the local structure around the absorber atom from EXAFS data is to build a structure model and calculate the theoretical EXAFS spectrum for that model using the FEFF program. Programs such as Artemis is used to adjust the structure parameters in the EXAFS equation 5.1 until a least squares fit is obtained between the theoretical and experimental EXAFS spectra. The model can be adjusted as required for example with different atom types, until a best possible fit is obtained between theoretical and experimental spectra.

The EXAFS equation can be written in terms of a sum of the contribution from all  $i$  scattering paths of the photoelectron:

$$\chi(k) = \sum_i \chi_i(k) \quad (5.1)$$

where each path  $\chi_i(k)$  can be written in the form:

$$\chi_i(k) = \frac{(N_i S_0^2) F_i(k)}{k R_i^2} \sin[2k R_i + \varphi_i(k)] \exp(-2\sigma_i^2 k^2) \exp\left(\frac{-2R_i}{\lambda(k)}\right) \quad (5.2)$$

$$R_i = R_{\text{eff}i} + \Delta R_i. \quad (5.3)$$

The kinetic energy of the photoelectron expressed in magnitude of change of the wave vector  $k$  using the mass of the electron  $m_e$  and Planck's constant  $\hbar$  is given by:

$$k^2 = \frac{2m_e (E - E_0 + \Delta E_0)}{\hbar^2} \quad (5.4)$$

The terms used in the equations which are calculated by the FEFF program are explained in the list given below:

- $F_i$ : Effective scattering amplitude of the photoelectron from the atom of type  $i$
- $\varphi_i(k)$ : Phase shift experienced by the photoelectron scattered by atom of type  $i$
- $\lambda(k)$ : Mean free path of the photoelectron
- $\sin[2k R_i + \varphi_i(k)]$ : This term accounts for the oscillations in the EXAFS signal with a phase given by  $2k R_i + \varphi_i(k)$ . The path of the photoelectron is described by  $(2R_i)$  (the distance to the neighboring atom and then back to the absorber atom), which is multiplied by  $k$  to determine the phase.

$R_i$  is the half path length of the photoelectron which is the distance between the absorber and neighboring atom for a single-scattering event and  $R_{\text{eff}i}$  is the half path length given as input for example from crystal structure data, to the theoretical calculation which can be modified by  $\Delta R_i$  during fitting.

The remaining variables determined by fitting a model to the EXAFS spectrum are explained as follows:

- $N_i S_0^2$ : For single scattering,  $N_i$  represents the number of coordinating atoms within a particular shell called the degeneracy of a single scattering path. For multiple scattering  $N_i$  represents the number of identical paths. The passive electron reduction factor ( $S_0^2$ ) usually has values between 0.7 and 1.0. ( $S_0^2$ ) accounts for the slight relaxation of the remaining electrons in the presence of the core hole vacated by the photoelectron.
- $F_i(k)$ : Effective scattering amplitude. For single scattering path it is the atomic scattering path used in x-ray diffraction. This term accounts for the element sensitivity of EXAFS. Atoms with more more electrons scatter photoelectrons more strongly at higher wavenumbers.
- $\Delta R_i$ : This term represents the change to the interatomic distance relative to the initial path length  $R_i$  and can be changed to fit the model to the data.
- $\sigma^2$ : This term accounts for the disorder in the interatomic distances. Specifically in EXAFS,  $\sigma^2$  is the mean-square displacement of the bond length between the absorber atom and the neighboring atoms in a shell. This term has contributions from dynamic (thermal) disorder and static (structural heterogeneity) disorder. The EXAFS process occurs on the femtosecond time scale ( $10^{-15}$  s), while thermal vibrations occur on a much longer time scale of  $10^{-10}$  s to  $10^{-12}$  s. On a simplifying assumption that the atoms are essentially *frozen* at one position about their energy minima during the fast excitation process, EXAFS probes the distribution of distances between the absorber atom and each of the neighboring atoms within a shell in terms of a  $\sigma^2$  value.
- $\Delta E_i$ : This term relates to a change in the photoelectron energy. This value is used to align the energy scale of the theoretical spectrum to match the extracted EXAFS spectrum from a measurement. This parameter can be different for various coordination shells but is more often constant for all the paths used in the model.

Once a model for the EXAFS parameters to be evaluated has been developed, the variable parameters in the EXAFS equation and the mathematical variables used to related parameters of different paths are adjusted to arrive at least-squares fit between the experimental and theoretical spectra. A typical output from the fitting procedure include the user defined variables, their best fit values, the uncertainties in these variables, along with important information about the statistics of the model.

Statistical parameters include the number of independent data points  $N_{\text{idp}}$ , number of iterated variables  $N_{\text{var}}$  which is less than the number of independent points, chi-square  $\chi^2$  and reduced chi-square  $\chi^2_{\nu}$  values and R factor [83, 84]. The R factor is the sum of squares of the differences between the data and the fit at each data point, divided by the sum of squares of the data at each corresponding point. For fit results in  $r$  space, the data points considered for the calculation are from the real and imaginary parts of the Fourier transform.

$$\text{R factor} = \frac{\sum_i (\text{data}_i - \text{fit}_i)^2}{\sum_i \text{data}_i^2} \quad (5.5)$$

The  $\chi^2$  value is the sum of squares of the difference between the resulting fit and the data divided by the uncertainties ( $\varepsilon$ ) at each data point ( $i$ ).

$$\chi^2 = \frac{N_{\text{idp}}}{N_{\text{pts}}} \sum_i \left( \frac{\text{data}_i - \text{fit}_i}{\varepsilon_i} \right)^2 \quad (5.6)$$

where  $N_{\text{idp}}$  is the number of independent points in the fitted theoretical model given by Nyquist theorem:

$$N_{\text{idp}} = \frac{2}{\pi} \Delta k \Delta r + 1 \quad (5.7)$$

where  $\Delta k$  is the data range subjected to Fourier transform and  $\Delta r$  is the  $r$  range used in the data analysis.

For EXAFS analysis, since the uncertainties are not well defined, the  $\varepsilon$  value is based upon the amplitude of the EXAFS signal at distances of 15–25 Å where there is rarely any contribution from atoms at these distances. Reduced chi-square  $\chi^2_{\nu}$  is calculated by dividing  $\chi^2$  by the number of degrees of freedom in the fit  $\nu$  given by the difference between the number of independent points in the experimental spectra and the number of variables fit in the theoretical model.

### Rutile anhydrous RuO<sub>2</sub> reference

Crystal structure parameters of RuO<sub>2</sub> reported by Bolzan *et al.* [66] were used to generate the  $x$ ,  $y$ ,  $z$  coordinates of Ru and O atoms necessary for the FEFF input file. Initially for a cluster size of 7 Å, possible list of all FEFF single and multiple scattering

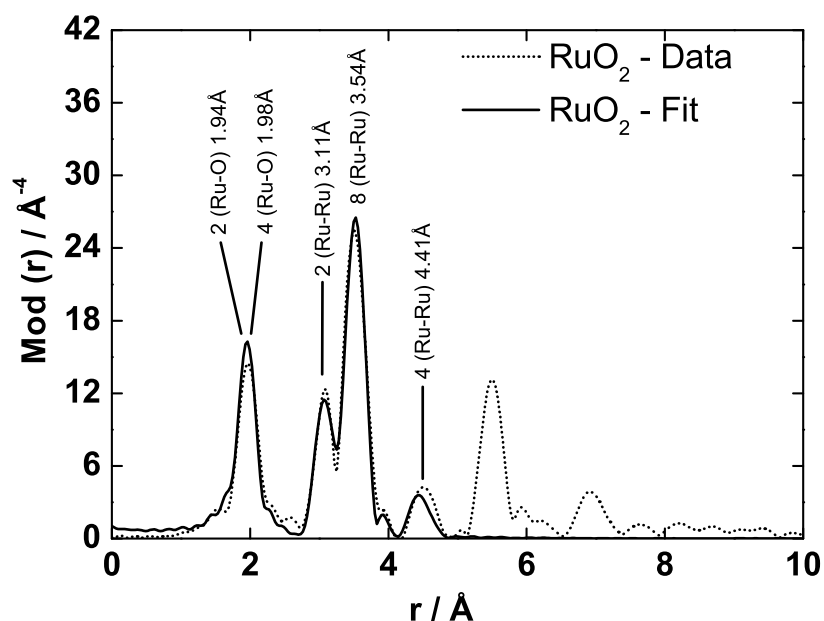


Figure 5.16.: Experimental Fourier transformed EXAFS spectrum  $\text{RuO}_2$  along with the fit to the data obtained from FEFF simulation. The type of atoms in a particular coordination shell, the interatomic distances and average coordination numbers according to the crystallographic data are indicated

paths at the Ru K edge were generated. Scattering contributions with relative significance greater than 15% of the maximum amplitude contributing path were chosen from the list of paths. Only single scattering contributions were included in the simulation of theoretical EXAFS signal  $\chi(k)$  which was then Fourier transformed in the interval ( $3 \leq k \leq 18$ )  $\text{\AA}^{-1}$ . Five largest amplitude paths from the rutile  $\text{RuO}_2$  were selected to fit nearest neighbor peaks below 6  $\text{\AA}$  in the experimental pseudo radial distribution function of anhydrous  $\text{RuO}_2$  reference.

Two single scattering Ru–O paths at 1.94  $\text{\AA}$  and 1.98  $\text{\AA}$  with path degeneracies of 2 and 4 corresponding to the octahedral arrangement, three Ru–Ru paths at 3.11  $\text{\AA}$ , 3.54  $\text{\AA}$  and 4.41  $\text{\AA}$  with path degeneracies of 2, 8 and 4 respectively were used to fit the FT EXAFS peaks. The fit to the experimental EXAFS spectrum of anhydrous  $\text{RuO}_2$  using the model of rutile  $\text{RuO}_2$  is given in figure 5.16. Ru–O at distances very close to Ru–Ru contributions were not considered in the fitting.

For the paths selected for inclusion in the structure model, mathematical expressions for the EXAFS parameters in equation 5.2 were defined as follows. The experimental EXAFS spectrum was fit in  $r$ -space interval of 1–6 Å by varying the change in path length ( $\Delta R_i$ ), mean square displacement of the bond length ( $\sigma^2$ ), and energy shift parameters of Ru and O ( $E_0$  shift) with the path degeneracies ( $N$ ) kept constant at crystallographic values.

The change in path length  $\Delta R_i$  was defined by an isotropic expansion/contraction term as ( $\alpha \times R_{\text{eff}}$ ) so that the equation 5.3 is modified into:

$$R_i = R_{\text{eff}i} + (\alpha \times R_{\text{eff}}). \quad (5.8)$$

By doing so, instead of using five individual parameters of  $\Delta R_i$  for five paths, a single  $\alpha$  term could be determined and applied to all path lengths included in the model, effectively reducing the number of variables. Because this approach assumes that adjustments to all path lengths (interatomic distances) in the structure vary in proportion to one another with  $\alpha$  being the proportionality constant, this approach is best suited for cubic structures with isotropic expansion or contraction.

Though the use of a single expansion parameter is valid only in the case of cubic systems it can also be extended to tetragonal systems as a simple approximation to the change in interatomic distances. Thermal expansion model for tetragonal system of RuO<sub>2</sub> was taken into consideration too, where the change in path length was correlated with the unit cell parameters  $a$ ,  $b$  and  $c$ .

From literature on thermal expansion coefficient of rutile type RuO<sub>2</sub> [85], it is known that while parameters  $a$  and  $b$  expand with increasing temperature,  $c$  decreases. Using the individual thermal expansion coefficients along  $a$ ,  $b$  and  $c$ ,  $\Delta R$  parameters of different paths were correlated thereby constructing a fitting model with correlated variables. However, it was found that fitting models built using only one expansion term or two expansion terms both resulted in very similar values for the fitted parameters. The EXAFS fit parameters obtained for the reference anhydrous RuO<sub>2</sub> sample are listed in table 5.4 and these parameters were used as initial guess for the catalyst samples whose local structure around ruthenium was found to be similar to anhydrous ruthenium oxide from the XANES analysis.

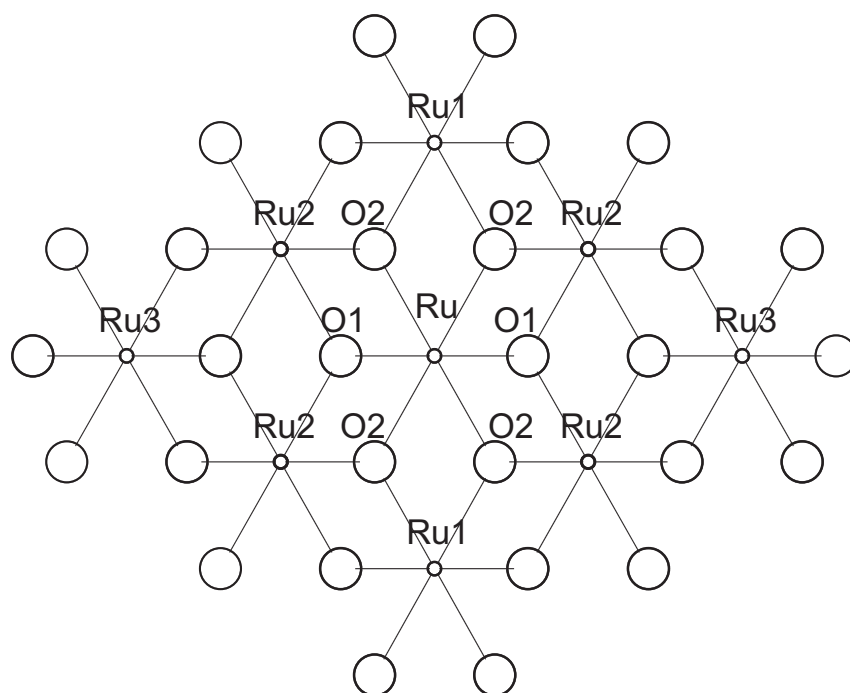


Figure 5.17.: EXAFS model representing the single scattering paths originating from the central Ru atom of rutile type  $\text{RuO}_2$

Sample	(Path) <sup>a</sup>	$(N \times S_0^2)^b$	$(R)^c$ Å	$(\sigma^2)^d$ Å <sup>2</sup>	$(E_0 \text{ shift})^e$ eV	$r$ -range Å	R-factor
Ref. 2	Ru↔O1	2	1.9458	0.0030	-5.91	1.0–6.0	0.189
	Ru↔O2	4	1.9902	0.0030	-5.91		
	Ru↔Ru1	2	3.1117	0.0025	-8.25		
	Ru↔Ru2	8	3.5463	0.0033	-8.25		
	Ru↔Ru3	4	4.5067	0.0056	-8.25		

Table 5.4.: EXAFS fit results of anhydrous  $\text{RuO}_2$  reference sample. <sup>a</sup>Path of absorber–backscatterer. <sup>b</sup> Path degeneracy or coordination number. <sup>c</sup> Distance between the absorber and the neighboring atom ( $R_i = R_{\text{eff}i} + \Delta R_i$ ). <sup>d</sup> Mean squared displacement of bond length. <sup>e</sup> Shift in energy scale reference

The model showing the numbering of atoms used to calculate the FEFF paths and subsequently used in obtaining the structure parameters from EXAFS analysis is given in figure 5.17.



### EXAFS analysis of Calcined samples Ru/Si1-c and Ru/Si2-c

Fourier transform peaks in the pseudo radial distribution function of samples Ru/Si1-c, Ru/Si2-c and RuO<sub>2</sub> all occur at identical distances from the central absorbing atom but with varied magnitudes. The magnitude of the peaks of calcined Ru samples in silicalite have reduced intensity compared to the reference with broadening of the signal due to shortened  $k$ -range of the samples. Significant FT peaks extending up to 6–7 Å are observed in these samples similar to the crystalline reference suggesting that ruthenium in silicalite has local geometry akin to anhydrous RuO<sub>2</sub>. Near-neighbor distances up to 6 Å was initially considered to check whether the similarity in the local structure of samples Ru/Si1-c and Ru/Si2-c (samples 3 and 4 in figure) with RuO<sub>2</sub> could be verified by fitting theoretical EXAFS data in this  $r$ -range. Three selected scenarios were considered each of which is probable in the real system.

The fitting procedure involved the usage of the same set of paths for the two samples considered and the reference as well. An obvious advantage of using multiple data set fitting is that consistency in the method of fitting can be maintained between different samples and as a result reliable interpretations or tendencies can be obtained. Due to this reason, although the EXAFS spectrum of the oxide reference was fitted using a more complex model earlier in section 5.2.3, the spectrum was once again fitted employing the same model used to fit the experimental spectra. As mentioned in section 5.2.3, the results of the previous fit were used as initial guess parameters during the iterations. The three scenarios considered and the details of each of the considered scenario is given next.

**Scenario 1** The aim of such a model scenario was to check whether the EXAFS spectra of the samples could be fit using a model based on crystalline RuO<sub>2</sub> with higher disorder alone without change in the path degeneracy or in other words average coordination numbers. The model considered for the fitting consists of one Ru–O path and two Ru–Ru paths at 1.986, 3.105 and 3.538 Å respectively with path degeneracy of 6, 2 and 8. The only iterated parameters in course of the fit were energy shift ( $E_0$ ) for Ru–O and Ru–Ru and the mean square displacement of bond length ( $\sigma^2$ ) of each path. The experimental spectra of samples and reference were fitted simultaneously by fixing common energy

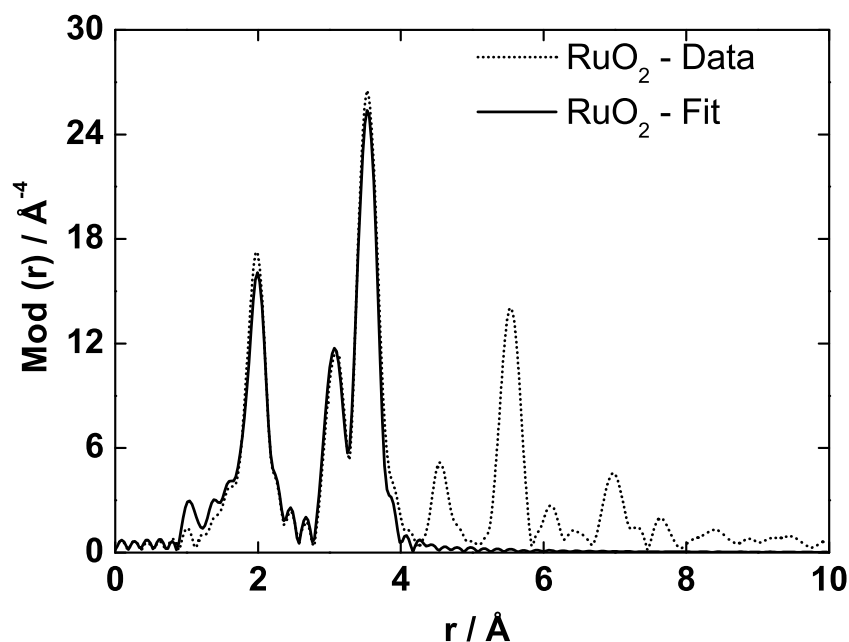


Figure 5.18.: Experimental EXAFS data of anhydrous  $\text{RuO}_2$  and the fitted EXAFS function using scenario 1

shift parameters but individual ( $\sigma^2$ ). The results of the fitting procedure employing scenario 1 for samples Ru/Si1-c, Ru/Si2-c and  $\text{RuO}_2$  are presented in table 5.5.

Reasonable fit to experimental spectra could be obtained for the considered samples and the  $\sigma^2$  values for all the paths in Ru/Si2-c are found to be higher than that obtained for anhydrous  $\text{RuO}_2$  which is found to further increase in Ru/Si1-c. Subsequently, another model scenario was also considered where the samples are assumed to have reduced coordination numbers due to smaller crystallite size but remain crystalline nevertheless like the reference material with a given  $\sigma^2$  value.

**Scenario 2** The next model considered for the fitting consists of one Ru–O path and two Ru–Ru paths at 1.986 Å, 3.105 Å and 3.538 Å respectively with  $\sigma^2$  values obtained in the previous fitting model for anhydrous  $\text{RuO}_2$  namely, 0.0040, 0.0025 and 0.0036 Å<sup>2</sup>. The only iterated parameters were the energy shift parameter ( $E_0$ ) and the degeneracy or coordination number of each path. The general fitting procedure adopted is the same as the previous case. The aim of such a model scenario was to check whether the EXAFS spectra of the samples could be fit using a model based on

Sample	(Path) <sup>a</sup>	(N × S <sub>0</sub> <sup>2</sup> ) <sup>b</sup>	(R) <sup>c</sup> Å	(σ <sup>2</sup> ) <sup>d</sup> Å <sup>2</sup>	(E <sub>0</sub> shift) <sup>e</sup> eV	r-range Å
Sam. 3	Ru↔O2	<b>6</b>	<b>1.986</b>	0.0058	5.31	1.0–6.0
	Ru↔Ru1	<b>2</b>	<b>3.105</b>	0.0031	-3.83	
	Ru↔Ru2	<b>8</b>	<b>3.538</b>	0.0043	-3.83	
Sam. 4	Ru↔O2	<b>6</b>	<b>1.986</b>	0.0072	5.31	1.0–6.0
	Ru↔Ru1	<b>2</b>	<b>3.105</b>	0.0047	-3.83	
	Ru↔Ru2	<b>8</b>	<b>3.538</b>	0.0056	-3.83	
Ref. 2	Ru↔O2	<b>6</b>	<b>1.986</b>	0.0040	5.31	1.0–6.0
	Ru↔Ru1	<b>2</b>	<b>3.105</b>	0.0025	-3.83	
	Ru↔Ru3	<b>8</b>	<b>3.538</b>	0.0036	-3.83	

Table 5.5.: EXAFS fit results of samples subjected to calcination post-treatment using the model of anhydrous RuO<sub>2</sub>. The parameters not iterated in course of the fit are given in bold and those parameters resulting from iteration are given in normal text. <sup>a</sup>Path of absorber–backscatterer. <sup>b</sup> Path degeneracy or coordination number. Value of (S<sub>0</sub><sup>2</sup>) was fixed at (S<sub>0</sub><sup>2</sup>)=1. <sup>c</sup> Distance between the absorber and the neighboring atom (R<sub>i</sub> = R<sub>effi</sub> + ΔR<sub>i</sub>). <sup>d</sup> Mean squared displacement of bond length. <sup>e</sup> Shift in energy scale reference

crystalline RuO<sub>2</sub> with reduced coordination number given in terms of degeneracy of each path. The results of the fitting procedure are presented in table 5.6.

In sample Ru/Si2-c, the average coordination number given in terms of (N × S<sub>0</sub><sup>2</sup>) when the value of (S<sub>0</sub><sup>2</sup>)=1, reduces from 6, 2 and 8 to 4.97, 1.95 and 5.88 by 17 %, 2.5 % and 26.5 % respectively. In sample Ru/Si2-c also the corresponding changes in are coordination number are from 6, 2 and 8 to 4.51, 1.58 and 4.52 by 24.8 %, 21 % and 43.5 % respectively. These changes are significant and they indicate considerable change in coordination numbers for higher Ru–Ru coordination shell and in turn to smaller crystallites inside the zeolite pores. However, like the increase in disorder observed in going from Ru/Si2-c to Ru/Si1-c in Scenario 1, coordination numbers are found to decrease on going from Ru/Si2-c to Ru/Si1-c.

Before attributing the change in coordination numbers as completely due to the small crystallites inside the zeolite pores, it is to be noted that the model considered here is based upon the assumption that the disorder of the two samples are identical to those

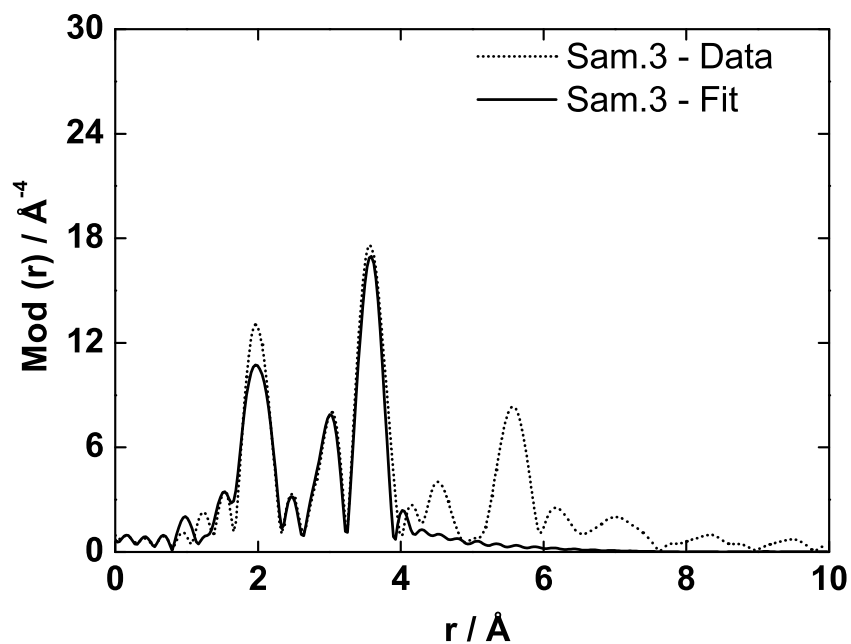


Figure 5.19.: Experimental EXAFS data of Sample 3 and the fitted EXAFS function using scenario 1

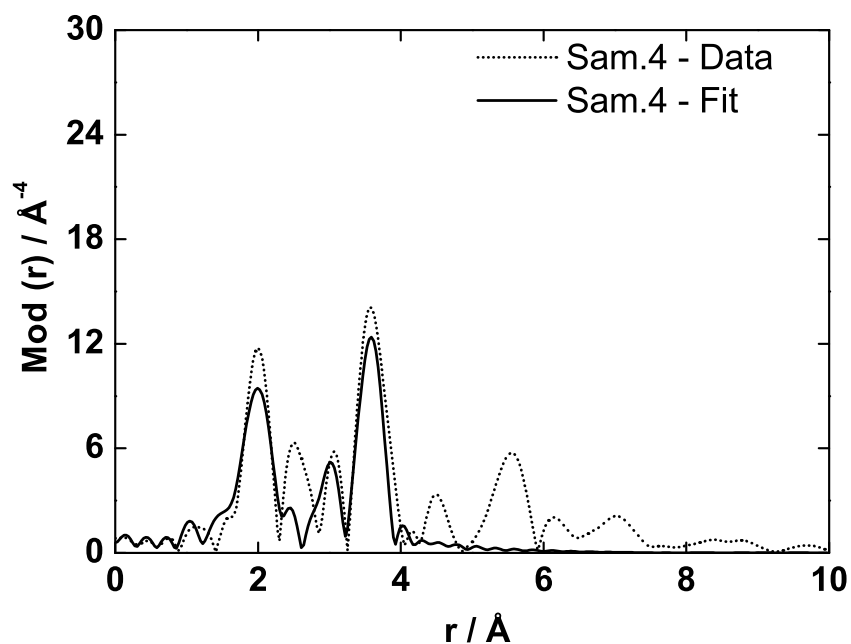


Figure 5.20.: Experimental EXAFS data of Sample 4 and the fitted EXAFS function using scenario 1

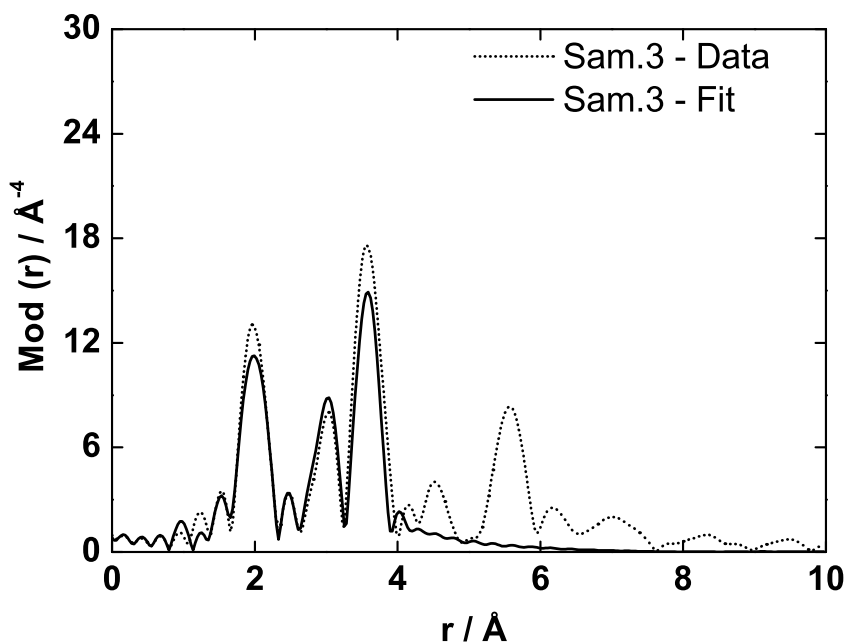


Figure 5.21.: Experimental EXAFS data of Sample 3 and the fitted EXAFS function using scenario 2

Sample	(Path) <sup>a</sup>	(N × S <sub>0</sub> <sup>2</sup> ) <sup>b</sup>	(R) <sup>c</sup> Å	(σ <sup>2</sup> ) <sup>d</sup> Å <sup>2</sup>	(E <sub>0</sub> shift) <sup>e</sup> eV	r-range Å
Sam. 3	Ru↔O2	5.0	<b>1.986</b>	<b>0.0040</b>	5.30	1.0–6.0
	Ru↔Ru1	1.9	<b>3.105</b>	<b>0.0025</b>	-3.79	
	Ru↔Ru2	5.9	<b>3.538</b>	<b>0.0036</b>	-3.79	
Sam. 4	Ru↔O2	4.5	<b>1.986</b>	<b>0.0040</b>	5.30	1.0–6.0
	Ru↔Ru1	1.6	<b>3.105</b>	<b>0.0025</b>	-3.79	
	Ru↔Ru2	4.5	<b>3.538</b>	<b>0.0036</b>	-3.79	

Table 5.6.: EXAFS fit results of samples subjected to calcination post-treatment using the model of rutile RuO<sub>2</sub>. <sup>a</sup>Path of absorber–backscatterer. <sup>b</sup> Path degeneracy or coordination number. Value of (S<sub>0</sub><sup>2</sup>) was fixed at (S<sub>0</sub><sup>2</sup>)=1. <sup>c</sup> Distance between the absorber and the neighboring atom (R<sub>i</sub> = R<sub>effi</sub> + ΔR<sub>i</sub>). <sup>d</sup> Mean squared displacement of bond length. <sup>e</sup> Shift in energy scale reference. The parameters not iterated in course of the fit are given in bold and those parameters resulting from iteration are given in normal text

obtained for the anhydrous RuO<sub>2</sub> reference. Moreover the value of ( $S_0^2$ ) was assumed and fixed at the value of 1 and not iterated and determined from reference compounds. Nevertheless, this assumption was consistently used for all the scenarios considered for the fit. In reality however, there is the possibility that both coordination numbers and disorder in distances change simultaneously so such a scenario was also considered.

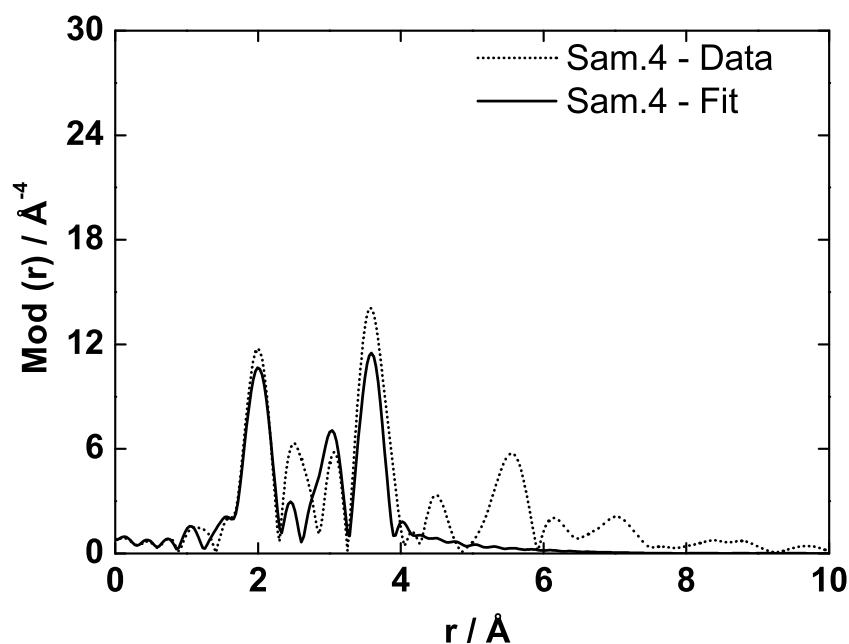


Figure 5.22.: Experimental EXAFS data of Sample 4 and the fitted EXAFS function using scenario 2

**Scenario 3** In this scenario, the coordination numbers were iterated and the different  $\sigma^2$  values obtained from scenario 1 for Ru/Si2-c and Ru/Si1-c were used in the fitting procedure. The results of the fitting procedure are presented in table 5.7.

The coordination numbers obtained for the first near-neighbor Ru shell in sample 3 and 4 are greater than 2 which is unreasonable while the average other coordination numbers are found to be closer to the crystalline reference.

In the three scenarios discussed so far, the first scenario where the silicalite loaded samples 3 and 4 exhibit local geometry similar to RuO<sub>2</sub> as evidenced earlier from the XANES region, seems most probable. Since the fit to the data could very well be obtained by only considering that the disorder in the samples change, while the coordination numbers remain the same, could be a possible interpretation to explain the reduced

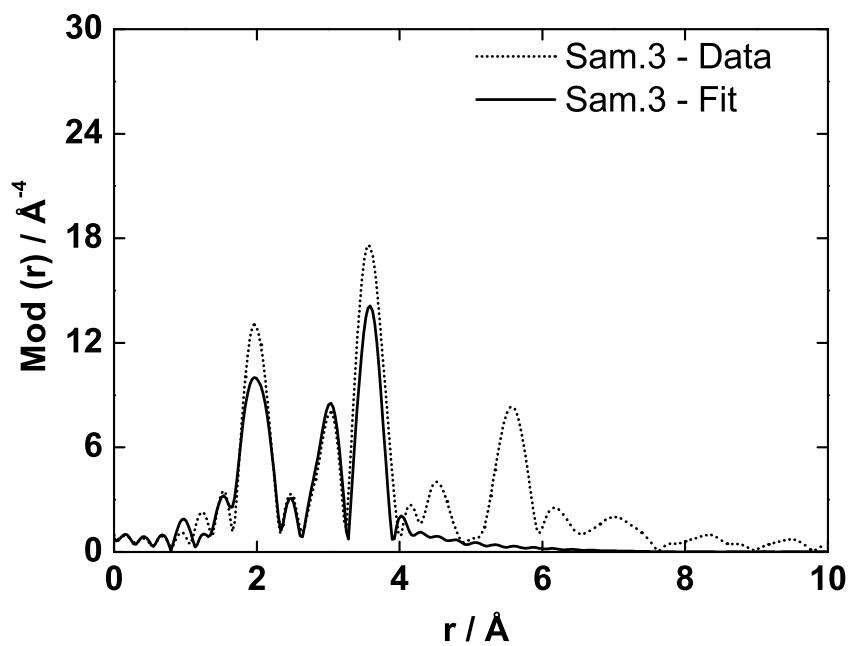


Figure 5.23.: Experimental EXAFS data of Sample 3 and the fitted EXAFS function using scenario 3

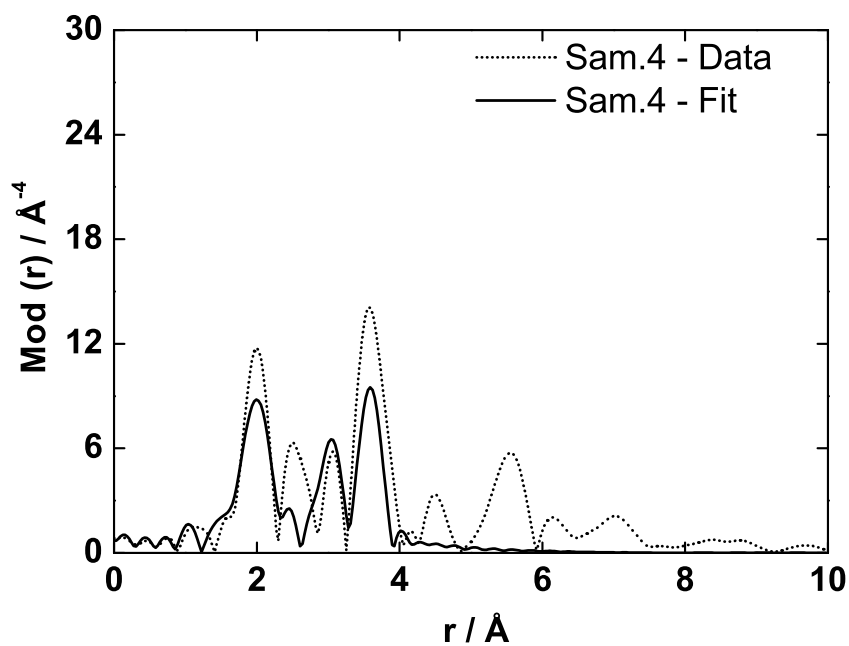


Figure 5.24.: Experimental EXAFS data of Sample 4 and the fitted EXAFS function using scenario 3

## 5. Ruthenium based catalysts in zeolite

Sample	(Path) <sup>a</sup>	(N × S <sub>0</sub> <sup>2</sup> ) <sup>b</sup>	(R) <sup>c</sup> Å	(σ <sup>2</sup> ) <sup>d</sup> Å <sup>2</sup>	(E <sub>0</sub> shift) <sup>e</sup> eV	r-range Å
Sam. 3	Ru↔O2	5.6	<b>1.986</b>	<b>0.0058</b>	5.28	1.0–6.0
	Ru↔Ru1	2.2	<b>3.105</b>	<b>0.0031</b>	-3.81	
	Ru↔Ru2	6.5	<b>3.538</b>	<b>0.0043</b>	-3.81	
Sam. 4	Ru↔O2	5.5	<b>1.986</b>	<b>0.0072</b>	5.28	1.0–6.0
	Ru↔Ru1	2.6	<b>3.105</b>	<b>0.0047</b>	-3.81	
	Ru↔Ru2	5.9	<b>3.538</b>	<b>0.0056</b>	-3.81	

Table 5.7.: EXAFS fit results of samples subjected to calcination post-treatment using the model of rutile RuO<sub>2</sub>. <sup>a</sup>Path of absorber–backscatterer. <sup>b</sup> Path degeneracy or coordination number. <sup>c</sup> Distance between the absorber and the neighboring atom ( $R_i = R_{\text{eff}i} + \Delta R_i$ ). <sup>d</sup> Mean squared displacement of bond length. <sup>e</sup> Shift in energy scale reference. The parameters not iterated in course of the fit are given in bold and those parameters resulting from iteration are given in normal text

FT magnitudes in samples 3 and 4 compared to anhydrous RuO<sub>2</sub>. In scenario 2 where the coordination numbers were iterated, the coordination numbers for the higher Ru–Ru shells were found to decrease to a greater extent compared to the Ru–O shell. Nevertheless, simultaneous decrease in coordination number pointing towards encapsulation inside the zeolite pores is also likely from scenario 3. Sample 4 exhibits additional FT peaks other than that found in the oxide reference and this points towards the possible mixture of more than one type of Ru species in the zeolites. Sample 4 also exhibits higher disorder for all the shells and is thus more complicated to arrive at one single structure picture.

### EXAFS analysis of Ru/ZSM-5-c (sample 9)

Ru/ZSM-5-c (sample 9) which completes the series of calcined samples, exhibits local structure different from that observed in silicalite samples Ru/Si2-c and Ru/Si1-c (samples 3 and 4). The main difference compared to samples 3 and 4 is the absence of coordination shells beyond 4 Å. Two FT peaks were attributed to the Ru near neighbors



Sample	(Path) <sup>a</sup>	(N × S <sub>0</sub> <sup>2</sup> ) <sup>b</sup>	(R) <sup>c</sup> Å	(σ <sup>2</sup> ) <sup>d</sup> Å <sup>2</sup>	(E <sub>0</sub> shift) <sup>e</sup> eV	r-range Å
Sam. 9	Ru↔O2	3.8	2.019	0.0034	9.27	1.5–4.0
	Ru↔Ru1	2.8	3.088	0.0067	-2.82	

Table 5.8.: EXAFS fit results of sample 9 using the first Ru–O and Ru–Ru paths of rutile RuO<sub>2</sub>. <sup>a</sup>Path of absorber–backscatterer. <sup>b</sup> Path degeneracy or coordination number. <sup>c</sup> Distance between the absorber and the neighboring atom ( $R_i = R_{\text{eff}i} + \Delta R_i$ ). <sup>d</sup> Mean squared displacement of bond length. <sup>e</sup> Shift in energy scale reference

in samples 3 and 4 resembling anhydrous RuO<sub>2</sub> whereas only one peak at around 3.1 Å is seen in Ru/ZSM-5-c (sample 9) similar to hydrous RuO<sub>2</sub>.

Based upon these preliminary observations, a model consisting of one Ru–O shell with coordination number of 6 at around 2 Å and one Ru–Ru shell with coordination number of 2 at around 3.1 Å was considered for the EXAFS fitting procedure. However, a minor structure feature at around 2.6–2.9 Å was observed in the experimental spectrum of the sample which has been attributed to Ru–O contribution in hydrous RuO<sub>2</sub> samples in literature [79]. This peak was not considered in the fitting procedure for the simple reason that it overlaps with the stronger Ru–Ru contribution at 3 Å and the fitting, results in unreasonable values for the disorder and artificially large coordination numbers. Moreover neglecting this peak in the fitting procedure still provides enough information to verify if a given structure model explains the experimental data. The parameters of the two shell model fitted to the experimental EXAFS spectrum of Ru/ZSM-5-c (sample 9) are listed in table 5.8 and the experimental data along with the fitted EXAFS function are given in figure 5.25.

Data reduction and the subsequent extraction of EXAFS oscillation from the measured absorption spectrum of Ru/ZSM-5-c was tedious and meticulous for two main reasons. First, the quality of the spectrum was inherently poor due to the low Ru content in the material providing only a short  $k$ -range of 2.5 to 12.5 Å<sup>-1</sup> for the Fourier transform. Second, complete separation of background from the structure signal was not possible without a strong cut-off in radial distance which resulted in artificially low coordination numbers for the first oxygen shell. Therefore it was decided to use the option available

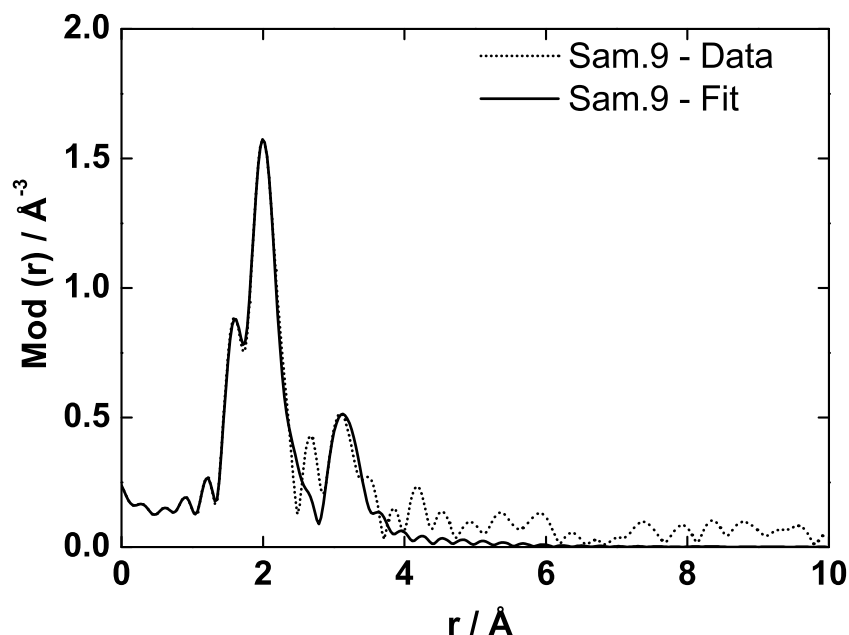


Figure 5.25.: Experimental EXAFS data of Sample 9 and the fitted EXAFS function using a two shell model of crystalline RuO<sub>2</sub>

in IFEFFIT to simultaneously fit the signal to a model and a background spline for the rest of the signal in the low  $r$  range. Good match of the experimental data to the theoretically fitted function in the low  $r$  region below 1.5 Å is a direct result of employing this option and in fact this region was not considered in the fit. Non-zero value for the FT magnitude at the origin is also an artificial effect due to the fitted background and is amplified by the scale of the y-axis and does not point to poor background subtraction.

Oxygen shell coordination number of 3.8 at a distance of 2 Å coincides with the values reported for hydrous RuO<sub>2</sub> by McKeown *et al.* [79] and the Ru–Ru average coordination number of 2.8 at 3.1 Å suggests that Ru–Ru interactions does not extent beyond a first coordination shell. From the observed distances of Ru–O and Ru–Ru in the fitted model, the Ru/ZSM-5-c sample can be described with the model of hydrous RuO<sub>2</sub> proposed by Zhan *et al.* [60] for ruthenium catalysts in Y-type zeolites where chains of Ru–O entities extend along the pores of the zeolite with possible Ru–O–Si interactions. In summary, from the EXAFS analysis the presence of non-agglomerated Ru species in the zeolite support with local coordination similar to hydrous RuO<sub>2</sub> is evidenced even after calcination step in sample 9.

## EXAFS analysis of Ru/NaA1 and Ru/NaA2 (samples 6 and 7)

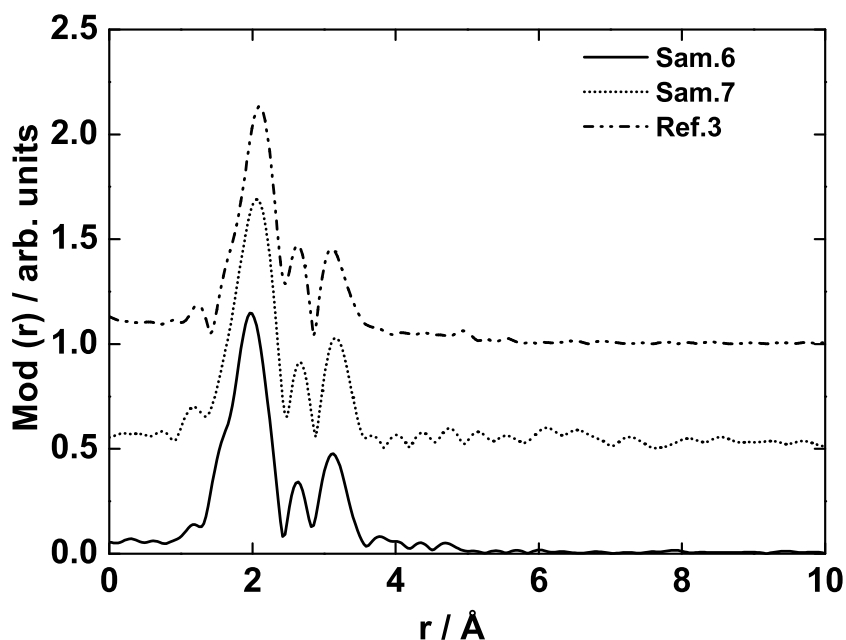


Figure 5.26.: Comparison of experimental EXAFS spectra of Ru/NaA1 and Ru/NaA2 (samples 6 and 7) along with hydrous RuO<sub>2</sub> reference

Figure 5.26 shows the pseudo radial distribution functions obtained by Fourier transform of the  $k^2$ -weighted EXAFS signal of ruthenium in NaA (sample 6 and 7) along with the hydrous RuO<sub>2</sub> reference 3. At first, strong similarity of the reference spectra used in this study to the RuO<sub>2</sub>·2.32H<sub>2</sub>O reported in literature [79] is noted and this observed similarity fulfills the need to use authentic reference compounds while discussing the structure aspects of complex oxides. Second, FT features of the Ru/NaA samples are near identical to the reference substance which has been systematically investigated and whose structure has been proposed to be a two-dimensional structure of independent chains made of RuO<sub>6</sub> edge connected octahedra atoms as illustrated in figure 5.27 [60].

FT EXAFS spectra of the samples and the reference also show a peak at a distance of roughly 2.6 Å which in the case of hydrous RuO<sub>2</sub> in literature [79] was assigned to the Ru–OH<sub>2</sub> or the Ru–OH bond. The authors had reasoned that the longer Ru–O distance of 2.6 Å could indicate a strong interaction of the Ru species with the zeolite framework through Ru–O–Si<sub>zeo</sub> type interactions either through terminal oxygen atoms or bridged

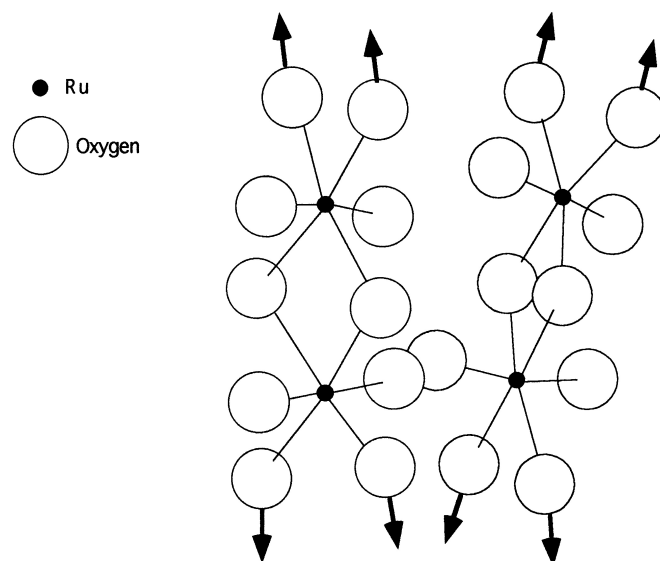


Figure 5.27.: Model of two-dimensional  $\text{RuO}_2 \cdot 2.32\text{H}_2\text{O}$  with disordered  $\text{RuO}_6$  edge connected in twisted unconnected chains

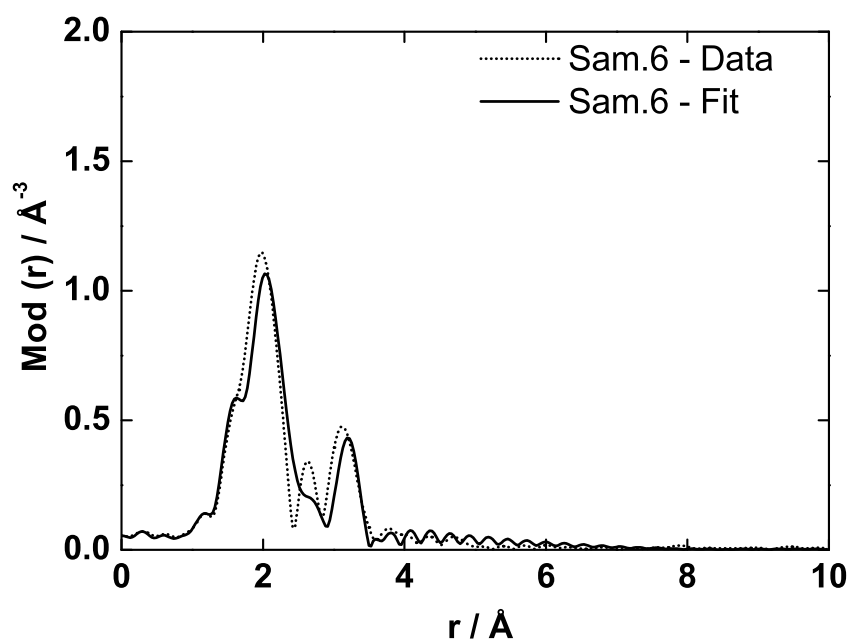


Figure 5.28.: Experimental EXAFS data of Sample 6 and the fitted EXAFS function using a two-shell model of crystalline  $\text{RuO}_2$

oxygen atoms. However, to unambiguously answer the question if Ru–O–Si/Al type interactions exist in Ru/NaA1 and Ru/NaA2 (sample 6 and 7), direct evidence in the

Sample	(Path) <sup>a</sup>	$(N \times S_0^2)^b$	(r) <sup>c</sup> Å	$(\sigma^2)^d$ Å <sup>2</sup>	$(E_0)^e$ eV	r-range Å
Sam. 6	Ru↔O2	4.6	2.080	0.0069	9.27	1.5–4.0
	Ru↔Ru1	1.4	3.124	0.0048	-2.82	
Sam. 7	Ru↔O2	3.4	2.019	0.0033	9.27	1.5–4.0
	Ru↔Ru1	3.3	3.103	0.0082	-2.82	
Ref. 3	Ru↔O2	4.01	2.024	0.0070	9.27	1.5–4.5
	Ru↔Ru1	2.90	3.093	<b>0.0082</b>	-2.82	

Table 5.9.: EXAFS fit results of samples without calcination post-treatment, using the two shell model of crystalline RuO<sub>2</sub>. <sup>a</sup>Path of absorber–backscatterer. <sup>b</sup> Path degeneracy or coordination number. <sup>c</sup> Distance between the absorber and the neighboring atom ( $R_i = R_{\text{eff}i} + \Delta R_i$ ). <sup>d</sup> Mean squared displacement of bond length. <sup>e</sup> Shift in energy scale reference. The parameters not iterated in course of the fit are given in bold and those parameters resulting from iteration are given in normal text

form of Ru–Si/Al shell in the FT EXAFS spectra could not be seen. There is no conclusive proof as to either such interactions exist in samples 6 and 7 but it cannot be completely ruled out. The in situ XANES spectra recorded during the reduction of sample 7 under mild conditions obliquely suggest that the interaction of ruthenium in sample 7 with the zeolite is not very strong while similar studies for sample 6 have not been performed.

The experimental Fourier transformed EXAFS spectra and the fit for samples Ru/NaA1 and Ru/NaA2 are given in figure 5.28 and figure 5.29 respectively. The corresponding EXAFS results presented in table 5.9 indicate that the ruthenium species present in the NaA zeolite (samples 6 and 7) are disordered RuO<sub>2</sub> most likely with a chain type structure. The prominent FT peak in the EXAFS spectra of samples 6 and 7 correspond to the Ru–O contribution at an interatomic distance of 2.02 Å which matches with the distance obtained by analyzing the reference of hydrous RuO<sub>2</sub>.

The fit to the experimental spectrum of hydrous RuO<sub>2</sub> is given in figure 5.30. Similar distances of 3.12 and 3.10 Å for Ru–Ru contribution in the samples 6 and 7 were also obtained from EXAFS analysis which was only very slightly higher than the value of 3.09 Å obtained in reference 3. The disorder in the distance between Ru–O in samples 6 is 0.007 Å which is same as that observed for the reference 3 but the value obtained

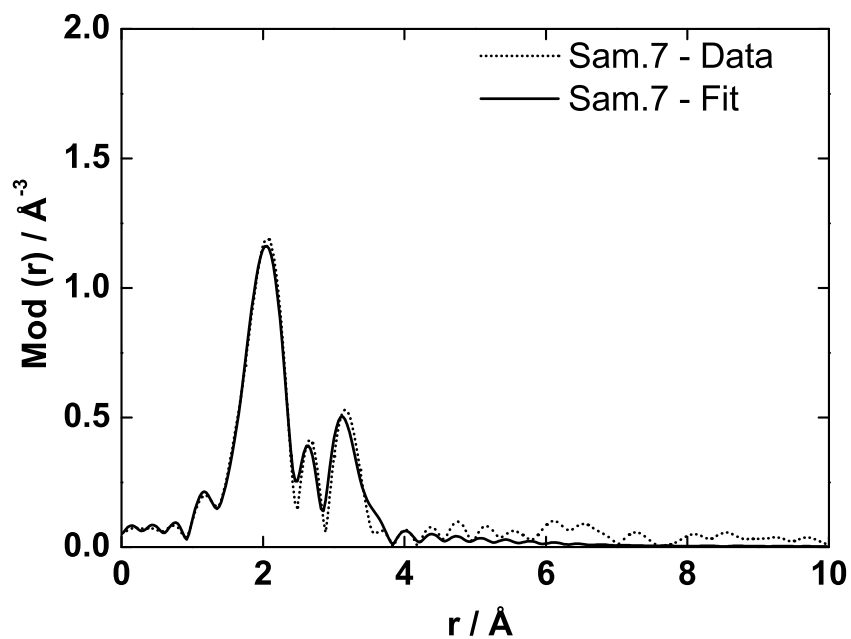


Figure 5.29.: Experimental EXAFS data of Sample 7 and the fitted EXAFS function using a two-shell model of crystalline RuO<sub>2</sub>

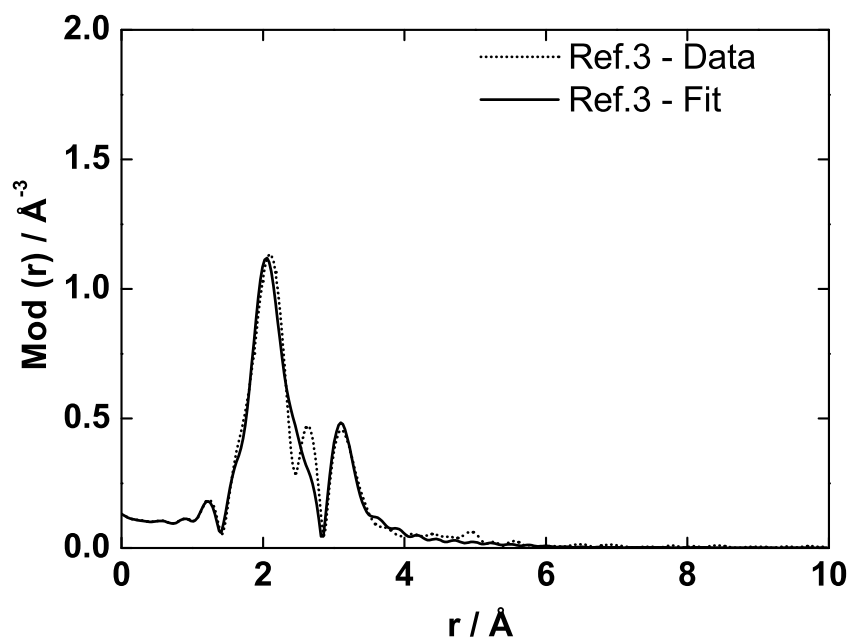


Figure 5.30.: Experimental EXAFS data of reference 3, hydrous RuO<sub>2</sub> and the fitted EXAFS function using a two-shell model of RuO<sub>2</sub>

for sample 7 is 0.003 Å which is lower. In the case of disorder in the Ru–Ru distance, however, no trends could be observed.

The error in the determination of coordination numbers are significantly higher than that obtained for the interatomic distances, nevertheless some indications about the difference in local structure around Ru in samples 6 and 7 were obtained from the Ru–Ru shell. The Ru–Ru shell average coordination number of 1.4 is obtained for sample 6 whereas a value of 3.3 is obtained for sample 7. If all the ruthenium species form a chain like structure, an average value of 2 is expected for the average coordination number and the values that deviate from 2 indicate the presence of more than one type of species. The EXAFS average coordination numbers of 1.4 and 3.3 could suggest that Ru exists predominantly in chain like structures with other phases coexisting as a minor fraction. EXAFS results of samples 6 and 7 which show that the local environment of Ru in the NaA zeolites resembles hydrous RuO<sub>2</sub>, confirm the results derived from the XANES investigation.

To summarize the results on the investigation of Ru catalysts in zeolites NaA, ZSM-5 and Silicalite-1, FEFF based EXAFS analysis revealed the presence of local structure similar to anhydrous RuO<sub>2</sub> in samples subjected to calcination post treatment and presence of local structure similar to hydrous RuO<sub>2</sub> in NaA zeolite supported catalysts. Edge connected distorted octahedra of RuO<sub>6</sub> in a chain like structure was elucidated from the EXAFS analysis of Ru/NaA sample. For all the investigated samples, results from EXAFS analysis were supported by the findings from the XANES spectra and weighting fraction LC-XANES analysis.





## 6. Summary

In this dissertation, XAS (X-ray absorption spectroscopy) was employed as a fundamental spectroscopic method to ascertain the physical and electronic structure of metal and metal oxides dispersed in inorganic matrices. Metals and metal oxides dispersed in inorganic matrices like aluminosilicates (zeolites) are extensively used as catalysts for several industrially relevant chemical transformations. Metals like platinum, gold and metal oxides like ruthenium dioxide incorporated in zeolites are difficult to structurally characterize using diffraction methods due to the absence of long range order in well dispersed materials. Small particles of metal or metal oxide are also very sensitive to gases and either special care in handling or custom designed in situ cells are required to perform catalyst preparation and XAS experiments.

Catalyst characterization is extensively carried out using laboratory spectroscopic methods, however synchrotron radiation based techniques are necessary to gather direct structure information complementary to the lab techniques. Certain porous materials with loaded metal or metal oxides can only be completely characterized using the powerful yet expensive synchrotron radiation techniques and XAS is one such technique which has been at the forefront to investigate catalysts under operating conditions.

In the first part of the thesis, platinum clusters were prepared in NaY zeolite in an in situ XAS cell and structurally characterized as nanometer sized metal clusters with approximately 13 atoms on an average. These highly dispersed Pt clusters in NaY zeolite were found to be very reactive towards carbon monoxide (CO) and the degradation of platinum clusters upon CO interaction was revealed by detailed EXAFS (Extended x-ray absorption fine structure) analysis.

Analysis of Pt<sub>13</sub>H<sub>m</sub>/NaY after CO adsorption revealed a decrease in Pt–Pt average distance to 2.69 Å from 2.77 Å together with a decrease in the Pt–Pt average coordination number from 5.8 to 0.9. Two Pt–C contributions, one at 1.95 Å and the next at 2.14 Å

## 6. Summary

---

were obtained with average coordination number of 0.8 and 1.7 respectively. The short Pt–C distance of 1.95 Å is similar to the Pt–C distance observed in well characterized compounds like Pt<sub>3</sub>(CO)<sub>6</sub> where CO molecules are coordinated to Pt in a linear and bridge like fashion. With further evidence from infra red (IR) spectroscopy results, it was inferred that one linear and two bridged CO molecules coordinate to Pt.

During CO interaction with hydrogen reduced Pt clusters, Quick-XAS measurements were performed to study the time dependent changes of the Pt L<sub>3</sub> edge XANES (X-ray absorption near edge structure) spectrum. In order to quantify the time dependent change of the white line, two methods were used. In the first method, the area under the curves was directly determined using numerical integration. In the second method, the XANES spectra were subjected to curve fitting analysis and fitted as a superposition of an arctan function and pseudo-Voigt function. The area under the pseudo-Voigt function was determined using numerical integration by employing the QAG algorithm (Gauss-Kronrod 61 point rule) from the GNU scientific library.

The area under the pseudo-Voigt function plotted against time showed a gradual decrease in area under the curve with time in two regimes. Until 193 s after the introduction of CO, a linear fit to the data with slope of  $13.00 \pm 0.03 \text{ eV s}^{-1}$  and from 193 s up to 725 s, a linear fit with slope of  $12.74 \pm 0.01 \text{ eV s}^{-1}$  was obtained and the reaction kinetics of CO interaction was found to be of zero order.

From the L<sub>2</sub> and L<sub>3</sub> edge XANES spectra of Pt catalysts in NaY zeolite, fractional change in the *d*-electron occupancy in Pt was quantitatively obtained by carrying out the following steps in sequence:

- The XAS spectra of the Pt metal foil measured together with each sample were aligned with each other.
- The first point of zero-crossing of the second derivative of the Pt metal spectra was assigned to the tabulated edge energy of Pt and the corresponding XAS spectra of the samples were energy calibrated.
- After background removal from the pre-edge region, normalization to unit edge step was carried out.
- The inflection points of the XAS spectra of the samples and the metal foil were determined from their corresponding first derivative plots.

- 
- The energy scale (x-axis scale) was shifted using the expression  $(E-E_i)$ , where  $E_i$  is the first inflection point of each sample. After the shift to the energy scale, the  $L_2$  and  $L_3$  edge spectrum of each sample could be overlaid.
  - Overlap in the EXAFS oscillations above 40 eV for the  $L_2$  and  $L_3$  was verified in the overlaid spectra
  - The area under the curves for each of the investigated sample was determined using Simpson's rule in the range -30 eV to +30 eV.

In the second part of the thesis, multi-resolution wavelet analysis of EXAFS spectra of an Au-Ag alloy model system was carried out using Morlet wavelet. Model EXAFS signals, first with both Ag-Ag and Ag-Au near neighbors and next with only Ag-Ag near neighbors were generated using EXCURV98 package. These two signals were subjected to wavelet transform in order to check if it is possible to distinguish between Ag-Au and Ag-Ag backscatterers located at equal distances. It was evidenced that the  $k$ -weighting of the model signal has a pronounced effect on the resolution achievable using the wavelet transform. A minimal  $k$ -weighting of  $k^1$  applied to the model signal is found to be appropriate to distinguish between the two different backscatterers in the wavelet transform. Limitations in the  $k$ - $r$  space resolution achievable using Morlet wavelets when the constituent model signals were from similar type of backscatterers were ascertained to arise from the bimodal nature of the chosen wavelet. A wide range of Morlet wavelet parameters  $\kappa$  and  $\sigma$  available for the transform provide multiple resolution in  $k$ - $r$  space for the analysis of the EXAFS signal and the effect of different set of parameters in providing variable resolution was demonstrated using a model signal.

In the EXAFS analysis of experimental data in the first two parts of the thesis, single scattering analysis using EXCURV98 program was used. However, to describe the local structure in oxide materials more accurately, complex structure models of well characterized reference compounds must be constructed. For this purpose, in the next part of the thesis, program FEFF which is more suitable for EXAFS analysis with multiple scattering, multiple data set fitting and multiple  $k$ -weighting with constraints was employed. With FEFF it is possible to generate all possible scattering paths corresponding to a model compound from its crystallographic data at a given edge. From this list, suitable theoretical EXAFS models of reference compounds can be constructed and fitted to the experimental EXAFS data by iteration of different parameters in the EXAFS equa-

## 6. Summary

---

tion. Therefore FEFF program was used in the analysis of EXAFS spectra of ruthenium containing materials and the results are summarized in the following paragraphs.

In the third part of the thesis, ruthenium loaded in silicalite-1, NaA and ZSM-5 zeolites together with anhydrous  $\text{RuO}_2$  and hydrous  $\text{RuO}_2$  reference compounds were investigated with XAS. XANES results confirmed that the oxidation state of ruthenium in all the samples is +IV similar to  $\text{RuO}_2$ . EXAFS analysis using FEFF methodology was employed to model the theoretical EXAFS spectra of anhydrous and hydrous  $\text{RuO}_2$ . The experimental EXAFS spectra of ruthenium incorporated in NaA, Na-ZSM-5 and Silicalite-1 were fitted with the model of anhydrous or hydrous  $\text{RuO}_2$ .

In the EXAFS investigation of ruthenium in silicalite-1 after calcination post treatment, local geometry of Ru similar to anhydrous  $\text{RuO}_2$  with an increased disorder in distance relative to anhydrous  $\text{RuO}_2$  was determined. Simultaneous decrease in the coordination number of higher Ru–Ru shells, more pronounced than the decrease in the Ru–O shell coordination number, indicated the encapsulation of the oxide clusters in the zeolite cavities.

Investigation of the structure of Ru/ZSM-5 after calcination was carried out with EXAFS analysis using the model of hydrous  $\text{RuO}_2$ . The presence of non-agglomerated Ru species in the zeolite support with local coordination geometry similar to hydrous  $\text{RuO}_2$  was evidenced. For Ru/NaA samples, EXAFS as well as in situ XANES investigations were carried out. From temperature programmed reduction of Ru/NaA zeolite it was found that temperature condition ( $\approx 120^\circ\text{C}$ ) milder than that required to reduce pure ruthenium oxide was sufficient to completely reduce Ru in oxidation state of +IV to Ru metal. The change in the oxidation state of Ru with time was quantified by linear combination XANES analysis using reference compounds. EXAFS results indicated that ruthenium species present in NaA zeolite is disordered  $\text{RuO}_2$  most likely with chain type structure of connected  $\text{RuO}_6$  octahedra.

Changes in the oxidation state of metal and metal oxide catalysts during chemical reactions and during oxidative or reductive pre-treatments can be recorded with the help of specially designed in situ XAS cells. Further, change in the structure of small particles of metal or metal oxide due to external atmosphere or other gases can be avoided when the preparation of these particles is carried out using an in situ set up prior to XAS measurement. By considering these two important factors, for the structure characterization and for recording changes in the oxidation state during chemical reaction of the

---

catalyst with gases, an in situ XAS catalytic reactor cell made of quartz and working in fixed bed conditions was designed.

Inconel alloy heating block, three-part fused thin walled quartz tube catalytic reactor, ultra-tight gas fittings to connect quartz to a metal tube for inlet and outlet gases were the essential components of the set up. This set up was tested by heating up to 350 °C with a coupled mass spectrometer at HASYLAB at Hamburg and was used to measure XAS spectra of reference materials under high temperature and gas flow at ANKA, Karlsruhe. Temperature dependent XAS spectra of ZrO<sub>2</sub> and RuO<sub>2</sub> reference compounds were measured and EXAFS spectra of these compounds were analyzed. Gas mixing and supply system with several mass flow controllers was also designed to provide a mixture of gases to the reactor along with the temperature control and measurement system. The compact design and good heat isolation, adjustable x-y axis table mount with micrometer precision provided quick installation and focusing of the synchrotron x-ray beam on to the sample inside the quartz tube.



## 7. Zusammenfassung

In dieser Dissertation wurde die Röntgenabsorptionsspektroskopie (engl.: X-ray Absorption Spectroscopy = XAS) verwendet, um die chemische und elektronische Struktur von Metallen und Metalloxiden, die fein verteilt in verschiedenen anorganischen Trägern vorliegen, aufzuklären. Metalle und Metalloxide, die fein verteilt in anorganischen Trägern wie z. B. Aluminosilikaten (Zeolithe) vorliegen, werden als Katalysatoren bei verschiedenen, industriell relevanten chemischen Umsetzungen eingesetzt. Metalle (z. B. Platin oder Gold) und Metalloxide (z. B. Rutheniumdioxid), die in Zeolithen enthalten sind, können nicht einfach mit Hilfe der Röntgenbeugung strukturell charakterisiert werden. Dies liegt daran, dass aufgrund der feinen Verteilung keine Fernordnung vorliegt. Kleine Metall- oder Metalloxydpartikel sind außerdem sehr empfindlich gegenüber Gasen. Deshalb müssen entsprechende Katalysatorproben bei der Präparation und bei XAS Experimenten unter Berücksichtigung bestimmter Vorsichtsmaßnahmen (z. B. Glove box) gehandhabt werden. Alternativ können hierfür auch speziell entwickelte in situ Zellen eingesetzt werden.

Die Charakterisierung von Katalysatoren erfolgt hauptsächlich mit Hilfe von labor-spektroskopischen Methoden. Techniken auf der Basis von Synchrotronstrahlung sind aber zusätzlich notwendig, um Strukturinformationen zu erhalten, die komplementär zu den Daten der Labormethoden sind. Bestimmte poröse Materialien, die mit Metallen oder Metalloxiden beladen sind, können nur mit Hilfe der leistungsfähigen, aber teuren Synchrotronstrahlungsmethoden vollständig charakterisiert werden. Eine dieser Methoden ist die XAS-Spektroskopie, die zur Untersuchung von Katalysatoren unter Betriebsbedingungen eingesetzt wird.

Im ersten Teil der Arbeit wurden Platincluster in einem NaY Zeolith mit Hilfe einer in situ XAS Zelle präpariert. Die strukturelle Charakterisierung ergab, dass die nanometergroßen Metallcluster durchschnittlich aus etwa 13 Atomen bestehen. Es wurde festgestellt, dass diese fein verteilten Platincluster sehr reaktiv gegenüber Kohlenstoff-

monoxid (CO) sind. Eine detaillierte EXAFS-Analyse (Extended X-ray Absorption Fine Structure) zeigte, dass die Platincluster durch Kontakt mit CO zersetzt werden.

Die Untersuchung von Pt<sub>13</sub>H<sub>m</sub>/NaY nach CO Adsorption ergab eine Abnahme des mittleren Pt–Pt Abstands von 2.77 Å auf 2.69 Å. Gleichzeitig nahm die mittlere Pt–Pt Koordinationszahl von 5.8 auf 0.9 ab. Die Auswertung lieferte zwei Pt–C Schalen, eine bei 1.95 Å und eine bei 2.14 Å, mit mittleren Koordinationszahlen von 0.8 bzw. 1.7. Der kurze Pt–C Abstand von 1.95 Å ist ähnlich zu den Pt–C Abständen in bekannten, gut charakterisierten Verbindungen wie z. B. Pt<sub>3</sub>(CO)<sub>6</sub>, in denen CO Moleküle linear oder verbrückend an die Platinatome koordiniert sind. Anhand weiterer Ergebnisse aus der Infrarotspektroskopie zeigte sich, dass ein lineares und zwei verbrückende CO Moleküle an das Platin koordinieren.

Während der Wechselwirkung von CO mit Wasserstoff reduzierten Platinclustern wurden Quick-XAS Messungen durchgeführt, um zeitabhängig die Änderungen des Pt L<sub>3</sub> Kanten XANES-Spektrums (XANES = X-ray Absorption Near Edge Structure) zu untersuchen. Um die zeitabhängigen Änderungen der White-Line quantifizieren zu können, wurden zwei Methoden verwendet. Bei der ersten Methode wurde die Fläche unter den Kurven direkt durch numerische Integration ermittelt. Bei der zweiten Methode wurden die XANES-Spektren einer Curve-Fitting-Analyse unterworfen. Dabei wurde eine Überlagerung einer arctan Funktion und einer pseudo-Voigt Funktion angepasst. Die Fläche unter der pseudo-Voigt Funktion wurde durch numerische Integration gemäß des QAG-Algorithmus (Gauss-Kronrod 61 point rule) aus der GNU scientific library ermittelt.

Das Schaubild, in dem die Fläche unter der pseudo-Voigt Funktion gegen die Zeit aufgetragen wurde, zeigte zwei Bereiche, in denen die Fläche mit unterschiedlichen Steigungen allmählich abnimmt. Bis 193 s nach Zugabe von CO konnte eine Gerade mit einer Steigung von  $13.00 \pm 0.03 \text{ eV s}^{-1}$  an die Datenpunkte angepasst werden. Im zweiten Bereich, 193 s bis 725 s, wurde eine Gerade mit einer Steigung von  $12.74 \pm 0.01 \text{ eV s}^{-1}$  angepasst. Für die Reaktionskinetik der CO Wechselwirkung ergab sich eine Reaktion nullter Ordnung.

Aus den L<sub>2</sub> und L<sub>3</sub> Kanten XANES-Spektren der Pt Katalysatoren in NaY Zeolithen konnte eine geringe Veränderung der Besetzung der Pt d-Orbitale quantitativ ermittelt werden. Hierzu wurden die folgenden Schritte nacheinander durchgeführt:



- 
- Die XANES-Spektren der Pt-Metallfolie, die mit jeder Probe zusammen gemessen wurden, wurden so verschoben, dass sie möglichst genau übereinander lagen.
  - Die erste Nullstelle der zweiten Ableitung der Pt-Metall-Spektren wurde auf den tabellierten Wert der Kantenenergie von Pt gesetzt. Auch die entsprechenden XAS-Spektren der Proben wurden energiekalibriert.
  - Nach der Untergrundkorrektur anhand des Vorkantenbereichs wurde das Spektrum auf einen Kantensprung von 1.0 normiert.
  - In den XAS-Spektren der Proben und der Metallfolie wurden die Wendepunkte aus den ersten Ableitungen ermittelt.
  - Die Energieskala (x-Achse) wurde anhand des Ausdrucks  $(E-E_i)$  verschoben. Hierbei ist  $E_i$  der erste Wendepunkt der jeweiligen Probe. Nach dem Verschieben der Energieskala konnten die  $L_2$  und  $L_3$  Kanten Spektren jeder einzelnen Probe übereinander gelegt werden.
  - Es wurde verifiziert, ob die EXAFS Oszillationen der  $L_2$  und  $L_3$  Kanten Spektren oberhalb von 40 eV überlappen.
  - Die Flächen unter den Kurven der verschiedenen untersuchten Proben wurden anhand von Simpson's Regel im Bereich von -30 eV bis +30 eV ermittelt.

Im zweiten Teil der Arbeit wurde eine Multi-Resolution-Wavelet-Analyse der EXAFS-Spektren eines Au–Ag Legierungs-Modellsystems unter Verwendung eines Morlet Wavelets durchgeführt. Modell-EXAFS-Signale wurden mit Hilfe des EXCURV98 Pakets generiert-zuerst mit Ag–Ag und Ag–Au Absorber–Rückstreuer-Paaren und anschließend nur mit Ag–Ag Paaren. Diese beiden Signale wurden einer Wavelet-Transformation unterworfen, um zu überprüfen, ob Ag–Au und Ag–Ag Rückstreuer, die sich im gleichen Abstand vom Absorberatom befinden, unterschieden werden können. Es zeigte sich, dass die  $k$ -Wichtung des Modell-Signals einen starken Einfluss auf die Auflösung hat, die mit Hilfe der Wavelet-Transformation erreicht werden kann. Eine minimale  $k$ -Wichtung von  $k^1$  scheint geeignet zu sein, um die zwei verschiedenen Rückstreuer in der Wavelet-Transformation unterscheiden zu können. Die  $k$ - $r$  Auflösung, die mit Morlet-Wavelets erreicht werden kann, ist aber begrenzt, wenn die einzelnen Signale von sehr ähnlichen Rückstreuern stammen. Dies liegt an dem bimodalen Charakter des gewählten Wavelets. Eine große Anzahl von Morlet-Wavelet-Parametern  $\kappa$  und  $\sigma$  liefern verschiedene Auflösungen im  $k$ - $r$  Raum für die Analyse von EXAFS-Signalen. Der Einfluss

unterschiedlicher Parametersätze und die dadurch erreichbaren variablen Auflösungen wurden an einem Modell-Signal gezeigt.

In den ersten beiden Teilen dieser Arbeit wurde bei den EXAFS-Auswertungen mit dem Programm EXCURV98 nur die Einfachstreuung berücksichtigt. Um aber die lokale Struktur von Oxidmaterialien genauer beschreiben zu können, müssen komplexe Strukturmodelle gut charakterisierter Referenzverbindungen konstruiert werden. Zu diesem Zweck wurde im nächsten Teil der Arbeit das Programm FEFF eingesetzt. Dieses Programm ist geeigneter für die EXAFS-Analyse, wenn Mehrfachstreuung oder verschiedene  $k$ -Wichtungen mit Constraints verwendet werden sollen. Außerdem erlaubt es die gleichzeitige Anpassung von verschiedenen Datensätzen. Mit FEFF ist es möglich, für eine bestimmte Absorptionskante alle möglichen Streupfade einer Modellverbindung aus den zugehörigen kristallographischen Daten zu generieren. Mit dieser Pfadliste können geeignete theoretische EXAFS-Modelle von Referenzverbindungen konstruiert und an experimentelle EXAFS-Daten durch Iteration verschiedener Parameter angepasst werden. Deshalb wurde FEFF bei der EXAFS-Auswertung von rutheniumhaltigen Materialien eingesetzt. Die Ergebnisse sind in den folgenden Abschnitten zusammengefasst.

Im dritten Teil dieser Arbeit wurden mit Ruthenium beladene Träger (Silicalit-1, NaA und ZSM-5) mittels XAS untersucht. Als Referenzverbindungen dienten wasserfreies und wasserhaltiges RuO<sub>2</sub>. Die XANES-Ergebnisse bestätigten, dass die Oxidationsstufe des Rutheniums in allen Proben, wie bei RuO<sub>2</sub>, +IV beträgt. Bei der EXAFS-Auswertung wurde das Programm FEFF verwendet, um die theoretischen EXAFS-Spektren von wasserfreiem und wasserhaltigem RuO<sub>2</sub> zu simulieren. Die experimentellen EXAFS-Spektren der rutheniumhaltigen Träger NaA, Na-ZSM-5 und Silicalit-1 wurden entweder mit dem Modell des wasserfreien RuO<sub>2</sub> oder des wasserhaltigen RuO<sub>2</sub> angepasst.

Die EXAFS-Untersuchung von Ruthenium in Silicalit-1 nach einer Nachbehandlung in Form einer Calcinierung zeigte, dass das enthaltene Ruthenium eine lokale Geometrie ähnlich zu wasserfreiem RuO<sub>2</sub> besitzt. Im Vergleich zu wasserfreiem RuO<sub>2</sub> beobachtet man aber eine größere Unordnung bezüglich der Abstände. Die gleichzeitige Abnahme der Koordinationszahlen höherer Ru–Ru Schalen und die geringere Abnahme der Koordinationszahl der Ru–O Schale weisen auf eine Einkapselung der Oxidcluster in den Zeolith-Poren hin.

---

Die EXAFS-Analyse der Struktur von Ru/ZSM-5 nach der Calcinierung wurde mit Hilfe des Strukturmodells von wasserhaltigem RuO<sub>2</sub> durchgeführt. Es zeigte sich, dass nicht agglomerierte Ru-Spezies mit einer lokalen Koordinationsgeometrie ähnlich zu wasserhaltigem RuO<sub>2</sub> in dem Zeolith-Träger vorliegen. Bei den Ru/NaA Proben wurden sowohl EXAFS- als auch in situ XANES-Untersuchungen durchgeführt. Aus der temperaturprogrammierten Reduktion der Ru/NaA Zeolithe ergab sich, dass das enthaltene Ruthenium mit der Oxidationsstufe von +IV bereits bei ca. 120 °C zu Rutheniummetall reduziert wird. Die Reduktion von reinem Rutheniumdioxid erfordert höhere Temperaturen. Die zeitliche Änderung des Oxidationszustandes wurde durch Linearkombinationsanalyse des XANES-Bereichs und mit Hilfe von Referenzverbindungen quantifiziert. Die EXAFS-Ergebnisse zeigten, dass das Ruthenium als ungeordnetes RuO<sub>2</sub> höchstwahrscheinlich in Form einer kettenförmigen Struktur verknüpfter RuO<sub>6</sub>-Oktaeder im NaA Zeolith vorliegt.

Änderungen der Oxidationszustände von Metall- und Metalloxidkatalysatoren im Verlauf von chemischen Reaktionen oder während einer oxidativen oder reduktiven Vorbehandlung können mit Hilfe von speziell entwickelten in situ XAS Zellen verfolgt werden. Weiterhin können Strukturänderungen von kleinen Metall- oder Metalloxidpartikeln aufgrund des Kontaktes mit der Atmosphäre oder anderen Gasen vermieden werden, wenn bereits die Präparation dieser Partikel vor der XAS-Messung innerhalb einer in situ Zelle durchgeführt wird. Aufgrund dieser Punkte wurde eine in situ XAS Reaktorzelle aus Quarz entwickelt, die unter Festbett-Bedingungen arbeitet. Die Zelle sollte vor allem für die Strukturcharakterisierung und für die Verfolgung von Oxidationszustandsänderungen bei chemischen Reaktionen von Katalysatoren mit Gasen verwendet werden.

Ein Inconel-Heizblock, ein dreiteiliger, dünnwandiger Quarzrohr-Reaktor und ultradichte Gas-Fittings, mit denen das Quarzrohr mit zwei Metallrohren für den Gasein- und Gasauslass verbunden wird, sind die Hauptkomponenten der Zelle. Diese Zelle wurde durch Aufheizen auf 350 °C und mit einem gekoppelten Massenspektrometer am HASY-LAB in Hamburg getestet. Am ANKA, Karlsruhe, wurde sie verwendet, um XAS-Spektren von Referenzmaterialien bei hohen Temperaturen und im Gasstrom zu messen. Temperaturabhängige XAS-Spektren von ZrO<sub>2</sub> und RuO<sub>2</sub> wurden gemessen und die EXAFS-Spektren dieser Verbindungen ausgewertet. Ein Gasmisch- und Versorgungssystem mit mehreren Massendurchflusscontrollern wurde ebenfalls entwickelt, so dass definierte

## *7. Zusammenfassung*

---

Gasmischungen in den Reaktor geleitet werden konnten. Das kompakte Design und der einstellbare x-y Tisch mit Mikrometergenauigkeit, auf dem die Zelle montiert wurde, ermöglichten eine schnelle Installation und Fokussierung des Synchrotronstrahls auf die Probe innerhalb des Quarzrohrs.

# A. Appendix

## A.1. XAS experiment

The XAS measurements presented in this work were carried out at the beamlines X1 and C of the Hamburger Synchrotronstrahlungslabor (HASYLAB, Hamburg) and at the XAS beamline of the Ångströmquelle Karlsruhe (ANKA, Karlsruhe). A schematic of the XAS experiment in transmission geometry is shown in figure A.1 and all XAS measurements were carried out in transmission geometry.

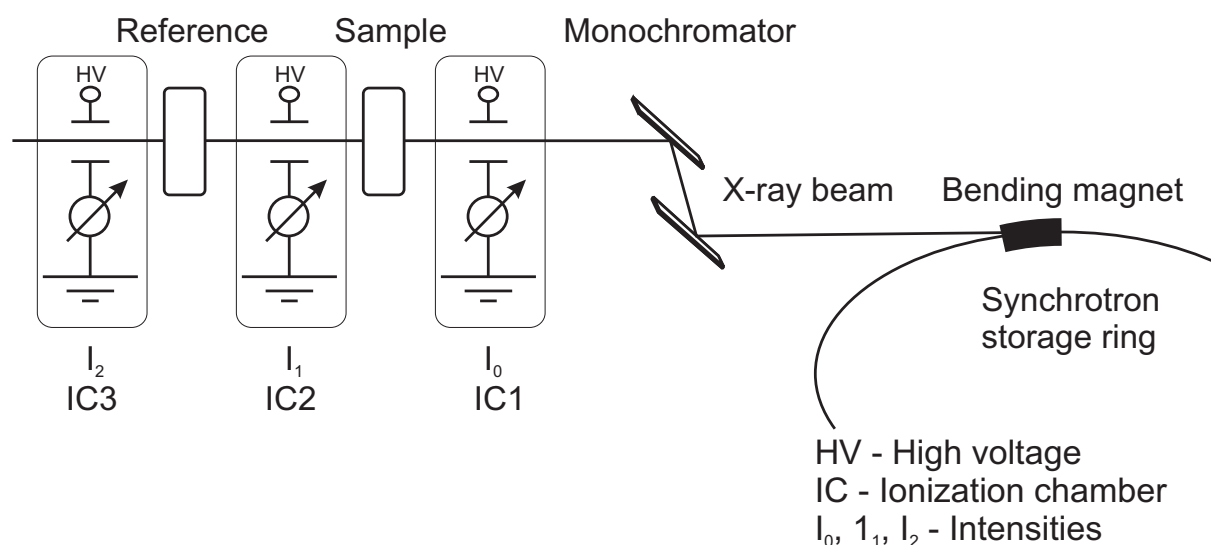


Figure A.1.: Layout of a typical XAS beamline experiment in transmission mode

Synchrotron radiation represents any radiation from charged particles traveling at relativistic speeds in applied magnetic fields which force them to travel along curved paths. Synchrotron radiation is normally produced in storage rings where electrons or positrons are kept circulating at constant energy. Synchrotron radiation is typically produced either in bending magnets needed to keep the electrons in a closed orbit, or in

insertion devices such as wigglers or undulators situated in the straight sections of the storage ring. Key properties of the x-ray radiation from a synchrotron radiation source include brilliance, which describes the quality of the x-ray beam, given in terms of number of photons emitted per second, collimation of the beam given in milliradian, for the horizontal and vertical direction, source area given in  $\text{mm}^2$  and spectral distribution. (Spectral distribution refers to those photon energies that contribute to the measured intensity of the radiation. In synchrotron radiation community, it is a convention to define this photon energy range as a fixed relative energy bandwidth, which in the present case is chosen to be 0.1%.) Altogether, brilliance is defined for a x-ray source in equation A.1 [86].

$$\text{Brilliance} = \frac{\text{Photons/second}}{(\text{mrad})^2 (\text{mm}^2 \text{ source area}) (0.1\% \text{ bandwidth})} \quad (\text{A.1})$$

Understandably, the intensity in photons per second after the monochromator crystal can be given by the product of the source brilliance, angular divergence set by the horizontal and vertical apertures (in milliradian), the source area (in  $\text{mm}^2$ ) and the relative energy bandwidth of the monochromator crystal. Further, synchrotron radiation is pulsed and the pulse duration is given by the electron bunch length divided by  $c$ , the speed of light.

### A.1.1. Monochromator

Monochromator is one of the most important components of an XAS experiment used to select the x-ray energy incident on the sample.

While low resolution x-ray absorption spectra (6 eV bandwidth) are sufficient for EXAFS data analysis, high resolution spectra are required for XANES data analysis because structural information can be extracted from a small energy shift of an absorption peak ( $\Delta E \geq 0.2$  eV) or from splitting of a peak. Because the intensities of absorption peaks (called white lines) contain information about structure (d band vacancies) careful preparation of samples free from pinholes and high harmonic suppression in the incident photon beam are required for XANES spectroscopy.

The energy bandwidth  $\Delta E$  of a photon beam monochromatized by Bragg diffraction on a crystal is monochromator is determined by the angular divergence  $\Delta\theta$  and the crystal monochromator rocking curves [87].

A x-ray monochromator usually consists of two parallel crystals (double crystal monochromator) or a single crystal with a slot cut through it (channel cut monochromator). All the XAS experiment stations where the samples were measured (Beamlines X1, C and ANKA-XAS) employ a double crystal monochromator. Typical monochromator crystals are made of silicon or germanium and are cut and polished such that a particular atomic plane of the crystal, described by the  $(hkl)$  indices, is parallel to the surface of the crystal. Common monochromator crystals used are Si(111), Si(311) and Si(511) whose  $(hkl)$  indices are all odd. The energy of x-rays diffracted by the crystal pair is controlled by rotating the crystals in the polychromatic beam. Only the x-rays with energies that satisfy Bragg's law given in equation A.2 are diffracted by the crystals [19].

$$2d \sin \theta = n\lambda \quad (\text{A.2})$$

where  $d$  is the spacing of the atomic planes of the crystal parallel to its surface,  $\theta$  is the angle of the crystal with respect to the incident polychromatic beam,  $\lambda$  is the wavelength of the diffracted x-ray and  $n$  is an integer. The fundamental x-ray energy according to equation A.3 corresponds to  $n=1$  and x-rays of higher harmonic energies correspond to  $n>1$ .

$$E = \frac{hc}{\lambda} = \frac{nhc}{2d \sin \theta} \quad (\text{A.3})$$

XAS scan over an energy range is performed by successive change of the x-ray energy that is determined by the angle of the monochromator crystals relative to the incident x-ray beam through Bragg's law given in equation A.2. Both the monochromator crystals are rotated by a joint goniometer as shown in figure A.2. To this goniometer an additional optical angle encoder (Heidenhain ROD800) is attached due to the significantly higher resolution and reproducibility achieved in the energy scale.

According to Bragg's law, a crystal illuminated by a collimated white beam not only reflects the desired wavelength  $\lambda$  given by equation A.2 but also  $(\lambda/n)$  referred to

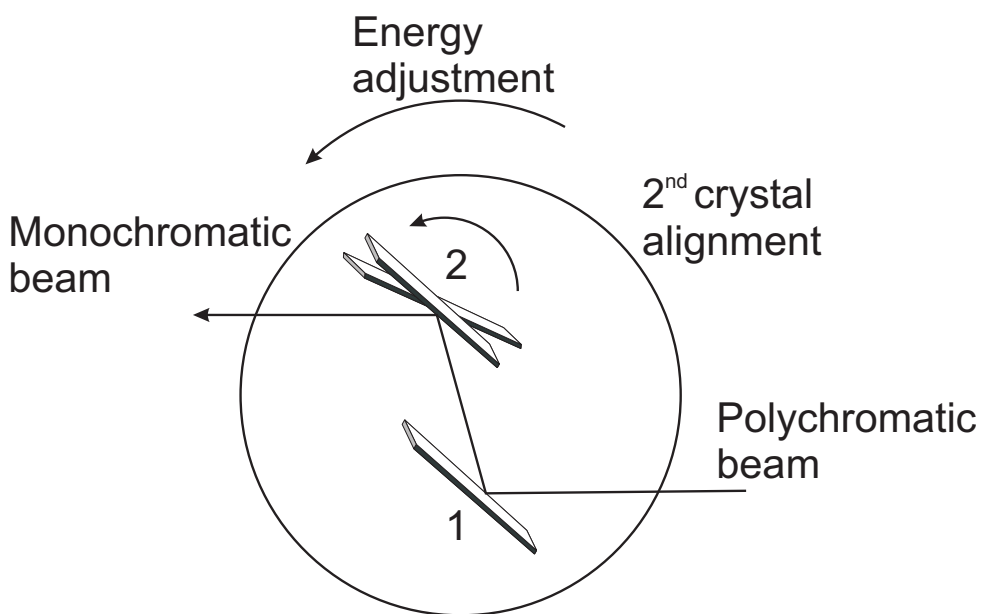


Figure A.2.: Double crystal monochromator mounted on a goniometer. In addition, the second crystal can be rotated separately and used to detune the monochromator.

as harmonics. In a typical transmission mode XAS measurement ionization chambers (which are not energy discriminative) are used and the higher harmonics which are hardly absorbed by the samples can contribute to the ionization current in the chambers. These higher harmonics must therefore be eliminated before entering the ionization chamber used for detection.

Further, higher harmonics are rejected based upon the knowledge that each diffracted energy has some angular spread due to the divergence of the source beam and inherent disorder in monochromator crystals. The higher energy beams of the harmonics generally have less angular spread than fundamental [19]. By slightly detuning (rotating the second crystal away from parallel with the first crystal) the double crystal monochromator by moving away from the peak of its rocking curve, most of the intensity from the harmonic can be rejected while the fundamental remains mostly unchanged.

### Rocking curve

A rocking curve is measured usually by keeping one crystal at a fixed angle and rotating the second crystal as shown in figure A.2. The shape of the rocking curve resembles a



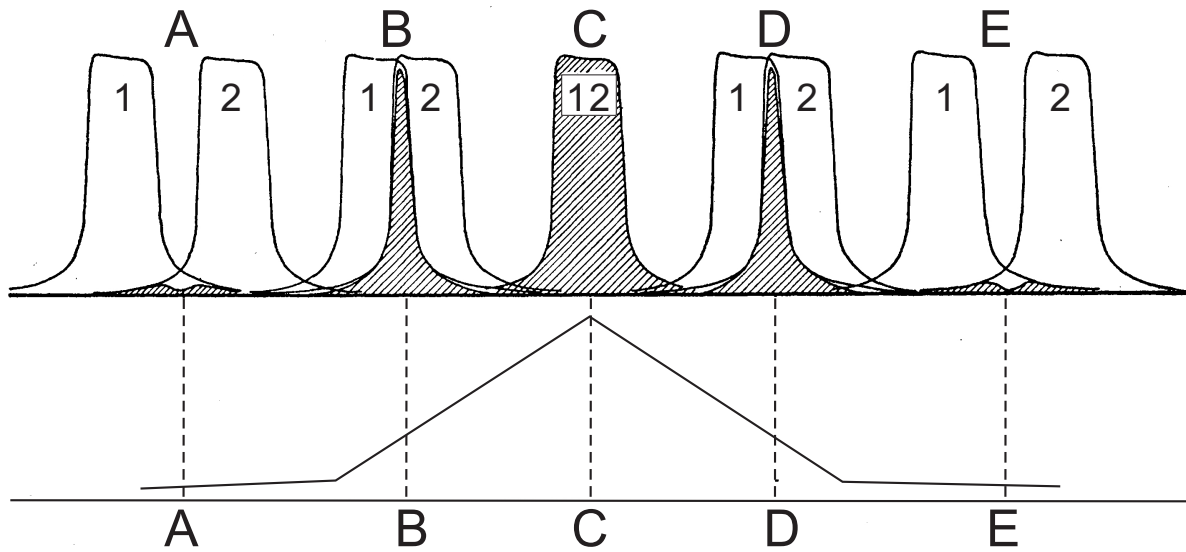


Figure A.3.: Variation of reflected intensity with various degrees of overlapping of the diffraction patterns of crystals 1 and 2 as the crystals are rocked through the parallel position. The values of the product integrals plotted as ordinates in the lower curve correspond to total superposed area available with different degrees of overlap

triangle and is different to that of the angular Darwin reflectivity curve (Additionally, Darwin width gives the angular width over which a particular reflection will diffract) of one crystal which can be approximated as a rectangle. The rocking curve is in fact the convolution of the reflectivity curves of the two crystals in the monochromator which can be explained with the help of figure A.3 which shows the different orientations of one monochromator crystal with respect to the other and their reflectivity curves.

In figure A.3, A, B, C, D and E represent the different configurations of crystals 1 and 2 relative to each other with C representing the relative angular offset  $\Delta\theta = 0$ . The intensity of x-rays reflected by the pair of crystals are represented by the region of overlap of the reflectivity curves of crystal 1 and 2. As one moves from setting A–E, the curves go from not overlapping to overlapping, then apart again, so the transmission of the whole system passes through a maximum at C.

The rocking curve can also be explained with a graphical tool first developed by Du-Mond [88]. An optical element inserted into an x-ray beam is supposed to modify some property of the beam such as its width, its divergence, or its wavelength band. It is

useful to describe this modification of the beam by a transfer function. The transfer function relates the input parameters of the beam before the optical element to the output parameters after the beam has passed the optical element. In the case of the monochromator, the perfect crystal is the optical element and the relevant beam parameters are beam divergence and wavelength band.

DuMond diagram is a graphical representation of the transfer function in which the horizontal axis is the beam divergence and the vertical axis is  $(\lambda/2d)$ .

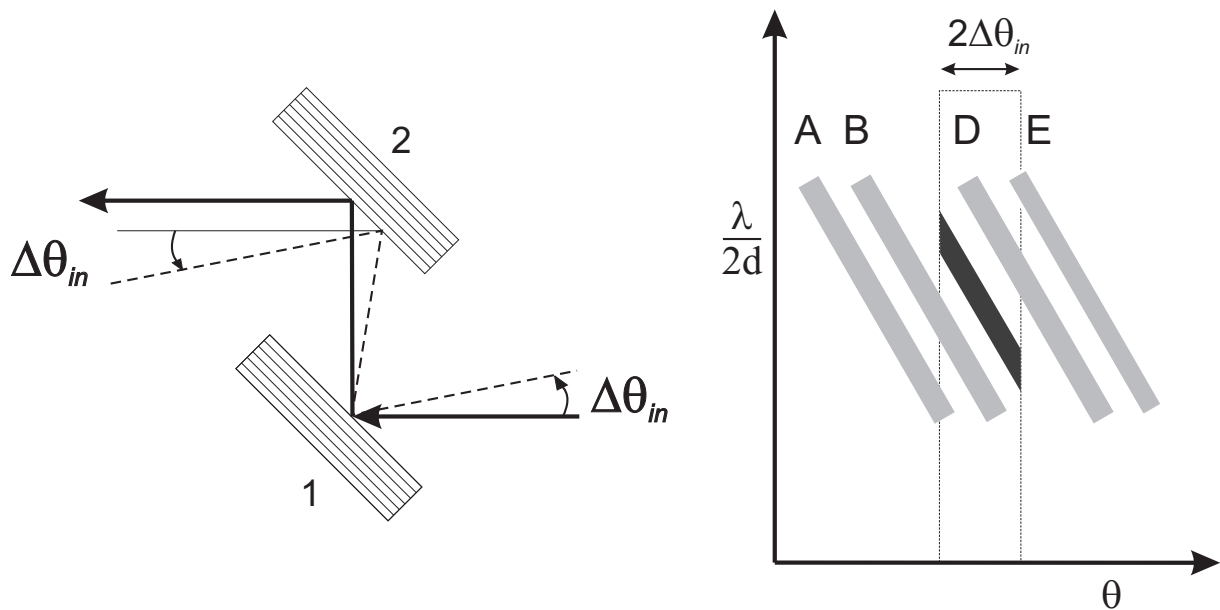


Figure A.4.: X-rays from a white source are incident on two crystals aligned in the same orientation. The central ray (full line) will be Bragg reflected by both the crystals and will emerge parallel to the original ray. The angle of incidence this ray makes with the second crystal is the same as that it made with the first, and will be Bragg reflected. The DuMond diagram in the right shows that a scan of the second crystal has a width equal to the convolution of the Darwin widths of the two crystals

DuMond diagram (right) for a non dispersive symmetric Bragg geometry (left) is shown in figure A.4 [86]. The beam incident on the first crystal is the boxed portion with an angular width of  $2\Delta\theta_{in}$  indicated in the right hand side figure. The slanted dark gray bar is the region in energy-angle spaced passed by the first crystal and its vertical width is the Darwin width. The light gray bars marked A, B, D and E represent the passband of the second crystal in energy-angle space for various values of the angular

offset similar to the scenarios A, B, D and E shown earlier in figure A.3. The pass bands for crystals 1 and 2 overlap for the configuration C. The X-rays reflected by the pair of crystals are represented by the region of overlap of the dark gray and light gray bars. As one moves from angle setting A–E, the bars go from completely not overlapping (A and B) to overlapping (C), then apart again (D and E), and the transmission of the whole system passes through a maximum. Only from an angular setting which lies between B and D will there be scattered intensity after the second crystal.

In all the XAS experiments described in this work, detuning of the second monochromator crystal to 35–40% intensity was used for harmonic rejection because a small offset in the angle of the second crystal with respect to the angle of the first crystal causes the x-ray intensity to be decreased slightly for the fundamental energy while dramatically decreasing the higher harmonic intensity [89]. For example, 35% detuning means that the incident x-ray intensity measured in the ionization chamber 1,  $I_0$  (given in figure A.1) has been decreased by 35% of its maximum value.

The edge energies of the elements studied in this work, the beamlines where the spectra were recorded along with the double crystal monochromator chosen for the measurement are presented in table A.1.

Crystal pair	Element	Edge	Energy / eV	Beamline
Si(111)	Platinum	L <sub>3</sub>	11563	X1, C
		L <sub>2</sub>	13272	
	Gold	L <sub>3</sub>	11918	X1, C, ANKA-XAS
		L <sub>2</sub>	13733	
Si(311)	Ruthenium	K	22117	X1, C
	Zirconium	K	17998	ANKA-XAS

Table A.1.: The double crystal monochromator chosen according to the edge energies of the elements studied and the beamlines where the XAS spectra were recorded [90]

### A.1.2. Ion chambers

X-ray intensities for all the samples measured and reported in this work were measured using the simple but reliable gas ionization chambers marked IC1, IC2 and IC3 in figure A.1. An ionization chamber consists of two parallel plate electrodes with uniform electric field and an inert gas or gas mixture in between them. Absorption of x-ray beam ionizes the gas into photoelectron-ion pair and these charged carriers are swept by the electric field to the electrodes where they are measured as a current which is then further amplified using commercial current amplifiers (like those produced by Keithleys). Inert gases (He, N<sub>2</sub>, Ar, or Kr) or gas mixtures are normally used for filling the ionization chambers.

In order to measure the incident and transmitted beam intensities from the sample ionization chambers IC1 (intensity  $I_0$ ) and IC2 (intensity  $I_1$ ) are used while for the reference samples IC2 measures the incident intensity and IC3 (intensity  $I_2$ ) the transmitted intensity.

Considering that the sample is placed in between the ionization chambers IC1 and IC2, a monochromatic beam of x-rays of energy  $E$ , which passes through the homogeneous sample of thickness  $x$ , is attenuated. In analogy to the Lambert-Beer law, this attenuation can be described by equation A.4.

$$\mu x = \ln \frac{I_0}{I_1} \quad (\text{A.4})$$

Here,  $I_0$  and  $I_1$  are the incident and transmitted x-ray intensities and  $\mu$  is the linear absorption coefficient.

## A.2. Analysis of XAS data

This section deals with the analytical techniques used in this study to extract information about the local structure around the absorbing atom from an experimental XAS spectrum. It is not intended here to extensively discuss the general EXAFS analysis procedure for which several review articles are available [19, 91, 92] but the FEFF based analysis procedure. Due to the complicated chore of data analysis, the following computer programs were used to analyze the XAS data in this study, apart from other data manipulation and plotting programs.

- FEFF calculates theoretical EXAFS spectra for a given spatial configuration of atoms based on curved-wave multiple scattering expansion of EXAFS equation [93].
- AUTOBK separates the experimentally measured x-ray absorption into background and EXAFS  $\chi(k)$  [94].
- FEFFIT modifies the theoretical EXAFS spectra from FEFF until a best fit is found to the experimental EXAFS data.
- ATOMS generates an input file to FEFF from the spatial coordinates of atoms or crystallography data.
- IFEFFIT incorporates AUTOBK, FEFFIT and ATOMS and provides an interface for data analysis through ATHENA and ARTEMIS [95, 96].

Certain key aspects of these programs in carrying out data analysis in general and details specific to the analysis of samples in different chapters will be mentioned when and where necessary.

### A.2.1. EXAFS Fourier transform

The analysis procedure used for the samples discussed in chapter on ruthenium catalysts is based on the analysis of the Fourier transform of EXAFS function. For these samples the FT of the data were analyzed with the use of conjugate variables  $k$  and  $2r$ . Due to the finite  $k$ -range of the measured data (from 3 to 18  $\text{\AA}^{-1}$ ), filtering of the data was done with a window function denoted as  $W(k)$ . An additional weighting term of the form  $k^n$ , with  $n = 1, 2$  or  $3$  was used to compensate for the decay in the amplitude of  $\chi(k)$  with increasing  $k$ .  $k$ -weighting as it is called, is also helpful to achieve a constant amplitude for the Fourier transformed signal. Fourier transform of the EXAFS signal after including the window function and weighting is given in equation A.5.

$$\tilde{\chi}(r) = \frac{1}{\sqrt{2\pi}} \int_0^{\infty} k^n \chi(k) W(k) \exp(i2kr) dk \quad (\text{A.5})$$

EXAFS signal from an experiment is discrete so for practical purposes a discrete version of equation A.5 which allows Fast Fourier Transform (FFT) algorithm is normally

used [97]. For a k-range data with  $N$ ,  $k_y = y\delta k$  and  $r_x = x\delta r$  the discrete Fourier transform is given by equation A.6.

$$\tilde{\chi}(r_x) = \text{FT}[\chi(k_y)] = \frac{\delta k}{\sqrt{\pi N}} \sum_{y=1}^N \chi(k_y) W(k_y) (k_y)^n \exp\left(\frac{i2\pi xy}{N}\right) \quad (\text{A.6})$$

### A.2.2. The isolation of $\chi(k)$

The first step in the analysis of EXAFS data is to convert the measured absorption data  $\mu(E)$  into the EXAFS  $\chi(k)$ , which is usually defined as given in equation A.7)

$$\chi(E) = \frac{\mu(E) - \mu_0(E)}{\mu_0(E)} \quad (\text{A.7})$$

$\chi(k)$  is obtained from  $\chi(E)$  by transforming the abscissa from photon energy to photo electron momentum  $k$  by applying the relation given in equation A.8.

$$k = \frac{\sqrt{2m(E - E_0)}}{\hbar} \quad (\text{A.8})$$

( $E_0$  is the threshold energy at the absorption edge step and the difference  $(E - E_0)$  is the kinetic energy of the ejected electron, which can be expressed by the momentum  $p$  of the electron or by the change of the amount of wave vector  $k$  of the electron given in equation A.9.

$$(E - E_0) = \frac{p^2}{2m} = \frac{\hbar^2 k^2}{2m} \quad (\text{A.9})$$

$\mu(E)$  is the total absorption from a single deep core level and the  $\mu_0$  is not the absorption coefficient for a truly isolated atom (*in vacuo*), but of an atom in its surrounding, where the the effect of the neighbors are “switched off”. Due to scattering of the ejected photoelectron from valence electrons, and also due to unspecific background factors (like spectrometer baseline, energy response of the detector *etc.*), this atomic background contains low frequency oscillations that cannot be measured independently or calculated from first principles.

The issues involved in the extraction of  $\chi(k)$  from the measured absorption are

1. to get the contribution to the total absorption from only the edge of interest and
2. to isolate the atomic absorption from the total absorption for that edge.

These two issues are handled by the program AUTOBK using the procedure explained in the next two sections.

### Pre-edge background and normalization

The first step in converting the total absorption to  $\chi(k)$  is to isolate the absorption due to the edge of interest from the absorption due to all other excitations followed by normalization. As an approximation of equation A.7, energy dependent normalization using  $\mu_0(E)$  can be replaced by a constant normalization, independent of energy. This approximation is not found to give serious errors in the results compared to other measurement uncertainties. The modified form of equation A.7 is of the form given in equation A.10.

$$\chi(E) = \frac{\mu(E) - \mu_0(E)}{\Delta\mu_0(E_0)} \quad (\text{A.10})$$

$\Delta\mu_0(E_0)$  used for normalizing EXAFS is determined by taking the difference in the extrapolation of smooth functional fits to the pre-edge total absorption and post-edge background absorption at the edge energy  $E_0, \mu_0(E_0)$ .

$$\Delta\mu_0(E_0) = \mu_0^+ - \mu_0^- \quad (\text{A.11})$$

The normalization process involved a regression to the XANES spectrum in the pre-edge region between  $[E_0 - 200, E_0 - 50]$  eV and the post-edge region between  $E_0$  to give  $\mu_0^-$ . A linear function is regressed to the pre-edge region, and a three term quadratic function is regressed to the post-edge region. These lines were extrapolated to the absorption edge,  $E_0$ , and the difference in absorption between these projected lines at  $E_0$  was the edge step. Normalized spectra were produced by subtracting the pre-edge line from the entire absorption data and then dividing the spectrum by the step height. After normalization, the pre-edge region lies along zero absorption and the edge step is 1.

### Post-edge background

The background function is constructed from splines that are connected with knots. A spline is a polynomial of  $n^{\text{th}}$  order, where order of 1, 2, or 3 correspond to linear quadratic or cubic splines. It can be determined with reasonable success due to the fact that the contributions from neighbor atoms to  $\chi(k)$  show much higher frequencies than that of the background  $\mu_0(E)$ . A common approach, called AUTOBK, was developed by Newville *et al.* [94] for post-edge background and is integrated into the IFEFFIT methods used by the program ATHENA [96].

In AUTOBK, the background function is constructed from third order (cubic) splines. The knots of the spline are not constrained in the optimization of the background function, which gives less importance to the placement of the knots. Information theory is used to constrain the background function to Fourier components that are longer in wavelength than that in the EXAFS spectrum by setting a maximum frequency component in  $R$  (called  $R_{\text{bkg}}$ ), below which contributing Fourier components are considered to be part of the background.

In the AUTOBK algorithm, the data range and the value for  $R_{\text{bkg}}$  determines the number of splines as given by equation A.12 [94].

$$N_{\text{bkg}} = \frac{2R_{\text{bkg}}\Delta k}{\pi} \quad (\text{A.12})$$

In general,  $R_{\text{bkg}}$  is about one-half the first nearest neighbor distance. This value for  $R_{\text{bkg}}$  allows all frequencies up to one-half the first shell distance to be removed by the background. The effectiveness of the background removal is ascertained by inspecting the Fourier transform of the  $\chi(k)$  data produced with different values of  $R_{\text{bkg}}$  since low frequency oscillations cause signals at artificially low distances at around 1 Å.

In order to ensure that only non-structural components of  $\mu(E)$  are removed by background removal, a rough calculation from FEFF of the expected first shell EXAFS spectrum without any structure optimization can be used. FT EXAFS spectra without ripples and strong discontinuities are good indications that the background removal was carried out in a good way. Additionally in IFEFFIT, the background spline parameters can also be iterated during an EXAFS fit to check if the structure parameters are strongly correlated to the background spline parameters.



**Comment on  $E_0$**  The threshold energy is chosen either as the energy position of the half edge jump or the inflection point of the absorption edge. This threshold energy represents the energy required to excite a core electron into an unoccupied state or into the continuum, creating a photoelectron. The threshold energy parameter or energy reference parameter,  $E_0$ , used for processing EXAFS data is not defined relative to the electron configuration within the solid (*i.e.*, the Fermi level or any other level), but rather it is a parameter that is used to align the experimental spectrum to the theoretically calculated spectrum. A systematic definition of  $E_0$  for all EXAFS spectra from the same absorption edge is desirable since a shift in  $E_0$  is determined in the fit of theoretical spectra to the experimental spectra. If all data sets have the same  $E_0$ , then all data sets will have the same energy shift. In this case, one variable can be used to model all data sets, rather than using a separate variable for each data set.

### A.3. Curve fitting of QXAS during CO interaction with 6wt% Pt/NaY

The key part of the Gnu plot routine used for curve fitting is given below:

```
# x0 = x-axis shift parameter of center of atan
# y0 = y-axis shift parameter of center of atan
# g1 = width of atan
# wv = Voigt line width
FIT_LIMIT=1e-07
set xrange[11540:11580]
set yrange[-0.5:1.5]
# Define the atan function
f0(x)=y0+(a/pi)*(atan((x-x0)/wa))
# Define Lorentzian
f1(x)=(wv/2)/((x-x1)**2+(wv/2)**2)
#Define Gaussian
f2(x)=exp(-(x-x1)**2*4*log(2)/wv**2)
# Define the function as superposition of a Gaussian and Lorentzian
f3(x)=m*f1(x)+(1-m)*f2(x)
```

## A. Appendix

---

```
# Define the function with an height (amplitude) term
f(x)=f0(x)+h*f3(x)
# Define the initial set of parameters
x1=11569.5;x0=11575.5;wv=5.4;h=5;m=0.5;wa=2.75;y0=0.5;a=1;
fit f(x) 'spt01_CO.norm' using 1:($2) via x0,wv,h,m;
set xrange[11540:11600]
plot "spt01_CO.norm" using 1:($2) ti "Experiment" w p 7,\
f(x) ti "Fit" w l 1,\
f0(x) ti "Arctan" w l 2,\
h*f3(x) ti "Pseudo-Voigt" w l 3,\
"spt01_CO.norm" using 1:(-f($1)+$2) ti "Residual" w l 4
```

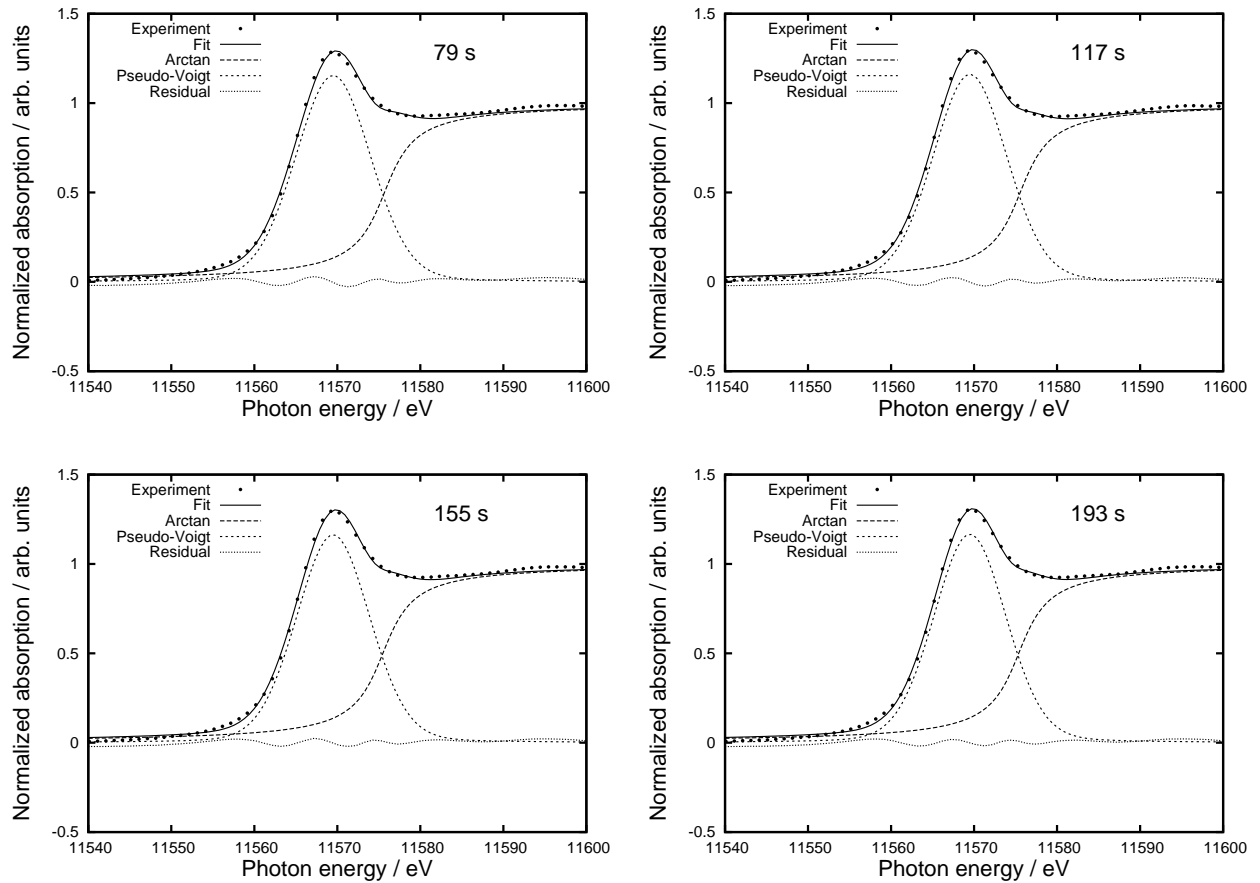


Figure A.5.: The experimental Q-XAS spectra measured after a given time of CO interaction, fit to the experimental spectrum using an arctan function to the rising absorption edge and a pseudo-Voigt function to the white line and the residual from the fit to the experiment are given for spectra 1–4

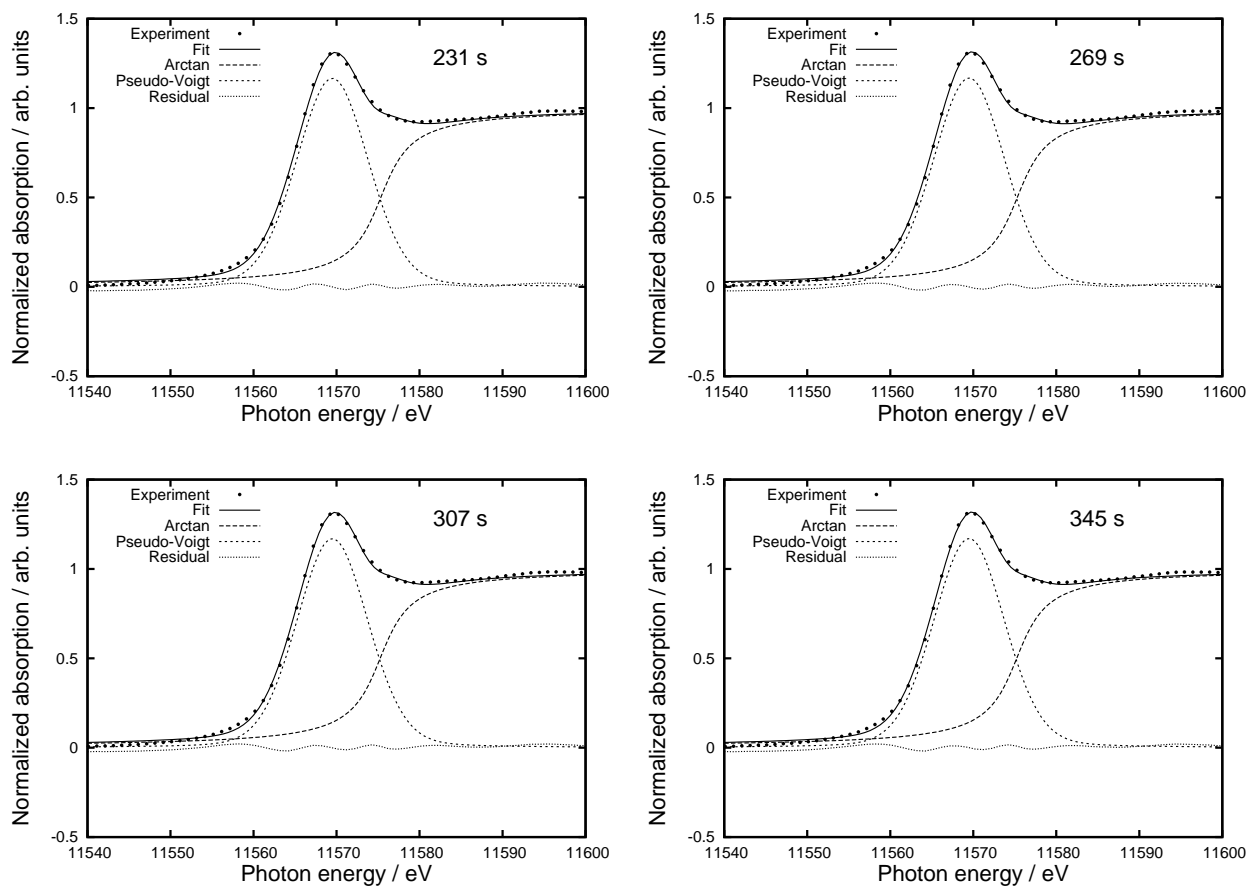


Figure A.6.: The experimental Q-XAS spectra measured after a given time of CO interaction, fit to the experimental spectrum using an arctan function to the rising absorption edge and a pseudo-Voigt function to the white line and the residual from the fit to the experiment are given for spectra 5–8

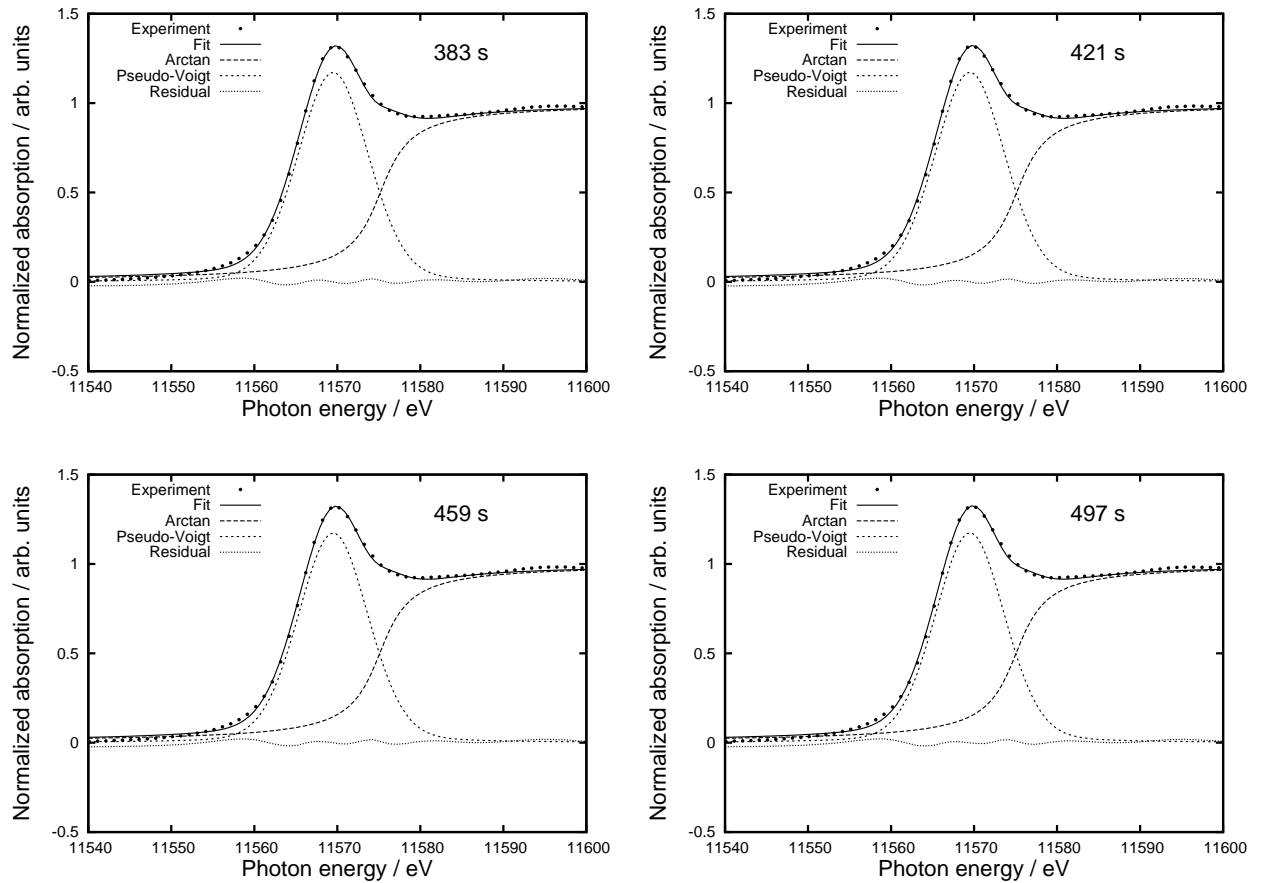


Figure A.7.: The experimental Q-XAS spectra measured after a given time of CO interaction, fit to the experimental spectrum using an arctan function to the rising absorption edge and a pseudo-Voigt function to the white line and the residual from the fit to the experiment are given for spectra 9–12

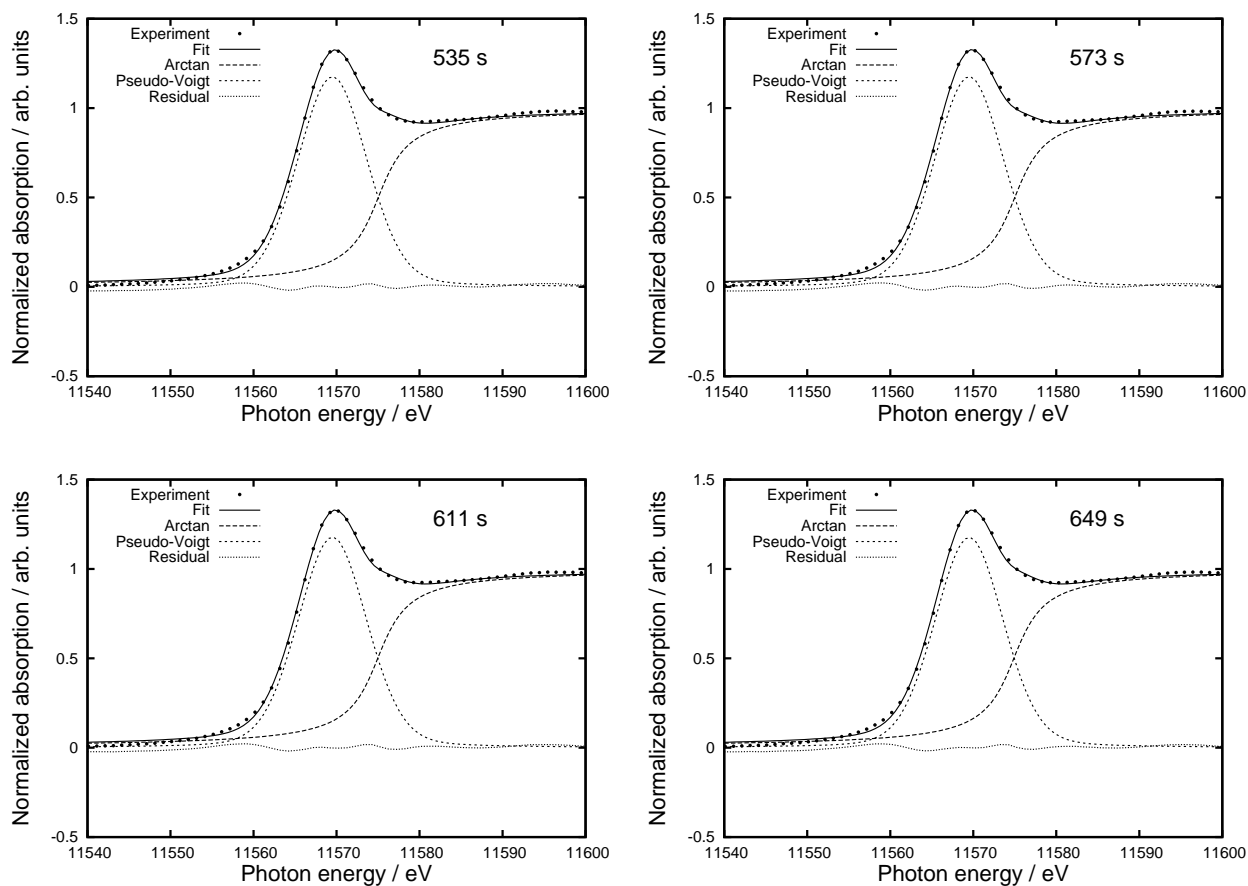


Figure A.8.: The experimental Q-XAS spectra measured after a given time of CO interaction, fit to the experimental spectrum using an arctan function to the rising absorption edge and a pseudo-Voigt function to the white line and the residual from the fit to the experiment are given for spectra 13–16

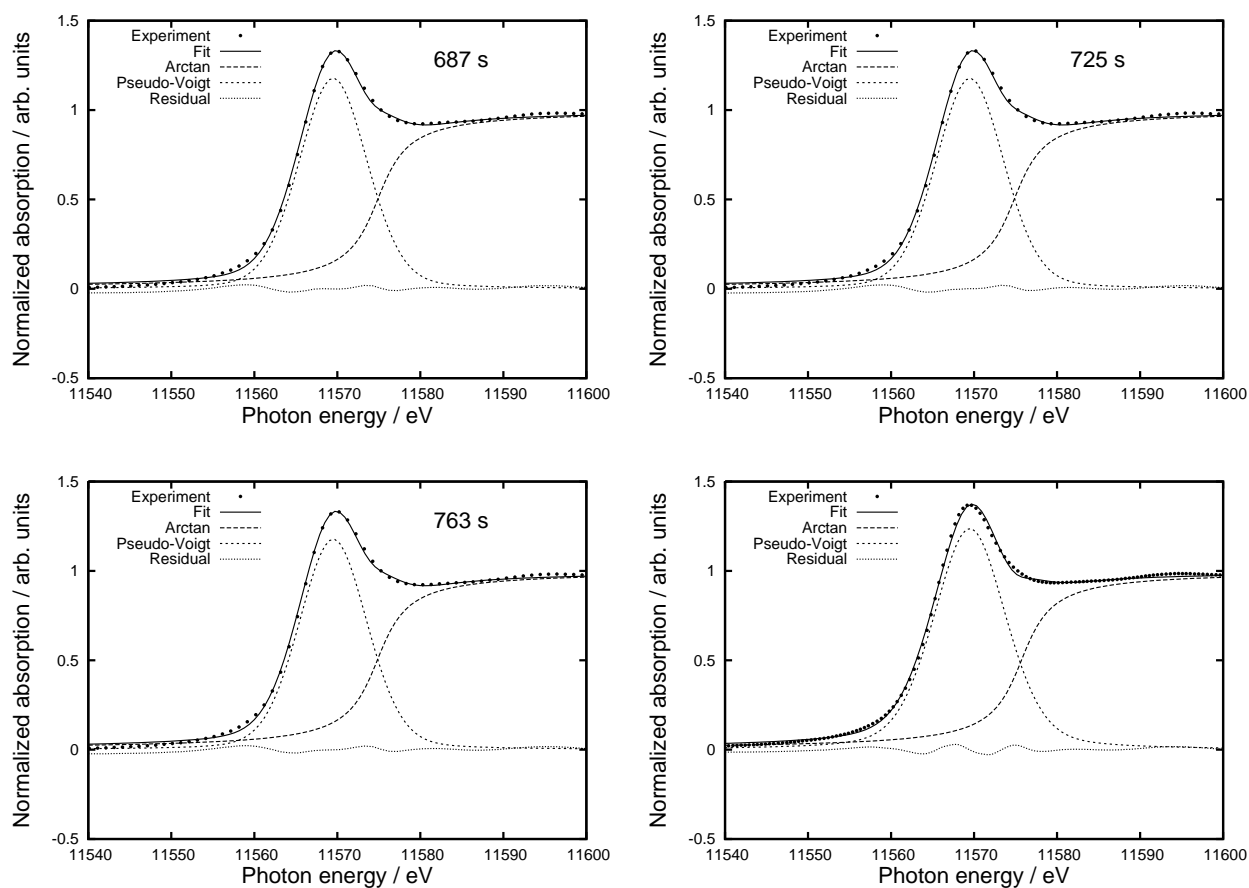


Figure A.9.: The experimental Q-XAS spectra measured after a given time of CO interaction, fit to the experimental spectrum using an arctan function to the rising absorption edge and a pseudo-Voigt function to the white line and the residual from the fit to the experiment are given for spectra 17–19 along with the fit to the XANES spectra of 6wt% Pt-CO/NaY (bottom right)





# References

- [1] A. N. Mansour, J. W. Cook Jr., and D. E. Sayers, *Journal of Physical Chemistry* **88**, 2330 (1984).
- [2] S. Gurman, N. Binsted, and I. Ross, *Journal of Physics C: Solid State Physics* **17**, 143 (1984).
- [3] D. A. McKeown, P. L. Hagans, L. P. L. Carette, A. E. Russel, K. E. Swider, and R. Rolison, *Journal of Physical Chemistry B* **103**, 4825 (1999).
- [4] T.-K. Sham, S. J. Naftel, and I. Coulthard, *Journal of Applied Physics* **79**, 7134 (1996).
- [5] S. Kraft, Stümpel., P. Becker, and U. Kuetsgens, *Review of Scientific Instruments* **67**, 681 (1996).
- [6] W. M. H. Sachtler, *Catalysis Today* **15**, 419 (1992).
- [7] S. Ciccariello, A. Benedetti, F. Pinna, G. Strukul, W. Juszczyk, and W. Brumberger, *Physical Chemistry Chemical Physics* **1**, 367 (1999).
- [8] R. Burch, J. P. Breen, and F. C. Meunier, *Applied Catalysis B: Environmental* **39**, 283 (2002).
- [9] S. D. Jackson, J. Willis, G. D. McLellan, G. Webb, M. B. T. Keegan, R. B. Moyes, S. Simpson, P. B. Wells, and R. Whyman, *Journal of Catalysis* **139**, 191 (1993).
- [10] O. S. Alexeev, F. Li, M. D. Amiridis, and B. C. Gates, *Journal of Physical Chemistry B* **109**, 2338 (2005).
- [11] E. Bus and J. A. van Bokhoven, *Journal of Physical Chemistry C* **78**, 121404 (2007).
- [12] F. Vila, J. J. Rehr, J. Kas, R. G. Nuzzo, and A. I. Frenkel, *Physical Review B* **111**, 9761 (2008).

- [13] B. H. Morrow and A. Striolo, *Molecular Simulation* **35**, 795 (2009).
- [14] A. C. Shi and R. Masel, *Journal of Catalysis* **120**, 421 (1989).
- [15] S. D. Jackson, B. M. Glanville, J. Willis, G. D. Mclellan, G. Webb, R. B. Moyes, S. Simpson, P. B. Wells, and R. Whyman, *Journal of Catalysis* **139**, 207 (1993).
- [16] B. L. Mojet and D. C. Koningsberger, *Catalysis letters* **39**, 191 (1996).
- [17] B. L. Mojet, J. T. Miller, and D. C. Koningsberger, *Journal of Physical Chemistry B* **103**, 2724 (1999).
- [18] D. C. Koningsberger, M. Oudenhuijzen, J. Bitter, and D. Ramaker, *Topics in Catalysis* **10**, 167 (2000).
- [19] Y. Ji, M. J. van der Eerden, V. Koot, P. J. Kooyman, J. D. Meeldijk, B. M. Weckhuyzen, and D. C. Koningsberger, *Journal of catalysis* **234**, 376 (2005).
- [20] M. S. Tzou, B. K. Teo, and W. M. H. Sachtler, *Journal of Catalysis* **113**, 220 (1988).
- [21] D. C. Koningsberger and R. Prins, *X-ray absorption: Principles, Applications, Techniques of EXAFS, SEXAFS and XANES*, Wiley-Interscience publication, New York, 1992.
- [22] X. Liu, M. Bauer, H. Bertagnolli, and E. Roduner, *Physical Review Letters* **97**, 253401 (2006).
- [23] B.-K. Teo and P. A. Lee, *Journal of the American Chemical Society* **101**, 2815 (1979).
- [24] R. J. Goodfellow, I. R. Herbert, and A. G. Orpen, *Journal of the Chemical Society, Chemical Communications* **23**, 1386 (1983).
- [25] K. Torigoe, H. Remita, P. Georgette, J. Belloni, and D. Bazin, *Journal of Physical Chemistry B* **104**, 7050 (2000).
- [26] Y. Akdogan, S. Anantharaman, L. Xiong, G. K. Lahiri, H. Bertagnolli, and E. Roduner, *Journal of Physical Chemistry C* **113**, 2352 (2009).
- [27] L. L. Sheu, H. Knözinger, and W. M. H. Sachtler, *Catalysis Letters* **2**, 129 (1989).
- [28] A. De Mallmann and D. Barthomeuf, *Catalysis Letters* **5**, 293 (1990).
- [29] D. Koningsberger, B. Mojet, M. Jeff, and D. Ramaker, *Journal of Synchrotron Radiation* **6**, 135 (1999).

- 
- [30] N. Ichikuni and Y. Iwasawa, *Catalysis Letters* **20**, 87 (1993).
- [31] M. Brown, R. E. Peierls, and E. A. Stern, *Physical Review B* **15**, 738 (1977).
- [32] P. S. P. Wei and F. W. Lytle, *Physical Review B* **19**, 679 (1979).
- [33] T.-K. Sham, *Physical Review B* **31**, 1888 (1985).
- [34] M. Vaarkamp, B. L. Mojet, M. J. Kappers, J. T. Miller, and D. C. Koningsberger, *Journal of Physical Chemistry* **99**, 16067 (1995).
- [35] B. I. Boyanov and T. Morrison, *Journal of Physical Chemistry* **100**, 16318 (1996).
- [36] J. Graetz, C. C. Ahn, H. Ouyang, P. Rez, and B. Fultz, *Physical Review B* **69**, 235103 (2004).
- [37] R. Sousa Jr, F. Colmati, E. G. Ciapina, and E. R. Gonzalez, *Journal of Solid State Electrochemistry* **11**, 1549 (2007).
- [38] J. A. Horsley, *Journal of Chemical Physics* **76**, 1451 (1982).
- [39] N. F. Mott, *Proceedings of the Physical Society, London* **62**, 416 (1949).
- [40] E. A. Stern and J. J. Rehr, *Physical Review B* **27**, 3351 (1983).
- [41] L. F. Mattheiss and R. E. Dietz, *Physical Review B* **22**, 1663 (1980).
- [42] P. W. Atkins and R. S. Friedman, *Molecular Quantum Mechanics, Third edition*, Oxford University Press, Oxford, New York, 2004.
- [43] B. W. Shore, *Reviews of Modern Physics* **39**, 439 (1967).
- [44] U. Fano and J. W. Cooper, *Physical Review* **137**, A1364 (1965).
- [45] E. H. S. Burhop, *The Auger Effect and other Radiationless Transitions*, Cambridge University Press, Cambridge, England, 1952.
- [46] U. Fano, *Physical Review* **124**, 1866 (1961).
- [47] E. A. Stern, *Physical Review B* **10**, 3027 (1974).
- [48] H. Funke, A. C. Scheinost, and M. Chukalina, *Physical Review B* **71**, 094110 (2005).
- [49] M. Muñoz, P. Argoul, and F. Farges, *American Mineralogist* **88**, 694 (2003).
- [50] X. Shao, L. Shao, and G. Zhao, *Analytical Communications* **35**, 135 (1998).

- [51] K. Yamaguchi, Y. Ito, T. Mukoyama, M. Takahashi, and S. Emura, *Journal of Physics B: Atomic, Molecular and Optical Physics* **32**, 1393 (1999).
- [52] Y. Ding, T. Nanba, and Y. Miura, *Physical Review B* **58**, 14279 (1998).
- [53] T. Uchino, J. D. Harrop, S. N. Taraskin, and S. R. Elliott, *Physical Review B* **71**, 014202 (2005).
- [54] J. D. Harrop, S. N. Taraskin, and S. R. Elliott, *Physical Review E* **66**, 026703 (2002).
- [55] M. Sahnoun, C. Daul, and O. Haas, *Journal of Applied Physics* **101**, 014911 (2007).
- [56] S. Mallat, *A Wavelet Tour of Signal Processing*, Academic Press, San Diego, 2001.
- [57] P. Goupillaud, A. Grossmann, and J. Morlet, *Geophysical Research Letters* **11**, 85 (1984).
- [58] J. Hagen, *Industrial catalysis*, Wiley-VCH Verlag GmbH and Co. KGaA, Weinheim, Germany, 2006.
- [59] B. C. Gates, *Catalytic Chemistry*, Wiley, New York, 1992.
- [60] G. Ertl, H. Knözinger, F. Schüth, and J. Weitkamp, *Handbook of Heterogeneous Catalysis; Volume 3*, Wiley-VCH Verlag GmbH and Co. KGaA, Weinheim, Germany, 2008.
- [61] G. Meitzner, *Microchemical Journal* **71**, 143 (2002).
- [62] B.-Z. Zhan, M. A. White, T.-K. Sham, J. A. Pincock, R. J. Doucet, K. V. R. Rao, K. N. Robertson, and T. S. Cameron, *Journal of the American Chemical Society* **125**, 2195 (2003).
- [63] S. Altwasser, R. Gläser, A. S. Lo, P.-h. Liu, K.-j. Chao, and J. Weitkamp, *Microporous and Mesoporous materials* **89**, 109 (2005).
- [64] R. W. Thompson and K. C. Franklin, *Verified Synthesis of Zeolitic Materials, 2<sup>nd</sup> revised edition*, Elsevier, Amsterdam, 2001.
- [65] S. Altwasser, R. Gläser, and J. Weitkamp, *Microporous and Mesoporous materials* **104**, 281 (2007).
- [66] B.-Z. Zhan and E. Iglesia, *Angewandte Chemie International Edition* **46**, 3697 (2007).

- [67] H. Liu and E. Iglesia, *The Journal of Physical Chemistry B* **109**, 2155 (2005).
- [68] A. A. Bolzan, C. Fong, B. J. Kennedy, and C. Howard, *Acta Crystallographica* **B53**, 373 (1997).
- [69] T. Takeda, M. Nagata, H. Kobayashi, R. Kanno, Y. Kawamoto, M. Takano, T. Kamiyama, F. Izumi, and A. W. Sleight, *Journal of Solid State Chemistry* **140**, 182 (1998).
- [70] International zeolite association, database of zeolite structures, <http://www.iza-structure.org/databases>.
- [71] E. M. Flaningen, J. M. Bennet, R. W. Grose, J. P. Cohen, R. L. Patton, and R. M. Kirchner, *Nature* **271**, 512 (1978).
- [72] D. H. Olson, G. T. Kokotallo, S. L. Lawton, and W. M. Meier, *Journal of Physical Chemistry* **85**, 2238 (1981).
- [73] B. C. Gates, *Catalytic Chemistry*, Wiley, 1992.
- [74] T. B. Reed and D. W. Breck, *Journal of the American Chemical Society* **78**, 5972 (1956).
- [75] J. B. Goodenough, *Progress in Solid-State Chemistry* **5**, 145 (1971).
- [76] H. Schäfer, G. Schneidereit, and W. Gerhardt, *Zeitschrift für anorganische und allgemeine Chemie* **319**, 327 (1963).
- [77] K. E. Swider, C. I. Merzbacher, P. L. Hagans, and D. R. Rolison, *Chemistry of Materials* **9**, 1248 (1997).
- [78] G. S. Iles and M. E. A. Casale, *Platinum Metals Review* **11**, 126 (1967).
- [79] S. Trasatti, *Electrochimica Acta* **36**, 225 (1991).
- [80] G. Battaglin, A. Carnera, G. D. Mea, G. Lodi, and S. Trasatti, *Journal of the Chemical Society, Faraday Transactions 1: Physical Chemistry in Condensed Phases* **81**, 2995 (1985).
- [81] E. Wendel, *Röntgenabsorptionsspektroskopische Untersuchungen an Metallkomplexen, Mischoxiden und Platinkatalysatoren*, Dissertation, Universität Stuttgart, Stuttgart, Germany, 2010, Yet to be published.

- [82] R. Viswanathan, G. Hou, R. Liu, S. R. Bare, F. Modica, G. Mickelson, C. U. Segre, N. Leyarovska, and E. S. Smotkin, *Journal of Physical Chemistry B* **106**, 3458 (2002).
- [83] J. J. Rehr, R. C. Albers, and S. I. Zabinsky, *Physical Review Letters* **69**, 3397 (1992).
- [84] P. R. Bevington and D. K. Robinson, *Data Reduction and Error analysis for Physical Sciences, Third Edition*, McGraw-Hill, United States, 2002.
- [85] E. Stern, M. Newville, B. Ravel, Y. Yacoby, and D. Haskel, *Physica B* **208-209**, 117 (1995).
- [86] K. V. Krishna Rao and L. Iyengar, *Acta Crystallographica* **A25**, 302 (1969).
- [87] J. Als-Nielsen and D. McMorrow, *Elements of Modern X-ray Physics*, John Wiley and Sons, Chichester, 2001.
- [88] A. H. Compton and S. K. Allison, *X-ray in Theory and Experiment*, Van Nostrand, New York, 1935.
- [89] J. W. M. DuMond, *Physical Review* **52**, 872 (1937).
- [90] D. Mills and V. Pollock, *Review of Scientific Instruments* **51**, 1664 (1980).
- [91] E. A. Stern and S. M. Heald, *Basic principles and applications of EXAFS*, North-Holland, New York, 1983.
- [92] T. M. Hayes and J. B. Boyce, *EXAFS spectroscopy*, Academic press, New York, 1982.
- [93] S. Zabinsky, J. Rehr, A. Ankudinov, R. Albers, and M. J. Eller, *Physical Review B* **52**, 2995 (1995).
- [94] M. Newville, P. Livins, Y. Yacoby, E. A. Stern, and J. J. Rehr, *Physical Review B* **47**, 14126 (1993).
- [95] M. Newville, *Journal of Synchrotron radiation* **8**, 322 (2001).
- [96] B. Ravel and M. Newville, *Journal of Synchrotron radiation* **12**, 537 (2005).
- [97] E. Oran Brigham, *The Fast Fourier Transform: An Introduction to Its Theory and Application*, Prentice Hall, Englewood Cliffs, NJ, 1973.

# Sankaran Anantharaman

---

Date of birth 01.01.1982  
Place of birth Tirunelveli, India  
Citizenship India

## Education

2005 - 2010 **Universität Stuttgart, Germany**  
Doctoral thesis in Physical Chemistry

2002 – 2004 **National Institute of Technology, Trichy, India**  
Master of Science in Applied Chemistry

1999 – 2002 **Bharathiar University, Coimbatore, India**  
Bachelor of Science in Applied Sciences

## Academic experience

July 2005 - July 2010 Doctoral thesis: *XAS investigation of catalytically relevant metal and metal oxides dispersed in inorganic matrices*  
Supervisor: Prof. Dr. H. Bertagnolli

January – June 2004 M.Sc. thesis: *Study of solvent effects on electronic and vibrational spectra of 4-dimethylamino-4'-nitroazobenzene and 4-hydroxyazobenzene*  
At: The department of Inorganic and Physical Chemistry, Indian Institute of Science, Bangalore, India.  
Supervisor: Prof. S. Umapathy

Dec – March 2002 B.Sc. project: *Evaluation of immersion plating efficiencies of cyanide free copper strike baths on mild steel*

## Honors

- Graduate college **Chemie in Interphasen** fellowship, Universität Tübingen
- DAAD - VIGONI program fellowship 2008-2009
- Best outgoing student award in M.Sc.

## Experimental skills

*Spectroscopic methods:* Synchrotron XAS, Laser Raman spectroscopy, UV-VIS, FT-IR, Mass spectrometry  
*Operating systems:* Microsoft Windows XP/2000, Apple OS X, Linux  
*Applications:* Matlab wavelet toolbox, Labview, LATEX, Microsoft Office and other common productivity packages for Windows, OS X and Linux platforms

## Publications

- 1) Y. Akdogan, **S. Anantharaman**, X. Liu, G. K. Lahiri, H. Bertagnolli, E. Roduner, Reconstruction of Pt<sub>13</sub> clusters into Pt<sub>2</sub>(CO)<sub>m</sub> on CO addition in NaY zeolite, **J. Phys. Chem. C** 2009, 113, 2352
- 2) A. Famengo, **S. Anantharaman**, G. Ischia, H. Bertagnolli, M. M. Natile, C. Maccato, E. Tondello, S. Gross, *Facile and reproducible synthesis of nanocrystalline ZnO from acetylacetonate: effect of experimental parameters and mechanistic investigations*, **Eur. J. Inorg. Chem.** 2009, 33, 5017
- 3) A. S. K. Hashmi, C. Lothschuetz, M. Ackermann, R. Doepp, **S. Anantharaman**, B. Marchetti, H. Bertagnolli. *Gold Catalysis: homogeneous oxidative esterification*, **Chemistry - A European Journal** 2010, 16, 8012